Reduced Order Modelling Applied to Parametric EIT and EEG for Comprehensive Characterisation of the Electrical Conductivities of Head Tissues

Matthew Ramsay Walker

School of Physics and Astronomy
Cardiff University

This dissertation is submitted for the degree of
Doctor of Philosophy

December 2024

Acknowledgements

This project was far from a solo effort and would not have been possible without an incredible amount of support throughout from family, friends and colleagues. I am extremely grateful for all of the people I have had around me for the past four years.

First and foremost, I would like to thank my primary supervisor Dr Leandro Beltrachini for his consistent enthusiasm, patience and commitment over the course of this project. Leo was understanding and helpful when my progress was slow, and a catalyst for results when work was going well. They encouraged my development as an independent researcher while allowing me to feel comfortable asking silly questions when I needed to. Above all else, Leo has been kind, a value that I have sincerely appreciated. It has been a privilege to have Leo as my supervisor.

I would also like to thank my secondary supervisor Professor Kevin Murphy and my mentor Dr Matthew Smith for their guidance and encouragement during this project. I would particularly like to thank Matt for his continued support of my academic and personal development over eight years as an undergraduate and then postgraduate student. I am also really thankful to all of my colleagues at Cardiff University Brain Research Imaging Centre (CUBRIC) for providing a fun and welcoming work environment. Similarly, I am very grateful to Dr Mariano Fernández-Corazza, Dr Sergei Turovets and Professor Carlos H. Muravchik for fruitful discussions, collaborations and gentle encouragement.

I would like to thank the Research Computing Services team at Cambridge University for my six month placement. I am incredibly grateful to everyone there who took the time to teach me about high performance computing and it was fantastic to be part of such a lovely team. I am also thankful to the AIMLAC CDT managers for their help with organising that placement. This PhD was financially supported by the UKRI AIMLAC CDT (funded by grant EP/S023992/1) and I am very grateful for their funding of me and this project.

To Mum and Dad, your continued patience, support and belief in me has been unwavering and I would not have made it nearly this far without you. For this, and everything else, I am eternally thankful. To Liv, Christine and Sophus, no-one can make me laugh like you three can. The moral support, laughs and wholesome memories you have given me has really kept me going. You are my role models in work and in life, and I love you all.

To my grandfather, our discussions on life, the universe and everything sparked a curiosity in me that will last a lifetime, and I have no doubt you would have read this entire thesis.

To my wonderful friends, it is difficult to put into words how much your support has meant to me over the last eight years. The sun-burnt bike rides, rainy runs, surprise hugs, mountain walks, pancake mornings and CUTri socials have made Cardiff my home. You know who you are, and you mean the world to me.

Summary

Electromagnetic source imaging (ESI) techniques based on electroencephalography (EEG) and magnetoencephalography (MEG) are used to better understand the function of the human brain and neurological conditions through monitoring electrical activity. ESI methods depend on models of the head encoding realistic and personalised anatomy and electrical conductivity characteristics. The anatomy can be extracted reliably from standard imaging techniques such as magnetic resonance imaging (MRI). However, extracting the individual conductivity of head tissues poses a unique challenge. This has been partially addressed by the development of parametric electrical impedance tomography (pEIT) and EEG/MEG-based calibrations, which aim to estimate these conductivities. Unfortunately, these techniques suffer from a heavy computational cost due to high-dimensional systems of equations needing to be solved. This thesis explores the application of a dimensionality reduction technique called reduced order modelling (ROM) to this problem, with the objective of accurate estimation of the conductivity of tissues in the head. For pEIT, the main results obtained were a substantial increase in speed and therefore practical accuracy while simultaneously unlocking, for the first time, the new ability to estimate the conductivity of deeper head tissues. An ROM-based calibration method utilising EEG data is also developed in this thesis, where the tuned conductivities of head tissues directly result in a large improvement in source localisation accuracy. The new frameworks developed in this work could have a far reaching impact in the field of EEG, providing new capabilities for researchers and clinicians.

Table of contents

List of figures

List of tables

Nomenclature

Acronyms/Abreviations

AP	Action Potential
CEM	Complete Electrode Model
CSF	Cerebrospinal Fluid
CT	Computerised Tomography
dB	Decibel
EEG	Electroencephalography
ESI	Electromagnetic Source Imaging
FEM	Finite Element Method
fMRI	Functional Magnetic Resonance Imaging
FP	Forward Problem
GM	Grey Matter
IP	Inverse Problem
MEG	Magnetoencephalography
MNS	Median Nerve Stimulation
MRI	Magnetic Resonance Imaging
PCA	Principle Component Analysis
pEIT	Paramteric Electrical Impedance Tomography

PEM Point Electrode Model

POD Proper Orthogonal Decomposition

PSP Postsynaptic Potential

ROI Region Of Interest

ROM Reduced Order modelling

SEP Somatosensory Evoked Potential

sLORETA Standardised Low Resolution brain Electromagnetic Tomography

SNR Signal-to-Noise Ratio

SVD Singular Value Decomposition

TDCS Transcranial Direct Current Stimulation

TES Transcranial Electrical Stimulation

WM White Matter

Notation

β Stability Factor

β_h Full-order Stability Factor

β_I Stability Factor Interpolant

$\boldsymbol{\sigma}$ Vector of P Electrical Conductivities

$\boldsymbol{A}$ Stiffness Matrix for CEM

$\boldsymbol{b}$ Source Vector

$\boldsymbol{b}^{EEG}$ Source Vector for the EEG-FP

$\boldsymbol{b}^{EIT}$ Source Vector for the EIT-FP

$\boldsymbol{J}^{p}$ Primary Current Density

$\boldsymbol{K}$ Stiffness Matrix

$\boldsymbol{q}$ Moment of Current Dipole

$\boldsymbol{u}^c$	Correction Potential on FE Mesh Nodes
$\boldsymbol{u}_N$	Reduced Basis Potential Solution
$\boldsymbol{u}_n$	Potential on FE Mesh Nodes
$\boldsymbol{y}$	Potential Measurements on Electrodes
$\dagger$	Moore-Penrose psuedoinverse
$\mathbb{C}$	Complex Numbers
$\mathbb{R}$	Real Numbers
$\mathbb{V}$	Transformation Matrix for a Reduced Model
$\mathscr{P}$	Parameter Space/Conductivity Space
$\mathscr{V}$	Pre-computed Vectors for Leadfield Matrix
Ω	Head Domain
$\partial\Omega$	Surface of Head Domain
ϕ_l	Piecewise Linear Basis Function on Electrode l
ψ_i	Piecewise Linear Basis Function on Node i
σ	Electrical Conductivity
Ξ	Sample Train of $\mathscr{P}$
e_l	Electrode l
H^1	Hilbert Space
I_l	Current Flowing through Electrode l
L	Number of Electrodes
N	Number of Snapshots in Reduced Model
n	Number of Nodes in FE mesh
P	Number of Tissues in Head Model
u	Electrical Potential Solution

u^{∞} Singularity Potential

U_l Potential on Electrode l

z_l Effective Contact Impedance on Electrode l

Chapter 1

General Introduction

1.1 General Overview and Motivation

The complexity of the human brain cannot be overstated. The unique and intricate composition and configuration of the brain generates the conditions necessary for all human thought, including consciousness, emotion, perception and reasoning. However, the exact chemical states and particular biological formations that allow these phenomena to exist are the subject of great scientific debate. Explaining these phenomena, and the mechanisms behind them, is the principle aim of the highly active field of cognitive neuroscience. In brains with certain neurological and psychiatric conditions, for which the underlying mechanisms stray from normal functioning, the additional characterisation of the pathology, diagnosis and treatment of these conditions is the domain of the tightly coupled fields of neurology, psychiatry and clinical neuroscience [113, 146]. All of these fields then share a similar line of inquiry, and fundamental to the progression of any scientific discipline is the concept of measurement. As such, knowing which metric to measure, and the most appropriate ways of measuring it, are essential considerations. In all of the aforementioned fields, the metrics to be measured overlap significantly, and therefore, so do the measurement devices.

A significant group of the technologies used in the neurosciences fall under the category of medical imaging and broadly speaking are divided into anatomical and functional imaging. These include magnetic resonance imaging (MRI), functional magnetic resonance imaging (fMRI), computerised tomography (CT), electrical impedance tomography (EIT), electroencephalography (EEG), magnetoencephalography (MEG) and positron emission tomography (PET) [98, 92, 86]. A relationship exists between most of these techniques, with each having distinct strengths and weaknesses and/or measuring different metrics. In many cases, imaging techniques can be used in conjunction with one another to achieve better results. For example, MRI and CT images compliment each other due to being sensitive to

different biological tissues in the human head [13]. These images can be co-registered to obtain a highly accurate picture of the head. A detailed picture like this can then be used in EEG, EIT or MEG, which require anatomical information for optimal performance [185, 60].

In functional imaging, one metric of particular interest is the electrical potential generated from active regions of the brain. This is measured by EEG and one use of these potential readings is to localise the source of the electrical activity [150]. EEG has the major advantages over other functional techniques of having high temporal resolution and being relatively cheap and mobile [86]. Localising sources over time can help us understand the operational relationship between different sections of the brain. EEG source localisation is, however, highly sensitive to anatomical accuracy and assumed electrical properties of the biological tissues [49, 184]. EIT is a technique that allows the characterisation of these electrical properties and is therefore highly complementary to EEG. This particular modality of EIT is known as parametric EIT (pEIT). Unfortunately, pEIT is not standard practice in the field mainly due to the associated computational expense.

Both EEG and pEIT are ill-posed inverse problems. An inverse problem (IP) constitutes estimating a quantity or quantities that can explain measurements taken, and typically consist of multiple forward problems (FPs). A FP simulates measurements using specific values for the quantity being estimated and other fixed parameters. The IP involves tuning the quantity until the FP simulated measurements are close to the real measurements. The ill-posedness comes from the fact that there are multiple values of the tunable quantity that produce similar simulated measurements in the FP. For EEG and pEIT, the FPs are computationally intensive, requiring a large system of equations to be solved, thus making the IPs also expensive. In the case of pEIT, the quantity to estimate is the conductivity of each tissue in a model. For EEG, the quantity to estimate is the location, magnitude and orientation of a source of electrical activity, where the fixed parameters can be the conductivities estimated by pEIT. In the abscence of pEIT, standard literature values are often used, which are known to lead to inaccuracies in the EEG-IP [116, 187]. Therefore, the main issue concerning EEG is the prohibitive cost of pEIT, which limits the personalisation of conductivities required for its accuracy.

1.2 Contributions

This thesis presents two major contributions to the field. The first is the application of a technique called reduced order modelling (ROM) to the pEIT-FP. This method is a form of dimensionality reduction and maps changes in the conductivity in the FP formulation to changes in the FP solution. This mapping can then be used for real-time generation of FPs

for any conductivity set, after a training phase which is much less computationally intensive than the previous method. Additionally, this speed up has now made it feasible to estimate all tissues in the head, instead of only a small subset, which was standard before.

Secondly, the newly trained ROM-pEIT-FP can now be utilised in the EEG-FP through the adjoint nature of the two problems to create real-time EEG-FPs for any conductivity set. This results in a powerful new framework, that compartmentalises the computationally intensive steps, allowing changes in the conductivity to be quickly mapped to changes in the EEG-FP solution. This separation allows the EEG-IP to estimate conductivities simultaneously with the current source. This additional degree of freedom, coupled with a large increase in speed, has the potential to unlock new levels of accuracy for EEG source localisation.

1.3 Thesis Structure

Chapter 2 continues this thesis with an introduction to the biological setting and neurophysiology responsible for generating electrical brain activity. A brief summary of the techniques used to localise this activity is provided before specific motivation for the use of each technique is given. High-density EEG is then looked at in more detail, with an overview of the basic apparatus used and an example of some signal processing of typical EEG data. The concept of forward problems (FPs) and inverse problems (IPs) is also covered in this section, which follows with a review of the need for accurate head models in EEG. Specifically, the effect of poor characterisation of the electrical conductivity field in the head models is explored. Finally, the use of parametric EIT (pEIT) is suggested as an antidote for head models with randomly assigned conductivities.

In Chapter 3, the mathematical foundations behind both the EEG and pEIT are laid out. Starting with Maxwell's equations for electromagnetism, the formulations are derived and one subsequent numerical implementation, highlighting the computational expense incurred in both methods by the FP. Additionally, the mathematical relationship between pEIT and EEG is described by the use of adjoint methods. Crucially, the dependence of the FPs on the conductivity of each head tissue is made clear.

Chapter 4 offers a solution to the computational expense in the pEIT-FP with the use of ROM to generate real-time FPs for any conductivity set. The application of ROM to pEIT (ROM-pEIT) is then tested with a realistic head model and a comparison between the full-order numerical solution in the pEIT-FP is then compared to the ROM-pEIT-FP to verify the appropriateness of this proposed solution.

Then, in Chapter 5, the ROM-pEIT framework is developed, including its incorporation with the IP. This new method is then utilised in a number of typical use cases where the

inverse performance is monitored. A clear comparison is then drawn between the use of the ROM-pEIT framework and the previous state-of-the-art technique with respect to overall speed and accuracy of reconstructed conductivities. This comparison is made with real and synthetic pEIT data. Examples of the new experiments that can be conceptualised thanks to the speed-up provided by ROM-pEIT are presented. Chapters 4 and 5 have been adapted from the submitted work: Matthew R. Walker, Mariano Fernández-Corazza, Sergei Turovets and Leandro Beltrachini, Electrical Impedance Tomography Meets Reduced Order Modelling: a Framework for Faster and More Reliable Conductivity Estimations [189].

The implementation of ROM-pEIT in EEG is then shown with the aid of the adjoint method described in Chapter 3. The generation of fast leadfield matrices for any conductivity set is then demonstrated and its accuracy compared to the full-order solutions verified. Taking advantage of this speed-up, a new optimisation technique is presented for the simultaneous reconstruction of electrical activity and tissue conductivity in realistic head models. The exact benefits to EEG are then presented. Finally, fusing the techniques of pEIT and the presented EEG-based conductivity estimation is shown to improve the estimation even further. The work in this Chapter has been prepared for publication as: Matthew R. Walker and Leandro Beltrachini, Fast Simultaneous Conductivity Estimation and Source Localisation in EEG using Reduced Order Modelling.

The final chapter summarises the major contributions of the thesis to the field and then concludes with the possible directions for new research. The future work proposed covers both the technical improvements in the framework, and the new directions of the field as a whole.

Chapter 2

Biophysical Electrical Phenomena and Measurement

2.1 Overview

To provide the necessary background for the remainder of this thesis, Chapters 2 and 3 detail the motivation, theory and mathematical background for the techniques of electroencephalography (EEG) and parametric electrical impedance tomography (pEIT). This chapter begins by describing the basic physiology of the brain and the neurons that make it, highlighting the generators of current in the brain. The motivation for localising brain current generators is given. An overview of EEG in various modalities and its role in neurological disorder assessment is then provided. Further, a light-touch primer of the basic principles for non-invasive high-resolution EEG with basic data pre-processing and source localisation is given. Finally, this chapter explores the construction of head models that limit the accuracy of EEG and the technique of pEIT that aids this construction. The use of pEIT to improve head model construction will provide the motivation for the following chapters.

2.2 Electricity in the brain

The brain and central nervous system are primarily formed of glial cells and neurons. The glial cells have been described as the supporting cells for the neurons and the ratio between the two and absolute number is still an open research question [182]. Recent studies have suggested the number of neurons in the brain is approximately 86 billion [17]. Each neuron has connections called synapses, where two neurons meet and communicate via the transmission

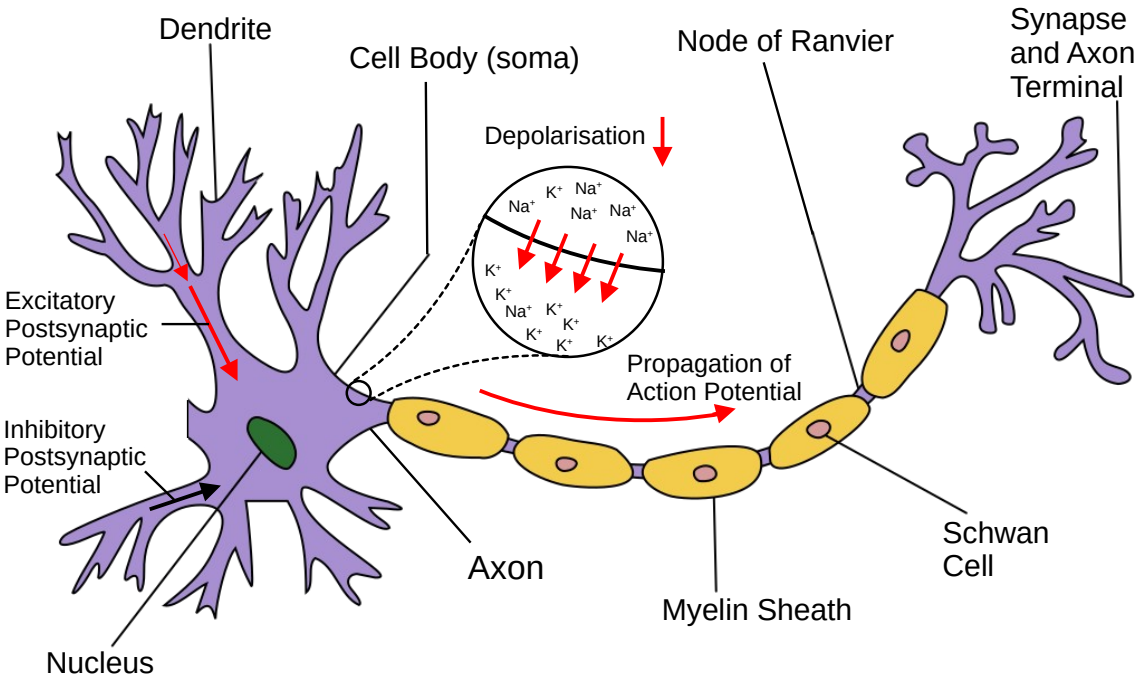

Fig. 2.1 Structure of a neuron. Adapted from an image by Quasar Jarosz on Wikimedia Commons under the Creative Commons Attribution-Share Alike 3.0 Unported license.

of chemicals. The number of synapses in the brain totals approximately 5×10^{14} [150]. This vast network of interconnecting neurons gives rise to the complex functionality of the brain.

A neuron is comprised of a cell body (soma), nucleus, axon, dendrites, axon terminals and synapses. Fig. 2.1 labels these different parts. At rest, a neuron holds a charge across the membrane of the cell where the inside is approximately -70 mV respective to the outside. This charge is held using an electrochemical gradient, where potassium and sodium ions have different concentrations inside and outside the cell. In this state, potassium has a higher concentration (140 mmol) inside the cell than outside (5 mmol), and sodium has the opposite arrangement (20 mmol inside and 140 mmol outside).

When a large enough potential (over a certain threshold) arrives at the neuron membrane, it causes sodium and potassium channels in the membrane to open and hence the permeability to increase. The sodium channels open faster, allowing the cell to be flooded with sodium ions in the direction of the gradient. This causes a depolarisation that gives the inside of the cell a 30 mV charge. The slower opening potassium channels then allow the potassium to travel out of the cell along their gradient, causing a hyperpolarisation of the cell membrane to -90 mV. Sodium and potassium pumps in the membrane then work to regenerate the electrochemical gradients back to -70 mV. This whole cycle takes about two milliseconds.

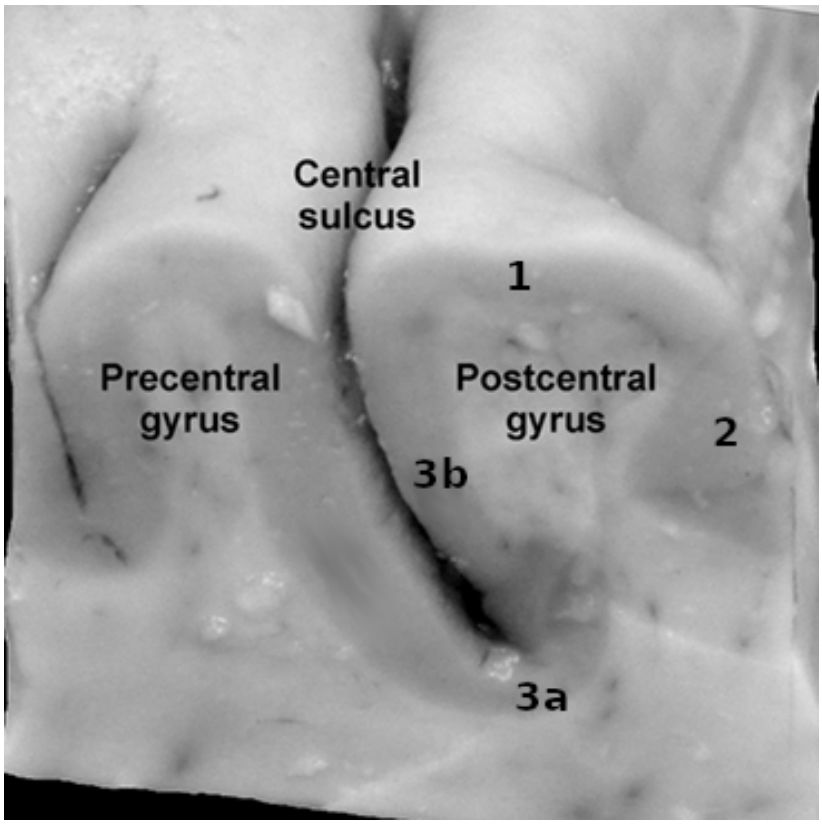

Fig. 2.2 Cortical slice displaying the postcentral and precentral gyrus, central sulcus and first three Brodmann areas. Image adapted from Geyer et al. (2011) under a Frontiers Media SA license agreement [74].

When travelling along an axon the depolarisation and repolarisation cycle is called an action potential (AP). The intracellular current created by the depolarisation and repolarisation generates two current dipoles with opposite polarities that sum to make an approximate quadrapole [86]. If an AP crosses a synapse - via the release of neurotransmitters from an axon terminal - it elicits a postsynaptic potential (PSP) in a dendrite of the neighbouring neuron. A neurotransmitter is a chemical that binds to receptors in the membrane of neuron causing it to open ion channels. A neurotransmitter can either be inhibitory or excitatory, causing inhibitory or excitatory postsynaptic potentials (I/EPSPs), respectively. PSPs travel along the dendrites towards the soma and if they reach the threshold potential when combined, an AP will instantiate in the axon. Although a PSP is roughly ten times small than an AP (10 mV to 100 mV, respectively), they are graded along the dendrite, creating an electrical dipole to form and causing a current to leak out of the cell. This can produce a measurable electrical potential as far as the scalp. Even though a PSP is smaller, concerted PSPs from many neurons are thought to produce signals at the scalp, not APs. This is due to the longer

durations of PSPs (up to 100 ms) and also due a dipolar source diminishing much more slowly than a quadrupolar source [86]. The propagation of changes in electrochemical imbalances across membranes along and between neurons are also referred to as electrical impulses. The impulses between connected neurons is the means of communication within the brain [86].

Fig. 2.1 displays a myelinated neuron, that has a myelin sheath around the axon. This myelin sheath is able to increase the speed with which the AP can propagate along the axon. It can achieve this by allowing the depolarisation to jump between gaps in the myelin sheath called nodes of Ranvier. This myelination is characteristic of most neurons in the white matter of the human brain. Conversely, the grey matter is formed mostly from unmeylinated neurons. The grey and white matter can be seen quite clearly in Fig. 2.2.

The cytoarchitecture (a term denoting the arrangement, shape, size and relative proportions of cells) can be further divided into regions in the grey matter. One of the most famous parcellations of this cytoarchitecture was published by Korbinian Brodmann in the early twentieth century, suggesting 43 distinguishable areas in human brains [74]. Although now considered outdated, it was widely accepted and is still used as a reference when referring to activity in specific areas of functionality in the cerebral cortex (grey matter). Fig. 2.2 displays a slice of the cortex across the central sulcus and the adjacent precentral and postcentral gyrus. The Brodmann areas 1, 2 and 3(a,b) are also labelled where 3b is on the anterior wall of the postcentral gyrus.

One popular angle of research has considered the description of networks within the brain to explain its inner workings [37]. This approach considers the use of graph theory to model the networks in question where the nodes in these models are generally formed using anatomically defined regions in the brain, such as Brodmann areas [37]. Substantial research efforts have branched from this concept, with the common goal of trying to characterise and identify the hyper-parameters of importance in complex networks such as those in the brain. Also of fundamental interest has been observing the difference in these networks between healthy and diseased brains. Linking connectivity and structural differences with pathological disease is an active pursuit in the field. In this vain, focus has been put on the differences in functional connectivity in neurological disorders, such as epilepsy [37]. In order to assess the connectivity, it is useful to measure the electrical activity in the brain and more specifically find its origin. This task is far from trivial and we present an overview of the methods to tackle this problem in the next section.

2.2.1 Electromagnetic Source Imaging

Electromagnetic Source Imaging (ESI) aims to localise the electrical activity in the brain. Two prominent techniques in the field are the source localisation modalities of electroen-

cephalography (EEG) and magnetoencephalography (MEG). These methods have a key advantage over other methods such as functional magnetic resonance imaging (fMRI), which is a high temporal resolution of the order of milliseconds [42]. As a result, these techniques are well positioned for connectivity analyses and brain mapping [201].

In MEG, magnetic fields near the surface of the head are traditionally measured using superconducting quantum interference devices (SQUIDs). The position of the sensors and the field strength are then used to reconstruct the source of electromagnetic activity within the brain. MEG has some advantages over its electrical counterpart EEG. For example, it has been suggested that MEG is less sensitive to perturbations in the the conductivity of the compact and spongiform skull [185]. However, MEG with SQUIDs (similarly to fMRI) is associated with significant setup and equipment costs, requiring magnetically shielded rooms (MSRs) which are expensive to build and does not allow for any movement of the participant. This has been somewhat alleviated by recent developments in the use of optically pumped magnometers (OPMs), however, this technology is still relatively new [100, 29].

For EEG, the electrical potential is measured on or in the head using electrodes. Similarly to MEG, the electrode positions and measurements can be used to reconstruct activity in the brain. Due to the physical contact required to obtain a potential measurement, there are many modalities and corresponding applications for EEG. These modalities can be both invasive and non-invasive, and, in comparison to MEG, are mobile, relatively cheap and do not require MSRs. In healthy brains, EEG has been widely adopted for connectivity analyses [156, 87, 69]. Conversely, in diseased brains, EEG has been utilised to diagnose and aid treatment of neurological conditions [86].

ESI in Epilepsy and Neurological Disease

EEG is an essential tool for pre-operative assessment in drug-resistant epilepsy patients. This course of treatment requires the identification of areas in the brain called epileptogenic zones (EZs), which is the area in the cortex of the brain required to be removed for complete seizure freedom. The EZ is estimated by determining the contributing sites of the seizure onset zone (cortex portion where seizures originate) and the irritative zone (cortex portion where interictal epileptic activity originates). The post surgical outcome is dependent on the accuracy of the identification of the EZ [82]. Historically, this identification has been achieved with highly invasive versions of EEG such as electrocorticography (ECoG) and stereo-EEG/intracranial-EEG (SEEG/iEEG) where either an array of electrodes is placed directly onto the scalp or a pair of electrodes are placed deep within the brain, respectively [202]. This can be far from ideal, given that these invasive electrodes need to remain in position for days at a time to monitor ictal and interictal activity, which can lead to major

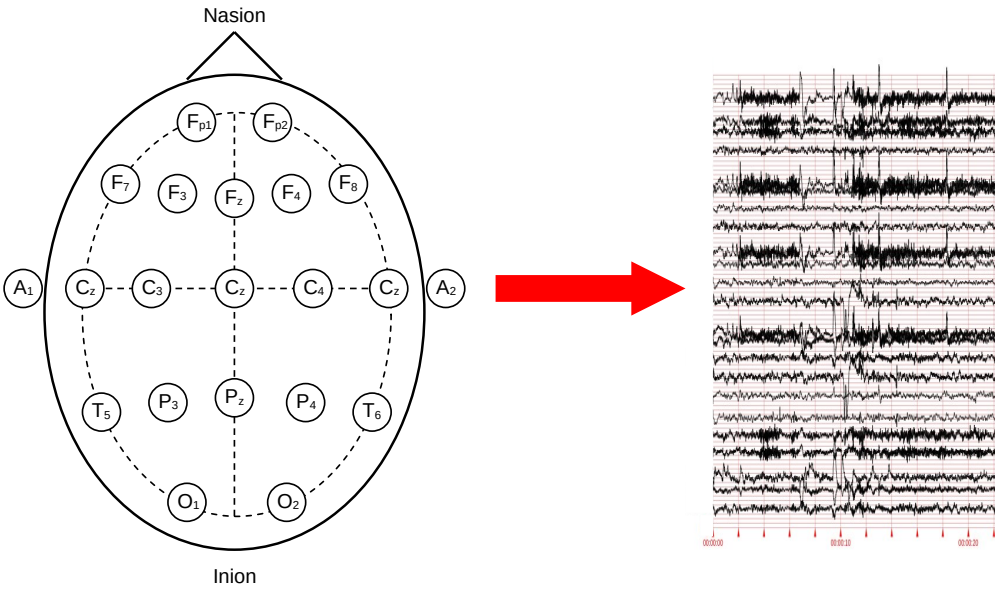

Fig. 2.3 Schematic of a 21 electrode EEG setup with the International 10-20 system standard. The electrodes are labelled based on their position on the head where F is frontal, F_p is pre-frontal, C is central, T is temporal, P is parietal, and O is occipital. Also labelled are the elcetrode A_1 and A_2 which are placed at the preauricular points (just before the ear canal). Also shown is an EEG recording from the open dataset collected by Shoeb (2010) [160]. The data was visualised using the open source software LightWAVE [121].

complications [82, 95]. This has motivated the use of non-invasive EEG, which is gaining traction as head models become more refined and as high-resolution EEG improves in accuracy [174]. These methods have been subsequently validated in a growing number of studies [45, 147, 199, 16]. Furthermore, recently it has been shown that combined analysis of EEG and MEG data can significantly improve source reconstruction in the context of epilepsy over invasive SEEG [15].

In addition to its role in preoperative epilepsy assessment, EEG has been used to study a myriad of other neurological disorders, including attention deficit hyperactive disorder (ADHD) and bipolar disorder (BD) [105, 54]. In both schizophrenia [71] and Parkinsons disease [168] well-characterised neurological responses to stimuli called somatosensory event potentials (SEPs) have been studied in diseased and healthy brains. Assessing these functional differences can lead to insights into the pathology of these diseases. Furthermore, EEG can be used in stroke detection through the breakdown of functional connectivity, assessment of brain activity in coma patients as well as for determining brain death [86].

2.3 Electroencephalography

High-resolution EEG is an essential clinical and research tool for understanding brain function and the assessment of neurological disease. From here on, any mention of EEG will be referring to non-invasive high-resolution scalp EEG.

2.3.1 Apparatus

EEG is traditionally performed using a cap with electrodes placed directly on the head. Depending on the type of electrodes, some work is then required to apply the electrodes to the scalp of the participant/patient who is to be measured. Each electrode, attached to a wire, then feeds back an electric potential to a differential amplifier. Each amplifier is connected to a common reference electrode and a measurement electrode. This means that the electrical potential measured on an electrode is the potential difference between that electrode and the common reference.

Fig. 2.3 shows a schematic of electrodes placed on the head in the International 10-20 system standard with an example EEG recording. The electrodes are positioned on imaginary lines seen in the figure, where the straight lines are formed using anatomical landmarks. These landmarks are the nasion, inion and preauricular points (labelled A_1 and A_2), which are above the nose, at the back of the head and just before each ear canal, respectively. At the vertex of the head, where the two straight lines cross, the electrode is labelled C_z. This is often chosen as the reference electrode. Other electrodes are named after which position of the head they are placed over. These labels are F, F_p, C, T, P and O which correspond to the frontal, pre-frontal, central, temporal, parietal and occipital areas of the head respectively. The International 10-10 system standard also exists with 81 electrodes and a similar labelling convention. Geodesic layouts (which are spaced differently and cover much more of the head and face) can have 64, 128 or 256 electrodes with additional reference electrodes. The BioSemi company, that produces commercial EEG caps, distribute their own layout as well as the popular 10-10 and 10-20 layouts. These are called "ABC" layouts and are named after the labelling convention used. In this layout the electrodes are spaced equiradially and come in nets (at the time of writing) with 16, 32, 64, 128, 160 and 256 electrodes. A 10-5 system has also been proposed, with a total of 345 electrodes [126].

2.3.2 Source Localisation

EEG signals can be interpreted in many ways. However, as stated in the previous sections, we are interested in analysing it in such a way that allows us to localise the source of an

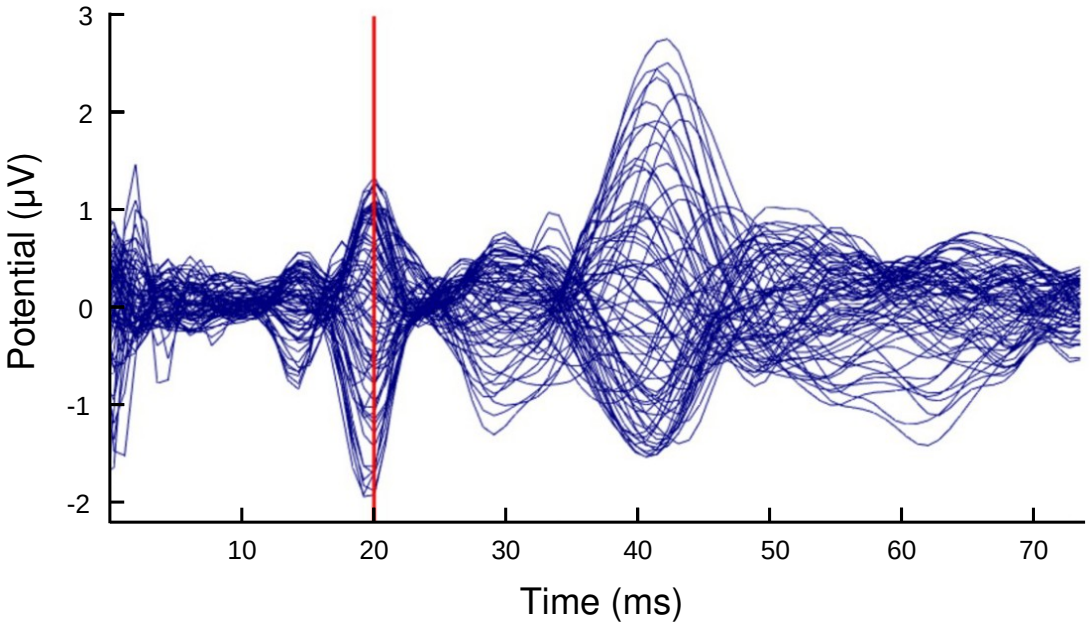

Fig. 2.4 Example SEP data where the stimulus is applied at 0 *ms* and the vertical red line highlights to high amplitudes at 20 *ms* typical of the P20/N20 component. This figure has been adapted from Schrader et al. (2021) under the CC-BY 4.0 Attribution license [158].

electrical current inside the brain. This section will provide a brief primer on multichannel EEG data preprocessing and analysis with the goal of source localisation. Also included is a motivating example that will be useful for chapter 6.

With sampling frequencies at approximately 1 kHz, up to 256 channels, and recording sessions lasting at least several minutes, a significant amount of data can be generated. Ideally, for source localisation, one set of potentials is required. Therefore, there is a need to reduced the readings taken into a single set. This preprocessing step is shown in the context of somatosensory evoked potentials.

Somatosensory Evoked Potentials

As an illustrative example of EEG source localisation, this Section will provide a brief background on somatosensory evoked potentials (SEPs) and how the data is processed. Evoked potentials are electrical potentials created by small, localised areas of current that occur in the brain due to a response to stimuli. A specific class of these evoked potentials are SEPs, where the current sources for some parts of the potential signal are thought to occur in the somatosensory cortex, located in the postcentral gyrus (see Fig. 2.2). SEPs are generated

through stimuli to the body, hence the name *somato-* which is derived from the Greek work *sōma* meaning body. One stimulus that generates SEP readings is median nerve stimulation (MNS), where the median nerve in the arm is stimulated using electrodes injecting current, to the point at which the current injected causes the thumb to twitch. The SEP generated can be split into multiple peaks and troughs that are named components. These components are thought to be the result of specific dipoles or combinations of dipoles [36] and are named depending on when they occur and what polarity they hold on a specific electrode. The SEP component P20/N20 caused by MNS is to indicate that there is approximately a 20 ms delay between the stimulus and the potential peak being measured, where the P or N stands for the polarity of the potential (positive or negative respectively) on each electrode [86]. The P20/N20 component is thought to originate in the somatosensory cortex whereas earlier ones (e.g., P2/N2) may originate from other areas such as the brain stem [36]. The polarity of course depends on the position of the reference electrode in use. Due to its high signal-to-noise ratios and ease of stimulation, SEPs are often used as test beds for new methods and sensitivity analysis in source localisation [16, 198, 184].

In addition to SEP responses from MNS, SEP measurements can also be made using tibial nerve stimulation or tactile stimulation [171, 36, 73]. Moreover, other classes of evoked potentials have been the topic of study, such as laser evoked potentials [31, 167, 72], auditory evoked potentials [76] and visual evoked potentials [89].

The response in the brain to a stimulus is of the order of milliseconds, meaning that in a single recording session, the stimulus can be applied thousands of times [36, 184]. The continuous data is then split into epochs, which are small sections of the data centred around the time of stimulation. The time spanned in each epoch contains a pre-stimulation interval (of the order of 100 ms) and the duration of the target response seen in the potential. The signal is then baseline corrected, by subtracting the average absolute power in the signal in the pre-stimulus interval before being passed through a frequency band filter. The signals in each epoch are then averaged for each channel, providing a single set of potentials for each channel. An example of the resulting signal at this stage is shown in Fig. 2.4 for SEP data with a clear response in the potential at 20 ms where the P20/N20 component is. This example cuts off at just over 70 ms but the SEP response carries on past this time point. For example, one peak is called the P140/N140 component, which is known as a long-latency SEP component that can be stimulated with MNS or tactile stimulation [73, 168].

Signal-to-Noise Ratio

An important consideration in EEG is the amount of noise in the data. This is useful not only to understand how trustworthy the data might be, but also to determine a suitable

level of noise to add to synthetic data. Noise can be characterised with value called the Signal-to-Noise Ratio (SNR) which is calculated as follows

$$SNR = \frac{P_s}{P_n}, \tag{2.1}$$

where P_s is the power of the signal and P_n is the power of the noise. For each channel, the power at the peak of the signal is assigned to P_s and the average power during a pre-stimulus interval is calculated for P_n. The length of the pre-stimulus interval is at the data analysts discretion, however, is typically of the order of 100 ms. SNR can also be given in decibels (dB) and this can be found from the linear SNR value with the following relation

$$SNR_{dB} = 20log_{10}(SNR). \tag{2.2}$$

In one of the earliest multichannel studies by Buchner et al. (1994), a range of 6.8 to 31.2 SNR values was found [36]. Similarly, values of 11.3, 7.5 (linear) and 26.4 dB were found for a SEP dataset by Aydin et al. (2014) [16], Vorwerk et al. (2019) [184] and Lew et al. (2009) [108, 198], respectively. In studies using synthetic data, values ranging from 40 db to 0 db have been utilised to simulate noise (where 0 db indicates a signal with the same power as the noise) [108, 120].

Forward and Inverse Problems

In Section 2.2, an electric dipole was described as being generated in the dendrites of a neuron during a PSP. An electric dipole consists of two point charges with some small separation between them, giving rise to a dipole moment, which has a direction and magnitude. When the separation tends to zero with the same moment, this limit is called a point dipole, which has been shown to be an adequate representation of current generators in the brain [51]. Furthermore, a point dipole has been shown to be a reasonable model specifically for current sources eliciting SEP responses [9, 85]. These dipoles can be modelled (although with some difficulty - see chapter 3) and the potential at each electrode simulated computationally. These simulations are called forward problems (FPs) in EEG. To construct the FP, the dipole is placed in a volume conductor with the approximate geometric features and conductivity of the human head (see next section). Maxwell's equations are then used to calculate the potential within and/or at the surface of the model and on the electrodes.

For distributed source models, a collection of dipoles in the brain is commonly referred to as a source space. The position of the dipoles in a source space is typically chosen to be in the centre of the grey matter. This central plane through the grey matter is calculated

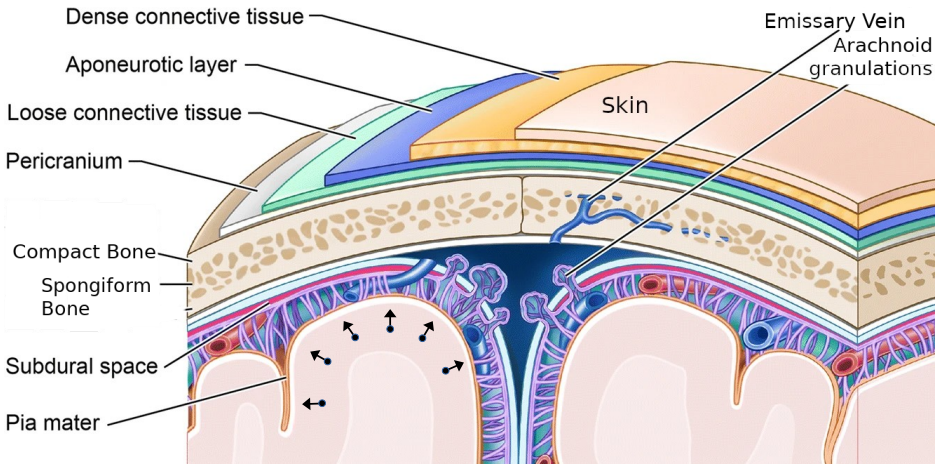

Fig. 2.5 Anatomical features in the head, where many of the significant layers in the scalp and skull are labelled. The small black arrows are sources of current (dipoles) located in the grey matter with an orientation normal to the half way plane drawn between the pia matter and the white matter (the layer below the dipoles). Adapted from Gomez et al. (2018) under the Creative Commons Attribution 4.0 International License [78].

as half way between the white matter and the pia matter (see Fig. 2.5). The orientation of the dipole moment is usually set as normal to the plane, meaning there can be a range of orientations. These orientations are referred to as tangential or radial with respect to the head, imagining it as roughly spherical with the centre of the head being the centre of the sphere. A characteristic difference between EEG and MEG is that MEG is insensitive to radially directed dipoles [4, 36]. Once a source space is constructed, the forward solution for each dipole can be calculated and stored.

We can then compare each forward solution with real, measured potentials from the EEG data (e.g. the potential on each channel at 140 ms in Fig. 2.4). Finding the lowest error between the measured data and the forward solutions and selecting the corresponding dipole as the current generator is known as the inverse problem (IP). This is explored in more detail in the following chapter.

2.3.3 Head modelling

ESI methods rely on computational models of the head that include anatomical structure and physical properties such as the electrical conductivity field [117]. Clearly, the structure is at least to some extent an individualised characteristic. However, recent work by McCann et al. (2020) has shown that the electrical conductivity field also varies significantly between

individuals [116]. Therefore, there remains an open research question: to what degree does this structural and conductive variability between individuals affect the accuracy of ESI?

Anatomical Structure of the Head

The human head is comprised of many tissues, each with different proportions and electrical properties. Certain assumptions about these tissues are often made when creating a computational representation of the head. Traditionally, one of the significant simplifications has been to model the head as a simple sphere with multiple tissue layers (often three: scalp, skull and brain) represented as shells within the sphere. This has the advantage of not requiring any special knowledge of the subject, which can be costly to obtain. Additionally, exact analytical solutions to the EEG-FP for spherical head models exist [50]. However, it can be shown that realistic head models outperform spherical ones in EEG source localisation in terms of accuracy [176]. Furthermore, subject specific models result in an even greater accuracy in ESI forward and inverse problems over generic atlas models [183]. Standard imaging techniques can be used to obtain this subject specific anatomy such as Magnetic Resonance Imaging (MRI) or Computerised Tomography (CT). The scans from these methods allow many of the tissues to be segmented individually [166, 13]. CT scans provide clear images of the skull, whereas, using MRI, different weightings (T1 and T2) can be applied to highlight a range of soft tissues and even some microstructural information when considering diffusion weighted imaging [98]. Voxel-based segmentation of these tissues using the images is then offloaded to software, for which many tools exist [152, 91]. Naturally, the detail that can be achieved from segmentation is a function of the resolution (number of voxels) of the images being processed, the sensitivity of the imaging technique to specific tissues, any noise that exists in the data and of course the segmentation technique itself. Consequently, identifying each known tissue of the head for use in models quickly becomes intractable with each tissue lying on a scale of difficulty.

To answer the above question, we must therefore consider the feasibility of obtaining each tissue and which reasonable assumptions can be made about the models while carefully assessing the impact of such assumptions. For example, even in realistic models, it is common for the scalp to be modelled as a single homogeneous layer. In reality, the scalp consists of the skin, connective tissue, loose connective tissue, blood vessels, muscle, fat, aponeurosis and periosteum (see Fig. 2.5) [58]. Some work has addressed this assumption, showing that the omission of blood vessels in the brain can impact EEG source localisation by as much as 15 mm [68].

In a similar way, the composition of the skull changes between regions as a result of fatty spongiform bone (also referred to as diploe or marrow) that is contained within

the hard bone skull plates. It has been shown that the electrical conductivity of a skull sample varies significantly depending on the ratio of spongiform bone to compact hard bone [41]. Inclusion of information about the spongiform bone then is crucial to EEG source localisation [115, 49, 143]. Furthermore, it has been shown that boundaries between these bone plates (known as sutures) also greatly influences the conductivity [41]. Sutures contain varying amount of connective tissue and are therefore more conductive than the compact bone either side. Omitting sutures from head models has been demonstrated to increase the error in EEG [115]. Additionally, each suture fuses at a different age, further motivating the use of individual head models being utilised.

Below the skull it is sensible to separate the remaining tissues into a highly conductive cerebrospinal fluid (CSF) compartment, a gray matter compartment and a white matter compartment owing to demonstrations in improvements of source localisation for both EEG and MEG [123]. The layer of tissue immediately subcranial is known as the dura. It is not often considered in head models due to difficulty in its segmentation from standard imaging techniques, however it has been shown to impact accuracy of source localisation in EEG when considered [142].

Another important consideration is the modelling of the electrodes in EEG and particularly the position of the electrodes. For high-density EEG with a net of electrodes placed on the scalp, it can be shown that the error induced by modelling the position of the electrodes incorrectly is significant, especially when considering deeper brain sources [190, 48].

Electrical Conductivity Field

After refining the head model to capture the most important tissues, our attention then turns to assigning the physical property of electrical conductivity to each. A common practice in the field is to use population averages gleamed from the literature to inform this choice. However, recent work has shown that the conductivity of specific tissues varies significantly between individuals [116]. Therefore, using population averages could be a misguided assumption and these conductivities should likely be subject specific. We then return to our original question and explore the degree to which these individual conductivity changes effect ESI accuracy.

The compact bone of the skull has a much lower conductivity than the other tissues of the head which causes it to act as an shield to electrical brain activity [116]. This has lead to the early observation that misspecification of this conductivity can lead to large errors for source localisation and even early recommendations that the sutures should be modelled [131].

For source reconstruction of one well characterised SEP in the primary somatosensory cortex (P20), it has been show that uncertainties in the scalp and skull conductivities can lead

to localisation errors of the order of centimeters [184, 9]. Furthermore, that same study found uncertainties in the grey and white matter in the brain significantly influenced the strength and orientation of the reconstructed source. A more recent global analysis of the source space produced similar findings, and additionally found that the strength of the influence from each tissue was dependent on the location of the source [187].

The conductivity of a tissue can also be modelled as anisotropic, meaning the conductivity of the tissue in one direction is different than another. For head tissues, the directions are often defined as radial and tangential to the centre of the head. When the anisotropy of white matter (extracted from diffusion weighted MRI data) is included in head models, it has been shown to influence the potential fields measured on the scalp in EEG [88, 193]. Furthermore, when considered as a single compartment (i.e. without spongiform bone), modelling the skull as anisotropic has also be shown to be influential [193].

The need for individualised electrical conductivities for modelling in EEG is evident. One method for estimating these conductivities is parametric (or bounded) electrical impedance tomography (pEIT). This technique is non-invasive, relatively affordable, and crucially uses most of the same hardware utilised by EEG, giving it the potential to be widely accessible [169].

2.4 Parametric Electrical Impedance Tomography

Electrical Impedance Tomography (EIT) is a method for reconstructing the electrical conductivity field within an object. This technique requires a set electrodes to be placed on the surface of the object of interest. While a subset of the electrodes are responsible for injecting and extracting current, the complementary subset are used to measure the electrical potential on the surface. The measurements from the latter set of electrodes are then used to infer the conductivity distribution within the object by simulating the current travelling through the object. This requires a computational model of the object and a discretisation scheme applied to the model for the conductivity to be reconstructed on to. The number of conductivities to solve and the number of electrodes to measure from determines how ill-posed the method is. The level of ill-posedness can split EIT into two camps; parametric EIT (pEIT) and imaging EIT. Parametric EIT (also known as bounded EIT) aims to reconstruct the conductivity of predefined compartments, therefore requiring only a handful of conductivities to be resolved, making it less ill-posed. However, imaging EIT requires the conductivity to be reconstructed at each discretised point in the model, making it much more ill-posed depending on the discretisation.

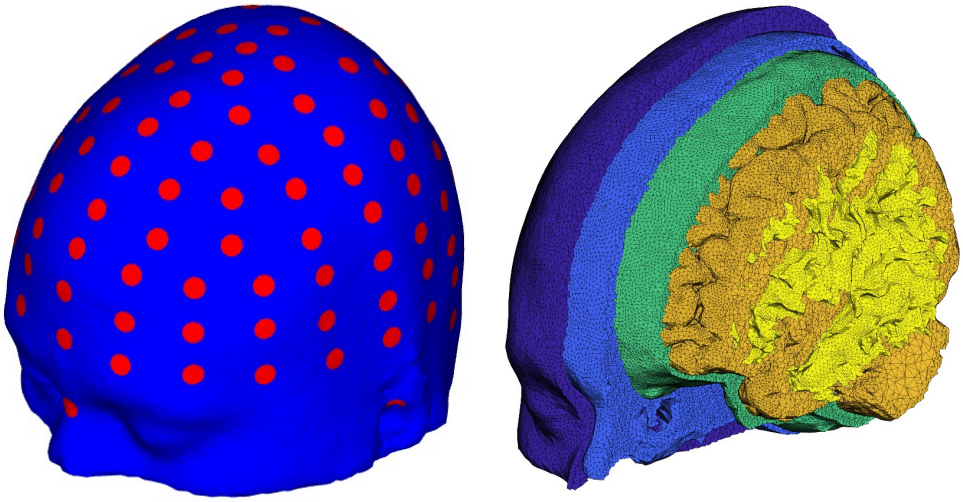

Fig. 2.6 Computational model of the head used in pEIT and EEG. Electrodes are red circles on the surface of the scalp on the left and the various tissue compartments are shown in different colours on the right.

Both modalities consist of a FP and a IP. The FP involves the simulation of the current through the model, which encodes a conductivity distribution, geometry of the domain, and electrode setup. The IP then tunes the conductivity distribution in the FP until its solution is closest to the real measurements.

The imaging EIT modality is forced to use coarse discretisations to reduce the number of conductivities to find, and produces low resolution images of the conductivity inside an object. Additionally, many stabilisation techniques are used to converge to a solution. For example, Principle Component Analysis (PCA) with basis constraints have been used to provide prior information of the conductivity distribution [177]. Other stabilisation methods include Tikhonov regularisation [178], Bayesian methods [99] and total variation [34]. Applied to the human body, imaging EIT has been adopted widely for applications such as lesion detection and stroke detection in the brain, as well as being used as an ESI technique [12, 1]. The open-source software EIDORS has been developed for EIT image reconstruction [3] with these uses in mind.

When applied to the human body, parametric EIT is a relatively affordable and non-invasive method for estimating the conductivities of tissue compartments in a human head [92]. Using an array of electrodes placed on the scalp, a small current is injected and extracted from a subset and the electrical potential is measured on the complementary set. This technique seeks to estimate the conductivities of head tissues (e.g., scalp, skull, etc.)

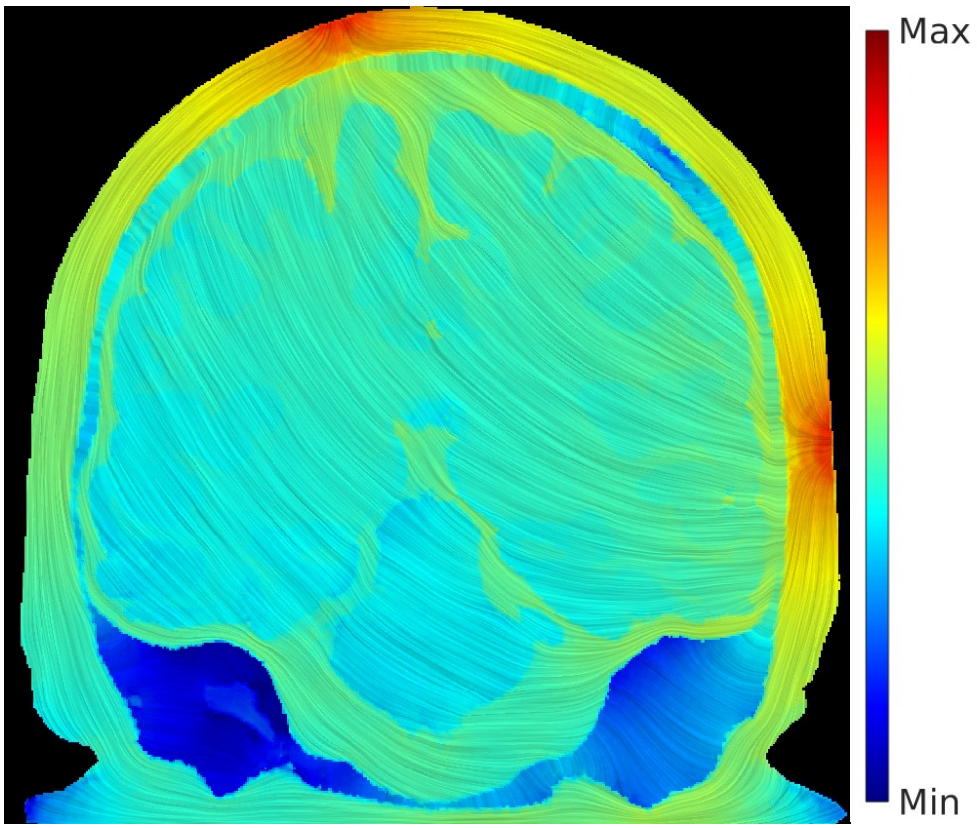

Fig. 2.7 Current flow between two electrodes through a coronal cross section of a head model, calculated using Line Integral Convolution. Red indicates large current flow and blue indicates small current flow.

by simulating forward solutions for sets of parameters and tuning the set to best match the electrical potential measurements taken. This allows one to characterise an individualised conductivity field in the head. An example of the fine discretisation used in parametric EIT models can be seen in Fig. 2.6. Notice the high resolution that allows the anatomical structure to be represented in detail. As mentioned previously, this structure can be obtained from standard imaging techniques.

For the problem discussed in the previous section, pEIT therefore provides a useful tool towards creating more individualised head models for ESI methods. Parametric EIT has already been used to effectively estimate skull, scalp, CSF and brain conductivities in highly realistic models [66, 63] as well as CSF for simple head models [67]. Tissue anisotropy has also been considered and estimated [60].

However, the computational complexity of the EIT-FP makes the technique prohibitive in some cases, especially for highly realistic and finely discretised models. To understand this, we now describe the mathematical formulation of the pEIT problem.

2.5 Chapter Summary

This chapter has introduced the problem that motivates the work in this thesis, starting from the reasons behind studying the electricity in the brain and ending at the limitations in the techniques designed to study it. The main points of this chapter can be summarised as follows:

- Postsynaptic potentials in the dendrites of neurons are thought to be the primary contributors of potential measured on the scalp. These current generators can be modelled as an electrical dipole and are vital for studying the function and dysfunction of the brain.
- Reconstructing the position and orientation of the current sources is called source localisation and the methods of EEG and MEG have this capability. High-resolution EEG in particular is a non-invasive and relatively affordable technique that involves electrodes placed on the scalp that measure the electrical potential, which is used for reconstructing sources of current.
- Of special interest to the research community are a class of evoked potentials called somatosensory evoked potentials. These occur due to current sources in the somatosensory cortex in the brain when a stimulus is applied to the body. These responses are well defined, easily reproducible and have generally high signal-to-noise ratios.
- EEG relies heavily on computational head models that should reflect the anatomy and conductivity of an individuals head. Conductivities not only vary between individuals in most tissue in the head but have been shown to have a great influence on source reconstruction in EEG.
- Parametric EIT can estimate the conductivities of an individual and has been successful in extracting the conductivities of the scalp and skull. This utilises most of the same equipment as EEG with minor modifications and uses an injection/extraction of a small amount of current from two more electrodes. However, the computational cost associated with this technique prevents it from wide spread adoption and limits its ability to estimate deeper tissues.

Chapter 3

Mathematical Formulation of pEIT and EEG

3.1 Overview

Chapter 1 outlined the motivation for using EEG to examine electrical activity in the brain. Also highlighted were the challenges related to obtaining the highly realistic head models that are essential for accurate ESI methods such as EEG. Parametric EIT was then introduced as a useful tool to aid the construction of these realistic models through characterising the electrical conductivity field. However, the computational burden of pEIT was noted as a significant disadvantage of the technique. In this chapter, the mathematical formulations of pEIT and EEG are derived to emphasise the sources of the computational complexity, to further understand how they may be addressed.

3.2 Forward Problems

3.2.1 Boundary Value Problems and Bioelectromagnetism

In Chapter 2, we saw that both pEIT and EEG are split into FPs and IPs. For both methods, we require a mathematical description of the FP to understand and simulate the propagation of current through a head model. The derivations for both of these mathematical formulations are very similar given that each problem is governed by the same fundamental laws of electromagnetism. Therefore, before rigorously treating each problem separately, we consider the generation of two simple boundary value problems in a biological setting that form the foundations of the pEIT-FP and the EEG-FP and highlight the difference between each.

In the pEIT-FP and EEG-FP, we are interested in calculating the electric potential u for a given point $\boldsymbol{r}$ in a three dimensional medium with a conductivity σ, as a result of a given injection of current with current density $\boldsymbol{J}$. Specifically, we are interested in the potential at points which have been identified as electrodes. To create a formulation for these potentials, we can utilise the fundamental laws of electromagnetism known as Maxwell's equations. These equations can first be simplified however by making a quasi-static approximation, meaning that the equations are not dependent on time. This approximation is justified, given that the frequencies seen in bioelectric phenomena, and of that used in pEIT, are generally below 100 Hz. With frequencies this low, it can be shown that the time dependent derivatives in Maxwell's equations are small compared to the other terms [94]. Therefore, after removing the time dependent derivatives, we are left with the quasi-static Maxwell's equations:

$$\nabla \times \boldsymbol{E} = 0, \tag{3.1a}$$

$$\nabla \times \boldsymbol{B} = \mu \boldsymbol{J}, \tag{3.1b}$$

$$\nabla \cdot \boldsymbol{B} = 0, \tag{3.1c}$$

$$\nabla \cdot \boldsymbol{D} = \rho \tag{3.1d}$$

where,

$$\boldsymbol{D} = \varepsilon \boldsymbol{E}, \tag{3.2a}$$

$$\boldsymbol{J} = \sigma \boldsymbol{E}, \tag{3.2b}$$

and $\boldsymbol{J}$ is the current density in A/m^2 where A is Amps (and eq. (3.2b) is Ohm's Law), $\boldsymbol{E}$ is the electric field in V/m where V is Volts, $\boldsymbol{B}$ is the magnetic field in Teslas (T), $\boldsymbol{D}$ is the electric displacement in C/m^2 where C is Coulomb, μ is the magnetic permeability (here the permeability of free space), ε is the electric permeability and σ is the conductivity. From 3.1a we note that $\boldsymbol{E}$ can be expressed as the gradient of a scalar potential, given that the curl of a gradient of a scalar is zero. Therefore, with a scalar potential u,

$$\boldsymbol{E} = -\nabla u. \tag{3.3}$$

Now, in the case of EEG, our goal is to find the potential as a result of a source of current in the brain. Therefore, we must add an external current source, called the primary current or impressed current to eq. (3.2b), which becomes

$$\boldsymbol{J} = \boldsymbol{J}^p + \sigma \boldsymbol{E}, \tag{3.4}$$

where $\boldsymbol{J}^p$ is the primary current density. Then, taking the divergence of eq. (3.1b) and then using eq. (3.3) and eq. (3.4), we obtain

$$\begin{aligned} \nabla \cdot \nabla \times \boldsymbol{B} &= \nabla \cdot \boldsymbol{J}, \\ 0 &= \nabla \cdot \boldsymbol{J}^p + \nabla \cdot \sigma \boldsymbol{E} \\ -\nabla \cdot \sigma(-\nabla u) &= \nabla \cdot \boldsymbol{J}^p \\ \nabla \cdot (\sigma \nabla u) &= \nabla \cdot \boldsymbol{J}^p \end{aligned} \tag{3.5}$$

which is a form of the Poisson equation. For a homogeneous, infinite and unbounded medium, and a dipolar current source, there is an analytical solution to eq. (3.5) [151, 197], given as

$$u(\boldsymbol{r}) = \frac{\boldsymbol{J}^p \cdot \boldsymbol{R}}{4\pi\sigma \boldsymbol{R}^3}, \tag{3.6}$$

where $R = |\boldsymbol{r} - \boldsymbol{r}_0|$ and $\boldsymbol{r}_0$ is the the position of the current dipole.

Since we are aiming to model the head, we would like to find the potential within a bounded domain Ω (e.g., a sphere), that has a surface $\partial\Omega$ where we can place electrodes. In this case, we must impose homogeneous Neumann boundary conditions on $\partial\Omega$ that specifies that no current is leaving the domain. Together with eq. (3.5), the following boundary value problem is formulated

$$\nabla \cdot (\sigma(\boldsymbol{r}) \nabla u(\boldsymbol{r}) = \nabla \cdot \boldsymbol{J}^p(\boldsymbol{r}) \quad \text{in } \Omega, \tag{3.7a}$$

$$\sigma(\boldsymbol{r}) \frac{\partial u(\boldsymbol{r})}{\partial \hat{\mathbf{n}}} = \langle \sigma(\boldsymbol{r}) \nabla u(\boldsymbol{r}), \hat{\mathbf{n}} \rangle = 0 \quad \text{on } \partial\Omega, \tag{3.7b}$$

where $\hat{\mathbf{n}}$ is a unit vector normal to $\partial\Omega$. This constitutes the basic formulation of the EEG-FP. A very similar derivation can be found for the pEIT-FP. In this case, there is no external current source in the interior of the domain, meaning that $\boldsymbol{J}^p$ in eq. (3.5) can be set to zero to obtain $\nabla \cdot (\sigma \nabla u) = 0$. However, the Neumann boundary conditions need to be adapted to include the normal component (w.r.t $\partial\Omega$) of the current density $\boldsymbol{J}(\boldsymbol{r})$ reflecting the injection of current through two or more points on the boundary. Therefore, in the pEIT case, the boundary value problem becomes

$$\nabla \cdot (\sigma(\boldsymbol{r}) \nabla u(\boldsymbol{r}) = 0 \quad \text{in } \Omega, \tag{3.8a}$$

$$\sigma(\boldsymbol{r}) \frac{\partial u(\boldsymbol{r})}{\partial \hat{\mathbf{n}}} = \langle \sigma(\boldsymbol{r}) \nabla u(\boldsymbol{r}), \hat{\mathbf{n}} \rangle = \boldsymbol{J}(\boldsymbol{r}) \quad \text{on } \partial\Omega. \tag{3.8b}$$

Analytical solutions exist for both of these boundary value problems when considering a spherical domain, with multiple layers (i.e., concentric shells) and/or isotropic conductiv-

ities [56, 50, 25, 52, 66]. However, these solutions are complex and sometimes computationally expensive. Additionally, for more complex shapes, that reflect the anatomy of the head, neither problem has analytical solutions. In this scenario, the domain is not smooth enough to obtain a sufficiently differentiable solution and therefore a classical solution does not exist [59]. Therefore, we must employ numerical methods to find a solution. One popular approach is the use of finite element (FE) methods to search for a solution. Here, we adopt the FE method due to its flexibility to handle arbitrary compartments in the domain (e.g., tissue compartments in the head), although boundary element method (BEM) could also be employed. This requires deriving a variational formulation (also called a weak formulation) for the problem following the recipe for the Galerkin Finite Element Method. In the next section, we show the derivation of the variational formulation and FE discretisation for eqs. (3.8). In the following sections, we adapt eqs. (3.7) and eqs. (3.8) to reflect more complex modelling assumptions before deriving their variational formulations and corresponding discretisations.

3.2.2 Parametric EIT-FP Formulation

Variational Formulation

To construct a variational formulation we must first restrict our search for the solution to eqs. (3.8) to an appropriate Hilbert space $H^1(\Omega)$ defined by

$$H^1(\Omega) = \{\psi : \Omega \mapsto \mathbb{R} | \psi, \nabla\psi \in L_2(\Omega)\}, \tag{3.9}$$

where the square-integrable functions ψ are part of the Lebesgue Space L_2 and $\mathbb{R}$ is the set of real numbers. The Galerkin method for constructing variational formulations requires that eq. (3.8)a must be multiplied by an appropriate test function $v \in H^1(\Omega)$ before being integrated over the domain. This results in

$$\int_\Omega v\nabla \cdot (\sigma(\boldsymbol{r})\nabla u(\boldsymbol{r}) d\Omega = \int_\Omega \sigma v \cdot \Delta u d\Omega = 0. \tag{3.10}$$

Before continuing, we need to recall the important result of Green's Formula, which can be derived from the divergence theorem (see Johnson (2009) p.26 [97]), that states

$$\int_\Omega \nabla v \cdot \nabla u d\Omega = \int_{\partial\Omega} v\nabla u \cdot \mathbf{n} d(\partial\Omega) - \int_\Omega v \cdot \Delta u d\Omega. \tag{3.11}$$

Then, multiplying by σ obtains

$$\int_{\Omega} \sigma \nabla v \cdot \nabla u d\Omega = \int_{\partial\Omega} \sigma v \nabla u \cdot \mathbf{n} d(\partial\Omega) - \int_{\Omega} \sigma v \cdot \Delta u d\Omega. \tag{3.12}$$

Now, applying eq. (3.10) to eq. (3.12), we can straightforwardly obtain the variational formulation of eq. (3.8), which can now be stated as [60]: Find $u \in H^1(\Omega)$ such that $\forall v \in H^1(\Omega)$

$$\int_{\Omega} \sigma \nabla u \cdot \nabla v d\Omega = \int_{\partial\Omega} v \underbrace{\sigma \nabla u \cdot \mathbf{n}}_{current\ density} d(\partial\Omega) \tag{3.13}$$

where the left-hand side is known as a symmetric positive definite bilinear form $B : H^1 \times H^1 \rightarrow \mathbb{C}$ defined as

$$B(u, v) = \int_{\Omega} \sigma \nabla u \cdot \nabla v d\Omega. \tag{3.14}$$

On the boundary, we have L point-like electrodes. In a traditional pEIT set up, two or more of these electrodes will have a non-zero current applied to them which injects or extracts current from the domain. Due to the point like nature, the current density at electrode l can be described in terms of the total current I_l for that electrode and a Dirac Delta function $\delta_{\boldsymbol{r}_l}$ at the position of the electrode (i.e., $\boldsymbol{J}(\boldsymbol{r}) = \boldsymbol{I}\delta_{\boldsymbol{r}_l}$). The problem can then also be described as described as [84]:

$$B(u, v) = \sum_{l=1}^{L} I_l \delta_{\boldsymbol{r}_l}. \tag{3.15}$$

An example of these point current injections can be seen in Fig. 3.1 for a spherical model, with one injection of current I and one sink of current $-I$. The figure displays the current density for each point in the sphere.

Galerkin Finite Element discretisation

To solve the variational formulation numerically and hence find an approximate solution to u, the domain is discretised. Here, we adopt the finite element (FE) method due to its flexibility to handle arbitrary compartments in the domain (e.g., tissue compartments in the head), although boundary element methods have also been employed for similar problems.

This discretisation of the domain in the FE scheme creates an FE mesh. The elements of the mesh can be any tessellating shape, however, we use tetrahedrons here. The points where elements meet are called nodes. An example of this discretisation is shown in Fig. 3.1 where the model is divided into many tetrahedrons.

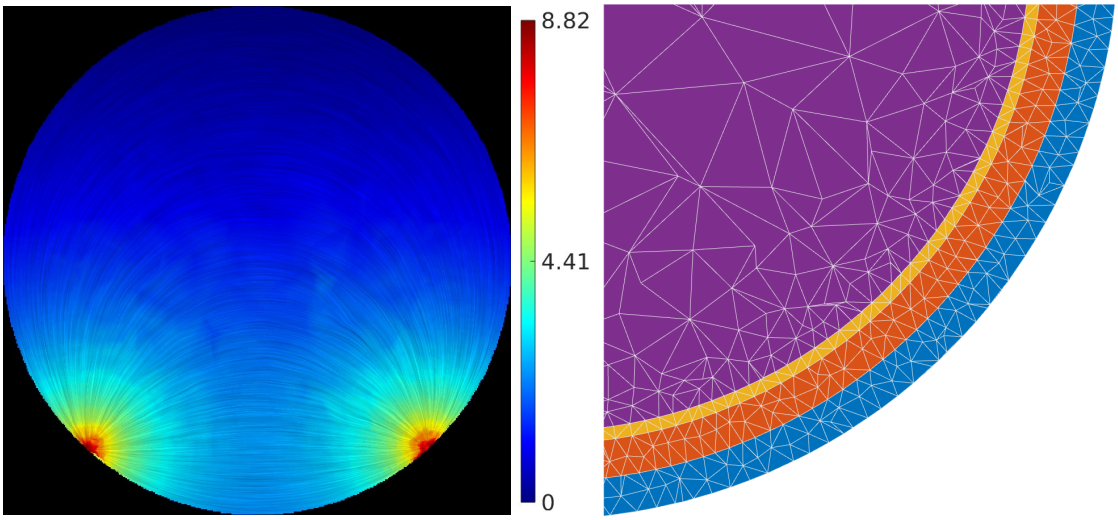

Fig. 3.1 **Left)** The current density (in A/m^2) within a sphere from one injection electrode and one sink electrode placed at the boundary. **Right)** The FEM discretisation on a cross section of a spherical model with concentric shells where the colours correspond to different layers: blue is scalp, orange is skull, yellow is CSF and purple is the brain.

Firstly, a finite-dimensional subspace of the Hilbert Space $V_h \subset H^1(\Omega)$ must be defined with a basis of linear peicewise continuous functions

$$V_h = span\{\psi_0, \psi_1, ..., \psi_n\}, \tag{3.16}$$

where n denotes number of nodes in the FE mesh and the subscript h denotes the resolution of the space (i.e., $h = \max h_i$ where $h_i = n_i - n_{i+1}$, following the FE literature [97]). In this form of Galerkin method, the space where the solution and test functions lie is equivalent. The finite approximation of u in this space is u_h and consists of a linear combination of the basis functions in V_h, expressed as

$$u^h = \sum_{i=1}^{n} \alpha_i \psi_i, \tag{3.17}$$

where $\boldsymbol{\alpha} = \{\alpha_1, ..., \alpha_n\}^T$ is a coefficient vector to be found. Setting $v = \psi_i$ results in a system of equations to solve that can be written as

$$\boldsymbol{K}\boldsymbol{\alpha}^T = \boldsymbol{b}, \tag{3.18}$$

where the matrix $\boldsymbol{K} \in \mathbb{R}^{n \times n}$ is known as the stiffness matrix and $\boldsymbol{b} \in \mathbb{R}^n$ is the right-hand-side vector. For a fine mesh, n is large leading to many equations needed to be solved and therefore

the above system is computationally expensive. Due to the piecewise linear basis functions ψ_i only taking the value 1 at a single node, then searching for the coefficients is effectively the same as searching for the solution. Therefore, to simplify notation later on, the coefficient vector $\boldsymbol{\alpha}$ will be referred to simply as $\boldsymbol{u}_n$. Therefore, eq. (3.18) can be rewritten as

$$\boldsymbol{K}(\boldsymbol{\sigma})\boldsymbol{u}_n(\boldsymbol{\sigma}) = \boldsymbol{b}, \tag{3.19}$$

where the entries to $\boldsymbol{K}(\boldsymbol{\sigma})$ are

$$K_{ij} = \int_\Omega \langle \sigma \nabla\psi_i, \nabla\psi_j \rangle d\Omega, \tag{3.20}$$

and depend on the conductivity values of each compartment $\boldsymbol{\sigma} = \{\sigma_1, \sigma_2, ..., \sigma_P\}$, where P is the number of tissue compartments. In practice, to find these entries, we first calculate eq. (3.20) for each individual tetrahedron element E by integrating only over that element, resulting in a symmetric *element* stiffness matrix $K_E \in \mathbb{R}^{4\times4}$ for each tetrahedron. For each tetrahedron, the contributions from each element stiffness matrix are summed to find the entries to the *global* stiffness matrix.

Once $\boldsymbol{K}(\boldsymbol{\sigma})$ has been constructed, the system in eq. (3.19) can be resolved with a range of fast iterative solvers [59].

Example in a Spherical Head Model

As an illustrative example, we consider a simple spherical model with multiple layers and an outer radius of 10 cm. The layers represent (from outer to inner) the scalp, skull, CSF and brain. In this example, one electrode is chosen to inject a current of 0.25×10^{-3} A and another is chosen to extract a current of -0.25×10^{-3} A. Using the formulation in the previous section, we can calculate the potential in the sphere using FE methods provided the sphere is transformed into a mesh (in our case a tetrahedral mesh). We discretise our sphere with 84,314 nodes, resulting in 485,216 tetrahedral elements. We consider two scenarios. The first is where all layers have a conductivity of 0.3 S/m resulting in a single homogeneous sphere. A cross-section of the sphere with the current density and electric potential in this case are plotted in Fig. 3.1 and Fig. 3.2 respectively. In the second scenario, the layers have different conductivities that are more representative of the head tissues. From outer to inner layers, the conductivities are 0.43, 0.01, 1.79 and 0.33 S/m. The current density and potential are plotted on the cross section of a sphere in Fig. 3.3. Notice how the current largely passes through the scalp layer with relatively high conductivity and how the skull layer “shields" the inner layers from current, resulting in lower potentials in those layers

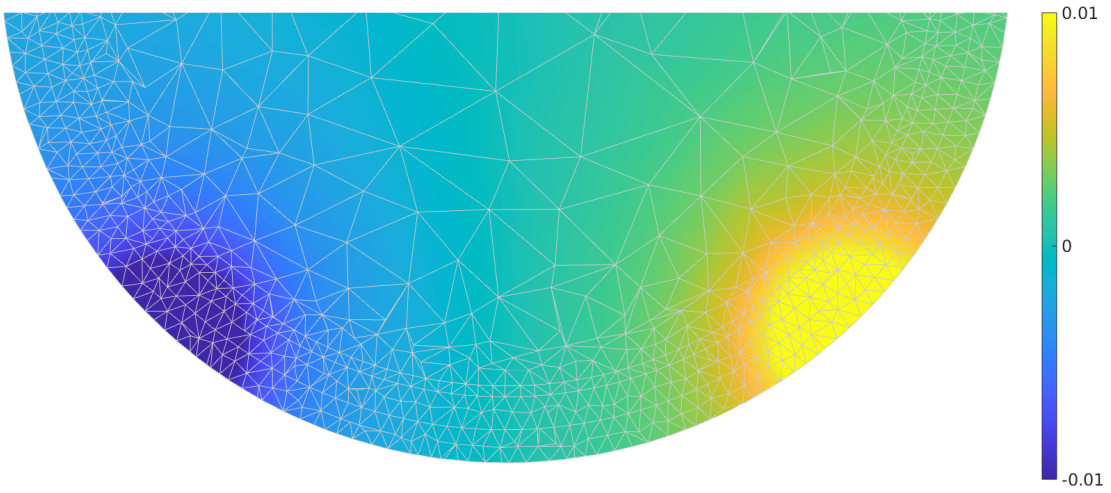

Fig. 3.2 Electric potential throughout a cross-section of homogeneous spherical head model with a conductivity of 0.3 S/m as a result of an injection current of 0.25×10^{-3} A and extraction current of -0.25×10^{-3} A from two electrodes. The potential is calculated using FEM and measured in volts.

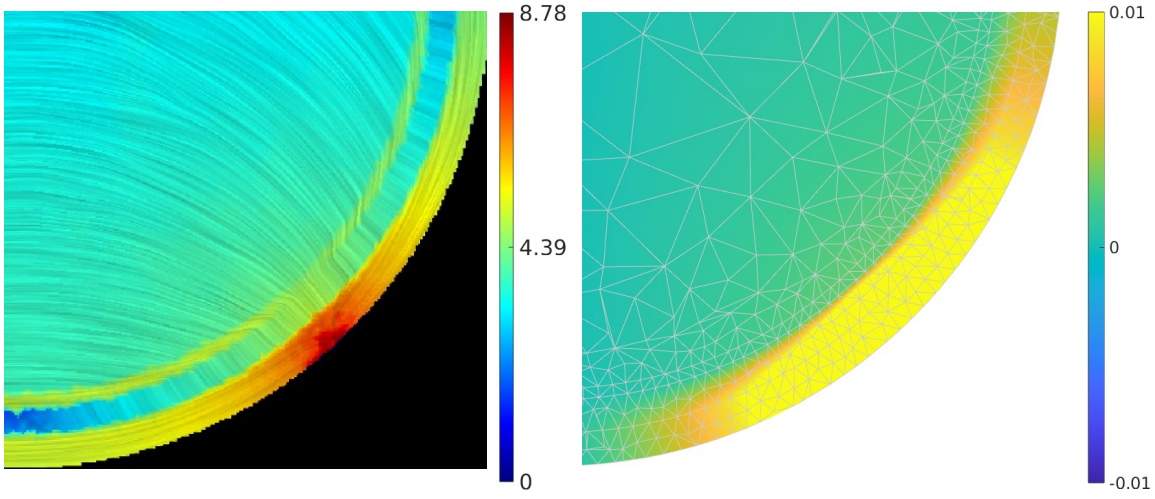

Fig. 3.3 **Left)** The current density (in A/m^2) in a spherical head model with multiple layers of different conductivities due to a current injection of 0.25×10^{-3} A. **Right)** The corresponding potential induced by the current shown to the left, measured in Volts.

compared to the homogeneous case. This represents a fundamental challenge in both the pEIT and EEG methods. The skull acts as an insulating layer to electrical activity, thus making conductivity changes in this layer, highly influential on the potential solution.

Complete Electrode Model

So far, we have considered point electrodes on the surface of the sphere. This form of representation is known as the point electrode model (PEM). In reality, electrodes are typically small discs with a finite area that are placed on the scalp [86]. While the PEM has been shown to be a justifiable assumption for electrodes with a small area [84], in real EIT studies it has been shown that the PEM does not match the measured data to the precision of the measurement devices [102, 162]. With this motivation, the complete electrode model (CEM) was developed to explain the real data. This model incorporates the area and effective contact impedance between each electrode and the scalp into the EIT formulation.

Additionally, modelling the electrodes has a theoretical advantage. For any solution u to the variational formulation, we wish to prove its existence and uniqueness. In the PEM, existence and uniqueness cannot be proven in the Hilbert space used for FE methods (H^1), but rather, a different solution space is required to prove these properties [84]. This is a result of the potentials not being well defined due to being unbounded linear functionals (Dirac Delta functions) [75, 84]. On the other hand, potentials on the electrodes in the CEM are well defined under certain conditions and therefore existence and uniqueness can be proven [162]. An example of the poorly defined potential in the PEM with respect to a well defined potential in the CEM can be seen in Fig. 3.4.

The pEIT-FP considering the CEM will be explored in detail in this section, following closely the work of Somersalo et al. (1992) and Vauhkonen et al. (1999) [162, 179].

The L electrodes $e_l,\ l = 1, ..., L$ are placed on $\partial\Omega$ and each have an associated current I_l flowing across the whole electrode and an effective contact impedance z_l. The electrodes are modelled with a non-negligable area, a finite contact impedance and a potential solution U_l. Consequently, the boundary conditions of the problem are no longer just Neumann and are now mixed, although the formulation of the interior of the domain remains the same. This new formulation is as follows:

$$\nabla \cdot (\sigma(\boldsymbol{r})\nabla u(\boldsymbol{r})) = 0 \quad \text{in } \Omega, \tag{3.21a}$$

$$\sigma(\boldsymbol{r})\frac{\partial u(\boldsymbol{r})}{\partial \hat{\mathbf{n}}} = \langle \sigma(\boldsymbol{r})\nabla u(\boldsymbol{r}), \hat{\mathbf{n}} \rangle = 0 \quad \text{on } \partial\Omega \setminus \cup_{l=1}^{L} e_l, \tag{3.21b}$$

$$u + z_l \sigma(\boldsymbol{r})\frac{\partial u(\boldsymbol{r})}{\partial \hat{\mathbf{n}}} = U_l \quad \text{for } l = 1, ..., L, \tag{3.21c}$$

$$\int_{e_l} \sigma(\boldsymbol{r})\frac{\partial u(\boldsymbol{r})}{\partial \hat{\mathbf{n}}} d(\partial\Omega) = I_l \quad \text{on } e_l, \tag{3.21d}$$

The new boundary conditions stated by eqs. (3.21b) and (3.21d) describe that current can only leave or enter the scalp on the parts labelled as the electrodes e_l and is zero on all

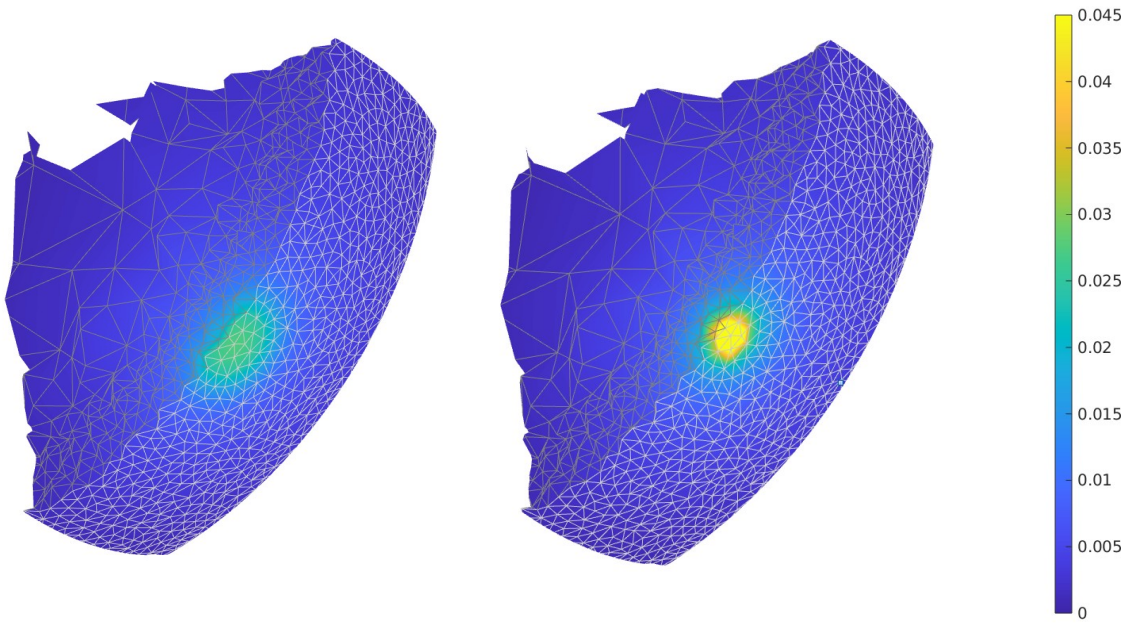

Fig. 3.4 Partial cross-section of a homogeneous sphere of conductivity 0.3 S/m coloured with the electric potential resulting from a current injection of 0.25×10^{-3} A considering the **left)** CEM and **right)** PEM.

other parts of the scalp $\partial\Omega \backslash \cup_{l=1}^{L} e_l$. Additionally, eq. (3.21c) represents the influence of the effective contact impedance on the electrode voltage. In the same way as before, we search for a solution (u, U) to eqs. (3.21), but now must expand the space to include the solution on the electrodes U. A suitable space is the direct sum of H^1 and the set of complex numbers $\mathbb{C}^L$,

$$H = H^1(\Omega) \oplus \mathbb{C}^L. \tag{3.22}$$

This space also contains the test functions in the domain and on the electrodes (v, V). To derive the bilinear form, we follow the same derivation for the PEM up to eq. (3.13) and at this stage, substitute in the new boundary conditions, namely eqs. (3.21b) and (3.21c). Rearranging eq. (3.21c) gives

$$\sigma(\boldsymbol{r}) \frac{\partial u(\boldsymbol{r})}{\partial \hat{\mathbf{n}}} = \frac{1}{z_l}(U_l - u),$$

and combining with eq. (3.21b) gives

$$\sigma(\boldsymbol{r}) \frac{\partial u(\boldsymbol{r})}{\partial \hat{\mathbf{n}}} = \sum_{l=1}^{L} \frac{1}{z_l}(U_l - u).$$

Substituting into eq. (3.13) then provides

$$\int_\Omega \sigma \nabla u \cdot \nabla v d\Omega = \int_{\partial\Omega} v \sum_{l=1}^{L} \frac{1}{z_l}(U_l - u) d(\partial\Omega)$$

which rearranges to

$$\int_\Omega \sigma \nabla u \cdot \nabla v d\Omega + \sum_{l=1}^{L} \frac{1}{z_l} \int_{e_l} (u - U_l) v d(\partial\Omega) = 0. \tag{3.23}$$

Simultaneously, we can combine eqs. (3.21b), (3.21c) and (3.21d), followed by multiplying by the test function for the electrode V_l in the following way

$$\begin{aligned}
\sum_{l=1}^{L} \int_{e_l} \frac{1}{z_l}(U_l - u) d(\partial\Omega) &= I_l \\
\sum_{l=1}^{L} \frac{1}{z_l}(\int_{e_l} (u - U_l) d(\partial\Omega)) + I_l &= 0 \\
\sum_{l=1}^{L} \frac{1}{z_l}(\int_{e_l} (u - U_l) d(\partial\Omega) + z_l I_l) &= 0 \\
\sum_{l=1}^{L} \frac{1}{z_l} V_l(\int_{e_l} (u - U_l) d(\partial\Omega) + z_l I_l) &= 0.
\end{aligned} \tag{3.24}$$

Finally, subtracting eq. (3.24) from eq. (3.23)

$$\begin{aligned}
\int_\Omega \sigma \nabla u \cdot \nabla v d\Omega + \sum_{l=1}^{L} \frac{1}{z_l} \int_{e_l} (u - U_l) v d(\partial\Omega) - \sum_{l=1}^{L} \frac{1}{z_l} V_l(\int_{e_l} (u - U_l) d(\partial\Omega) + z_l I_l) &= 0 \\
\int_\Omega \sigma \nabla u \cdot \nabla v d\Omega + \sum_{l=1}^{L} \frac{1}{z_l} \int_{e_l} (u - U_l) v - V_l(u - U_l) d(\partial\Omega) - \sum_{l=1}^{L} V_l I_l &= 0,
\end{aligned}$$

to obtain the problem: Find $(u, U) \in H$ such that $\forall (v, V) \in H$

$$B((u, U), (v, V)) = \sum_{l=1}^{L} I_l V_l, \tag{3.25}$$

where $B((u,U),(v,V))$ is the bilinear form $B : H \times H \rightarrow \mathbb{C}$

$$B((u,U),(v,V)) = \int_{\Omega} \sigma \nabla u \cdot \nabla v d\Omega + \sum_{l=1}^{L} \frac{1}{z_l} \int_{e_l} (u - U_l)(v - V_l) d(\partial\Omega). \tag{3.26}$$

For a detailed proof the reader is directed to Somersalo et al. (1992) [162]. As mentioned before, to maintain existence and uniqueness in the solution, a few conditions need to be met. Firstly, we must adapt the space. The problem can be seen using the Lax-Milgram Theorem, where the $B((u,U),(v,V))$ does not satisfy all conditions (see [162]). Qualitatively, there are multiple entries to the form $B((u,U),(v,V))$ that map to the same value in $\mathbb{C}$, and thus, the solutions are not unique. This can be solved by introducing a quotient space which "collapses" the space to remove the duplicate mappings. The quotient space is written as

$$\dot{H} = H/\mathbb{C}. \tag{3.27}$$

Secondly, to guarantee existence and uniqueness of the solution (u,U) we must also add the properties of conservation of charge and determine a reference condition for the electric potentials on the electrodes. The conservation of charge law can be held by ensuring the net current flowing across all electrodes is zero. Mathematically, this is expressed as

$$\sum_{l=1}^{L} I_l = 0. \tag{3.28}$$

The reference can simply be set as an average common reference where the net potential on all electrodes is also zero. This can be written as

$$\sum_{l=1}^{L} U_l = 0. \tag{3.29}$$

Note, an equally valid approach for obtaining a unique solution could also be choosing one electrode to which all other electrodes are referenced (i.e. $U_{ref} = 0$ or $\boldsymbol{U} = [U_1 - U_{ref}, U_2 - U_{ref}, ..., U_{L-1} - U_{ref}]$). In practice, for pEIT and EEG, this is the most common referencing strategy and the chosen electrode is usually assigned to dedicated referenced electrode positioned at the vertex of the head. This will be a point of discussion in Chapter 5.

To discretise the CEM formulation, we must approximate the solution on the electrodes in terms of weighted basis functions in a similar way as before. This is expressed as

$$U^h = \sum_{l=1}^{L} \eta_l \boldsymbol{\phi}_l, \tag{3.30}$$

where $\boldsymbol{\eta} = \eta_1, ..., \eta_L$ is a coefficient vector to be found and the basis vectors are $\phi_1 = \{1, 0, ..., 0\}^T \in \mathbb{R}^L$ and $\phi_2 = \{0, 1, 0, ..., 0\}^T \in \mathbb{R}^L$, etc. Note: these basis vectors do not necessarily satisfy condition (3.29) [179]; however, this can be achieved by simply referencing each potential to the mean or a reference electrode. Setting $V = \phi_i$ results in a system of equations to solve that can be written as

$$\boldsymbol{A}(\boldsymbol{\alpha}, \boldsymbol{\eta})^T = \boldsymbol{b}, \tag{3.31}$$

where $\boldsymbol{A}$ is the stiffness matrix and $\boldsymbol{b}$ is the right-hand-side vector. Similarly to the solution on the nodes, we simplify the notation by referring to the coefficient vectors $(\boldsymbol{\alpha}, \boldsymbol{\eta})$ as $\boldsymbol{u}$. In this way, the system can also be expressed as

$$\boldsymbol{A}(\boldsymbol{\sigma})\boldsymbol{u}(\boldsymbol{\sigma}) = \boldsymbol{b}, \tag{3.32}$$

where,

$$\boldsymbol{A}(\boldsymbol{\sigma}) = \begin{bmatrix} \boldsymbol{K}(\boldsymbol{\sigma}) & -\boldsymbol{B} \\ -\boldsymbol{B}^T & \boldsymbol{C} \end{bmatrix}, \ \boldsymbol{u}(\boldsymbol{\sigma}) = \begin{bmatrix} \boldsymbol{u}_n(\boldsymbol{\sigma}) \\ \boldsymbol{U}(\boldsymbol{\sigma}) \end{bmatrix}, \ \boldsymbol{b} = \begin{bmatrix} \boldsymbol{0} \\ \boldsymbol{I} \end{bmatrix}, \tag{3.33}$$

$\boldsymbol{u}_n(\boldsymbol{\sigma}) \in \mathbb{R}^n$ is the solution vector on the n nodes of the volumetric FE mesh, $\boldsymbol{U}(\boldsymbol{\sigma}) \in \mathbb{R}^L$ is the potential solution on the electrodes and $\boldsymbol{I} \in \mathbb{R}^L$ is the vector of injection currents on the electrodes. The matrices $\boldsymbol{B} \in \mathbb{R}^{n \times L}$ and $\boldsymbol{C} \in \mathbb{R}^{L \times L}$ encode information about the electrodes on the surface of the domain and do not depend on the conductivity. The entries of the matrices $\boldsymbol{K}$, $\boldsymbol{B}$ and the diagonal matrix $\boldsymbol{C}$ are given by [180]

$$K_{ij} = \int_\Omega \langle \sigma \nabla \psi_i, \nabla \psi_j \rangle d\Omega + \sum_{l=1}^{L} \frac{1}{z_l} \int_{e_l} \psi_i \psi_j d(\partial\Omega), \tag{3.34a}$$

$$B_{il} = \frac{1}{z_l} \int_{e_l} \psi_i d(\partial\Omega), \tag{3.34b}$$

$$C_{ll} = \frac{1}{z_l} \int_{e_l} d(\partial\Omega) = \frac{|e_l|}{z_l}, \tag{3.34c}$$

where e_l represents the lth electrode, $|e_l|$ its area, z_l its contact impedance, Ω is the domain (i.e., the head) with boundary $\partial\Omega$, and ψ_i is a basis function on the nodes $i = 1, 2, ..., n$.

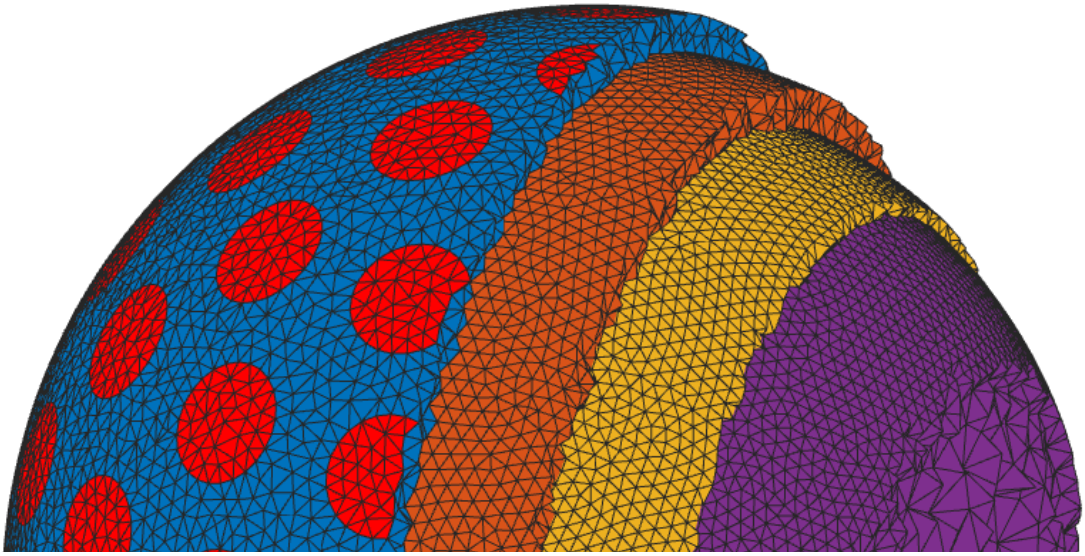

Fig. 3.5 FE mesh of a 4-layered spherical head model (with outer radius 10cm) considering the CEM with electrodes modelled as red circles, with a radius of 2.2cm.

A useful property of the matrix $\boldsymbol{K}(\boldsymbol{\sigma})$ is that, in the case of homogeneous conductivities, it can be linearly decomposed into several constituent stiffness matrices $\boldsymbol{K}_p \in \mathbb{R}^{n\times n}$, each representing a different compartment p in the head model and independent of $\boldsymbol{\sigma}$. Consequently, the matrix $\boldsymbol{A}(\boldsymbol{\sigma})$ can be split into p matrices $\boldsymbol{A}_p \in \mathbb{R}^{(n+L)\times(n+L)}$, i.e.,

$$\boldsymbol{A}(\boldsymbol{\sigma}) = \boldsymbol{A}_0 + \sum_{p=1}^{P} \sigma_p \boldsymbol{A}_p, \tag{3.35}$$

where $\boldsymbol{A}_0$ is a $\boldsymbol{\sigma}$-independent matrix encoding the information from matrices $\boldsymbol{B}$ and $\boldsymbol{C}$ and the second term in eq. (3.34a).

Revisiting our spherical head model example, we implement the CEM on the same tetrahedral mesh as before, while assigning triangles on the mesh surface to specific electrodes. This can be seen in Fig. 3.5, where the triangles coloured red are the electrodes. Each electrode is modelled with an effective contact impedance of 5 Ωm^2 and area of 0.0015 m^2. The current density resulting from injecting a current of 0.25×10^{-3} A into an electrode modelled on a homogeneous sphere and inhomogeneous sphere are shown in Fig. 3.6.

We build the stiffness matrix using volume and area coordinates which are detailed in Appendix A.1.

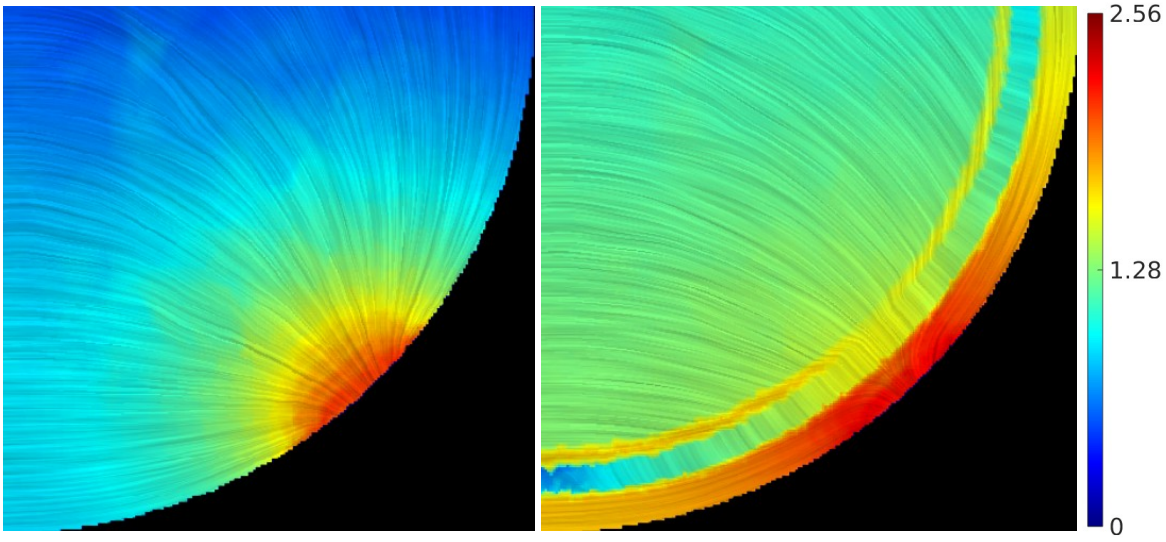

Fig. 3.6 Current density (in A/m^2) from a current injection of 0.25×10^{-3} A using the CEM for **left)** a homogeneous spherical model and **right)** a spherical model with multiple conductivity jumps.

3.2.3 EEG Formulation

The principle difference between pEIT and EEG FP formulations arises from the source of the electrical activity. In pEIT, the current source is two or more electrodes, whereas, in EEG, the current source is the electrical activity in the brain. Most commonly, that electrical activity is mathematically modelled as a point dipolar source, although research has been performed on the use of multipolar sources such as and quadrapoles [186, 25].

Similarly to pEIT, a difficulty occurs with the treatment of the singularity potential caused by the point source. Unfortunately, when deriving the variational formulation in preparation for numerical solutions, one quickly runs into trouble due to the integration terms on the current source. Consequently the solution suffers from a loss of existence and uniqueness in the finite element space. This difficulty arises from the integration of the function $\nabla\delta(\boldsymbol{x})$, which is not well defined. We dealt with this issue of singularity in pEIT by implementing the CEM, removing the point-like source of current. However, for a source in the brain, we require a different strategy to maintain existence and uniqueness.

Numerous ways of tackling this singularity problem have been developed, implemented and compared by accuracy and speed of convergence with modern iterative solvers [194, 107].

Source modelling

One approach, called the partial integration approach, multiplies eq. (3.7a) by a test function and integrates, following the formula for the variational formulation. Both sides are then integrated by parts where the boundary conditions are used to cancel terms. Here, the derivative is absorbed by the test function instead of the Dirac delta function and dipole is approximated on the FE mesh nodes [107, 137].

Another approach is to exchange the dipole for a local distribution of electric monopoles with the same collective moment as the dipole. This is called St. Venant's approach. The vertices of the node in which the source is located and the surrounding nodes are used as the positions of the monopoles [194]. This approach is popular due to its computational speed and is still utilised widely in the field [184, 187].

One other approach is known as Whitney's method. This technique replaces the source term with one that has higher regularity, meaning it is more differentiable, utilising lowest-order Raviart-Thomas basis functions [136, 135, 133, 137].

Another method that handles the singularity by reformulating the EEG-FP entirely is called the subtraction approach. This method splits up the potential and conductivity into a singularity part and correction part. The idea is to solve the FP analytically as if it were an unbounded homogeneous volume conductor with a given conductivity and then use FE methods to solve for a correction potential with correction conductivities [154, 14, 165, 197]. The subtraction approach has benefited from many different implementations, each with varying accuracies and computational costs. These include the projected [194], projected gradient [26], full [57] and analytical [24] subtraction approaches.

It is beyond the scope of this thesis to compare the relative strengths and weaknesses of each source modelling approach mentioned, however, significant work on this can be found in the literature [118, 20, 107, 137]. In chapter 6, we utilised the analytical subtraction approach, due to the existence and uniqueness in the solution, and the generally higher levels of accuracy over other approaches [27].

The subtraction approach

To implement the subtraction approach with the CEM, we follow the work of Beltrachini (2024) [27].

The subtraction approach is founded on the idea that the domain Ω can be split into two complementary subsets. The first is a non-empty set $\Omega^{\infty} \subset \Omega$ surrounding the dipole with a conductivity σ^{∞} and the second is the complementary set $\Omega^{c} \subset \Omega$ with conductivity σ^{c}. This allows the potential to also be split into a singularity potential u^{∞} and a correction potential

u^c. Similarly, the potentials on the electrodes can now be decomposed into their singularity U^∞ and correction U^c counterparts. The conductivities and potentials have the following relations

$$\sigma = \sigma^\infty + \sigma^c, \tag{3.36a}$$

$$u = u^\infty + u^c, \tag{3.36b}$$

$$U = U^\infty + U^c, \tag{3.36c}$$

where u^∞ is the potential in an unbounded homogeneous isotropic volume conductor. Substituting eq. (3.36) into eq. (3.7) produces

$$\begin{aligned}
\nabla \cdot ((\sigma^\infty + \sigma^c)\nabla(u + u^c)) &= \nabla \cdot \boldsymbol{j}^p \\
\nabla \cdot (\sigma \nabla(u^\infty + u^c)) + \nabla \cdot ((\sigma^\infty + \sigma^c)\nabla(u + u^c)) &= \nabla \cdot \boldsymbol{j}^p \\
\nabla \cdot (\sigma \nabla u^c) + \nabla \cdot ((\sigma^\infty + \sigma^c)\nabla u^\infty) &= \nabla \cdot \boldsymbol{j}^p \\
\nabla \cdot (\sigma \nabla u^c) + \nabla \cdot (\sigma^\infty \nabla u^\infty) + \nabla \cdot (\sigma^c \nabla u^\infty) &= \nabla \cdot \boldsymbol{j}^p \\
\nabla \cdot (\sigma \nabla u^c) + \nabla \cdot (\sigma^\infty \nabla u^\infty) - \nabla \cdot \boldsymbol{j}^p &= -\nabla \cdot (\sigma^c \nabla u^\infty).
\end{aligned}$$

Then, utilising the solution to Poisson's equation in an unbounded homogeneous conductor, $\sigma^\infty \nabla u^\infty = \boldsymbol{j}^p$ [197], and applying a similar treatment to the boundary conditions produces the following formulation

$$\nabla \cdot (\sigma \nabla u^c) = -\nabla \cdot (\sigma^c \nabla u^\infty) \quad \text{in } \Omega, \tag{3.37a}$$

$$\sigma \frac{\partial u^c}{\partial \mathbf{n}} = -\sigma \frac{\partial u^\infty}{\partial \mathbf{n}} \quad \text{on } \partial\Omega \backslash \cup_{l=1}^{L} e_l, \tag{3.37b}$$

$$u^c + z_l \sigma \frac{\partial u^c}{\partial \mathbf{n}} - U_l^c = U_l^\infty - u^\infty - z_l \sigma \frac{\partial u^\infty}{\partial \mathbf{n}} \quad \text{for } l = 1, \ldots, L, \tag{3.37c}$$

$$\int_{e_l} \sigma \frac{\partial u^c}{\partial \mathbf{n}} d(\partial\Omega) = -\int_{e_l} \sigma \frac{\partial u^\infty}{\partial \mathbf{n}} d(\partial\Omega) \quad \text{on } e_l. \tag{3.37d}$$

where $U^\infty = A_l^{-1} \int_{e_l} u^\infty d(\partial\Omega)$, $U^c = A_l^{-1} \int_{e_l} u^c d(\partial\Omega)$ on e_l and u^∞ is given in eq. (3.6) in the case of a dipolar source. As with pEIT, the domain is not sufficiently smooth enough for us to obtain an appropriately differentiable solution, meaning a variational formulation of 3.37 is also needed. Our variation formulation is stated as: Find $(u^c, U^c) \in H \; \forall (v, V)$ such that [27]

$$B((u^c, U^c), (v, V)) = l(v, V), \tag{3.38}$$

where $B((u^c, U^c), (v, V))$ is the same as defined in eq. (3.26) and,

$$l((v,V)) = -\int_\Omega \sigma^c \nabla u^\infty \cdot \nabla v d\Omega - \int_{\partial\Omega} \sigma^\infty \nabla u^\infty \cdot \nabla v d(\partial\Omega) \tag{3.39}$$

$$-\sum_{l=1}^{L} \frac{1}{z_l} \int_{e_l} (u^\infty - U_l^\infty)(v - V_l) d(\partial\Omega). \tag{3.40}$$

For the detailed derivation of eq. (3.40), we direct the reader to Beltrachini (2024) [27]. When discretised utilising the same basis functions used for the pEIT problem, this leads to the system of equations

$$\boldsymbol{A}(\boldsymbol{\sigma})\boldsymbol{u}^c(\boldsymbol{\sigma}) = \boldsymbol{b}^{EEG}(\boldsymbol{\sigma}), \tag{3.41}$$

where $\boldsymbol{A}(\boldsymbol{\sigma})$ is the same as in eq. (3.33),

$$\boldsymbol{u}^c(\boldsymbol{\sigma}) = \begin{bmatrix} \boldsymbol{u}_n^c(\boldsymbol{\sigma}) \\ \boldsymbol{U}^c(\boldsymbol{\sigma}) \end{bmatrix}, \ \boldsymbol{b}^{EEG}(\boldsymbol{\sigma}) = \begin{bmatrix} \boldsymbol{b}(\boldsymbol{\sigma}) \\ \mathbf{0} \end{bmatrix}, \tag{3.42}$$

$\boldsymbol{u}_n^c(\boldsymbol{\sigma}) \in \mathbb{R}^n$ is correction potential at each node in the FE mesh, $\boldsymbol{U}^c(\boldsymbol{\sigma}) \in \mathbb{R}^L$ is the correction potential at the L electrodes, $\mathbf{0}$ is a vector of L zeros and $\boldsymbol{b}(\boldsymbol{\sigma})$ is the conductivity-dependent source vector. $\boldsymbol{b}(\boldsymbol{\sigma})$ is formed by the inputs [27]

$$\boldsymbol{b}_i(\boldsymbol{\sigma}) = -\frac{1}{4\pi\sigma^\infty} \int_{\mathrm{T}_k} \langle \boldsymbol{\sigma}^c \nabla g(\boldsymbol{r}), \nabla \psi_i \rangle d\boldsymbol{r} - \frac{1}{4\pi} \int_{T_k} \psi_i \langle \nabla g(\boldsymbol{r}), \boldsymbol{n} \rangle d\boldsymbol{r} \tag{3.43}$$

$$-\sum_{l=1}^{L} \frac{1}{z_l} \int_{e_l} \psi_i (u^\infty(\boldsymbol{r}) - U_l^\infty) d(\partial\Omega) \ \text{ for } \ i = 1, ..., n, \tag{3.44}$$

where $g(\boldsymbol{r})$ is $\boldsymbol{q} \cdot \boldsymbol{R} R^{-3}$. The difficulty now becomes integrating the non-linear terms introduced by the singularity potential. Three approaches have been implemented to tackle this. The projected subtraction approach is so-called because it projects the infinity potential onto the finite element space, leading to an inherent approximation error [197]. The full subtraction approach utilises quadrature schemes to solve the integrals, which has been verified for varying orders of quadrature [57]. The analytical subtraction approach uses Gauss theorems to transform the integrals down to 1 dimension where analytical solutions can be found [24]. For details on the theory and implementation of these methods, the reader is directed to the corresponding publications by Dreshler et al. (2009) [57] and Beltrachini (2019) [24], respectively.

To calculate $\boldsymbol{b}_i(\boldsymbol{\sigma})$, we use the analytical subtraction method for the first two terms in eq. (3.40) and then the full subtraction method for the final term. We chose a combination

of the analytical and full subtraction approaches given the low relative errors achieved by both [57, 24]. To achieve these low errors however, it is worth noting that the mesh resolution must be high (of the order of 500k nodes or more) [107]. We respect both of these constraints with our EEG simulations in Chapter 6.

3.3 Dual Problem

3.3.1 Leadfield and Transfer Matrices

The previous chapter mentioned a source space containing the dipoles of interest, defined within the grey matter. Before solving the IP for EEG, the FP considering each dipole as its source must be solved, to find the potential at each electrode. Typically, a source space can contain thousands of dipoles and the potential at the electrodes for each is stored in an $L \times m$ matrix called the leadfield matrix, which we denote as $\boldsymbol{L}_f$. Given that each FP consists of solving a large system of equations (eq. (3.41)) with dimensions equal to the number of nodes in the FE mesh, generating the leadfield matrix is extremely computationally intensive task. Therefore, generating an individual leadfield matrix with personalised geometry and conductivities is prohibitive, leading to localisation errors in the IP.

One trick for alleviating this problem has been the utilisation of a transfer matrix $\boldsymbol{T}$. This matrix encodes the relationship of the source site to the electrodes, allowing the potential at each electrode for a source to be calculated with simple (and fast) matrix multiplications [107, 196, 191, 135]. For the complete electrode model, the transfer matrix is related to the stiffness matrix by

$$\boldsymbol{K}\boldsymbol{T}^T = \boldsymbol{B}, \tag{3.45}$$

where $\boldsymbol{K}$ and $\boldsymbol{B}$ are the same as in eq. (3.33). The leadfield matrix can then be found using [135]

$$\boldsymbol{L}_f = (\boldsymbol{T}\boldsymbol{B} - \boldsymbol{C})^{-1}\boldsymbol{T}\boldsymbol{b}, \tag{3.46}$$

where $\boldsymbol{b}$ is the same as in eq. (3.42) Now, computing the transfer matrix requires only $L \times 1$ linear systems (eq. (3.45)) to solve, instead of the m linear systems needed to calculate the leadfield from the FPs. This results in a substantial reduction in computational cost to calculate the leadfield matrix, although for a high number of electrodes in use is still a substantial task.

To the best of our knowledge, the transfer matrix approach has only been developed for the PEM with the subtraction approach, and only one implementation in the CEM, which

considered Whitney basis functions in the source vector [135]. However, for the reasons mentioned, we wish to use the subtraction approach with a theoretically rigorous treatment.

3.3.2 Adjoint Method

Recently, a mathematically rigorous approach has been presented that links the pEIT-FP and the EEG-FP by describing the pEIT-FP as the adjoint problem for the EEG-FP considering the CEM. This has the same effect as the transfer matrix approach of reducing the systems to solve from many EEG-FPs (the number of sources) to the few pEIT-FPs (the number of electrodes minus one). Crucially, this method maintains existence and uniqueness of the solution.

For many problems in the physical sciences, partial differential equations are solved numerically over a domain (e.g. similar to the EEG-FP) in the interest of finding only a specific output rather than the entire solution itself. Often, these problems have *adjoint* or *dual* problems, that are connected in some way to the output of interest. Intuitively, the solution to the adjoint problem can be thought of as the sensitivity of the output to perturbations in the source of the original problem (the *primal* problem) [75]. For a detailed description on adjoint methods the reader is directed to Giles and Süli (2002). In this section we follow the work of Beltrachini (2024) [27] to show that pEIT is the adjoint problem to EEG, and furthermore, how the ROM-pEIT can enable new capabilities for EEG as a technique.

When evaluating the EEG-FP, we are only interested in the electrical potential on the electrodes and specifically the differences between electrodes and a reference electrode. The entire solution u^c is in fact of little use. Suppose that we can describe a linear functional $m(u^c, \boldsymbol{U}^c)$, that contains only the correction potential on the electrodes. Then, we can reformulate eq. (3.38) for source j into our primal problem (P): Find $(J_p^{(j)}, (u^c, \boldsymbol{U}^c)^{(j)}) \in \mathbb{R} \times \dot{H}$ such that

$$J_p^{(j)} = m((u^c, \boldsymbol{U}^c)^{(j)}) + l^{(j)}(v, \boldsymbol{V}) - B((u^c, \boldsymbol{U}^c)^{(j)}, (v, \boldsymbol{V})) \; \forall (v, \boldsymbol{V}) \in H \text{ for } j = 1, ..., N_s, \tag{3.47}$$

where N_s is the number of sources and

$$m(u^c, \boldsymbol{U}^c)^{(j)} = U_l^c - U_k^c \text{ for } l = 1, ..., L-1, \, l \neq k, \tag{3.48}$$

and U_k^c is the correction potential on the kth electrode, which is the reference electrode. This can obviously be prohibitive given N_s can be in the region of 30,000 for a refined source

space. However, by introducing the dual problem of the EEG-FP, we are able to reduce the number of problems to solve from N_s down to $L-1$, realising a significant saving in computational cost. Firstly, it is important to note that eq. (3.48) can also be described more generally as the following

$$m(u^c, \boldsymbol{U}^c)^{(j)} = \sum_{i=1}^{L} I_i^{(l)} U_i^{c(l)} \text{ for } l = 1, ..., L-1, \, l \neq k, \tag{3.49}$$

where $I_i^{(l)}$ is a weight on the $U_i^{c(l)}$ (being 1 at l and -1 at k for the special case of eq. (3.48)). The dual problem (D) for the EEG-FP can be stated as: Find $(J_d, (z, \boldsymbol{Z})) \in \mathbb{R} \times \dot{H}$ such that [75]

$$J_d^{(j)} = m(w, \boldsymbol{W})^{(l)} + l^{(j)}(z, \boldsymbol{Z}) - B((w, \boldsymbol{W}), (z, \boldsymbol{Z})^{(l)}) \; \forall (w, \boldsymbol{W}) \in H, \text{ for } l = 1, ..., L-1, \tag{3.50}$$

where

$$B((w, \boldsymbol{W}), (z, \boldsymbol{Z})^{(l)}) = m(w, \boldsymbol{W})^{(l)}, \tag{3.51}$$

and therefore

$$B((w, \boldsymbol{W}), (z, \boldsymbol{Z})^{(l)}) = \sum_{i=1}^{L} I_i^{(l)} W_i^{c(l)} \text{ for } l = 1, ..., L-1, \, l \neq k. \tag{3.52}$$

Now, recalling from Somersalo et al. (1997) that the pEIT-FP considering the CEM is equivalent to eq. (3.52), if we chose $m(w, \boldsymbol{W}) = \sum_{i=1}^{L} I_i W_i$, and where the injection currents are 1 and -1 on the lth and kth electrode for $l = 1, ..., L-1$. From the Primal-Dual Equivalence Theorem it can be shown that $J_p = J_d$([75], Theorem 2.5) when $(z, \boldsymbol{Z})$ and $(u^c, \boldsymbol{U}^c)$ are unique solutions, given that $J_p = m(u^c, \boldsymbol{U}^c)$ and $J_d = l(z, \boldsymbol{Z})$. Therefore, we find that solving (D) requires solving $L-1$ pEIT-FPs. This is a dramatic reduction in computational complexity from problem (P).

3.4 Inverse Problems

3.4.1 Parametric EIT-IP

Parametric EIT is an ill-posed inverse problem (IP) that results in estimates of the electrical conductivities of tissue compartments. To solve the IP, multiple pEIT forward problems (FPs) need to be solved. As seen in the previous section, the FP solution consists of the simulated signals from the measurement electrodes and these are dependent on the head

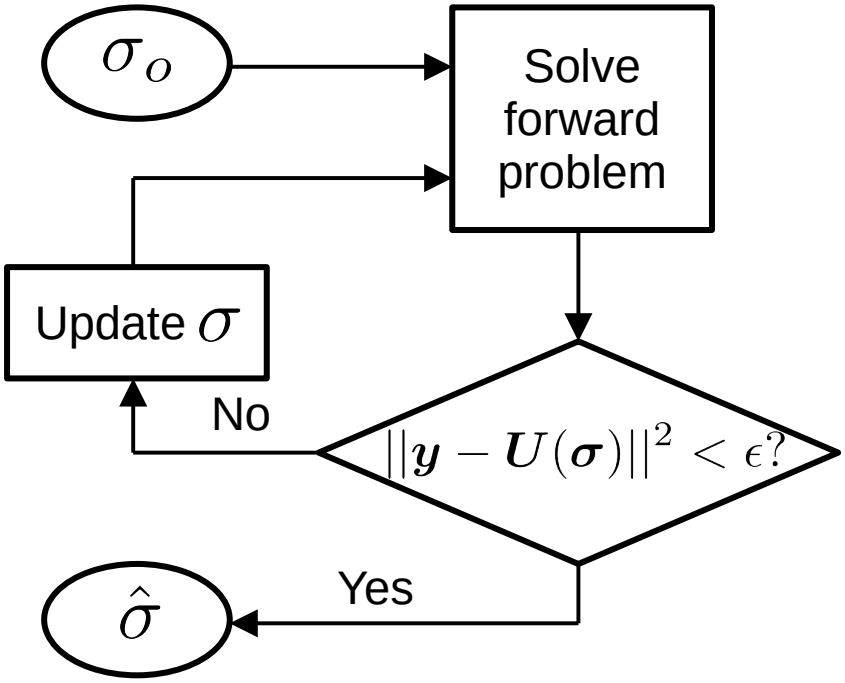

Fig. 3.7 Flow chart of the traditional implementation of the inverse problem for pEIT. Here, ϵ refers to a stopping threshold, $\boldsymbol{\sigma_0}$ is the initial conductivity guess and $\hat{\boldsymbol{\sigma}}$ is the estimated conductivity value. Note that each loop requires at least a full calculation of the forward problem.

model geometry and conductivities. A set of tissue conductivities are used to construct an FP before its solution is compared to a set of real measurements taken. The set of conductivities is then tuned utilising an error metric to find the set of conductivities that produce an FP solution that most closely matches the real signals. More specifically, this is done by iteratively minimising the squared error between the measurements $\boldsymbol{y} \in \mathbb{R}^L$ and the conductivity-dependent simulated signals $\boldsymbol{U} \in \mathbb{R}^L$ on L electrodes. Mathematically, this is generally expressed as

$$\hat{\boldsymbol{\sigma}} = \arg\min_{\boldsymbol{\sigma}} \{(\boldsymbol{y} - \boldsymbol{U}(\boldsymbol{\sigma}))^T (\boldsymbol{y} - \boldsymbol{U}(\boldsymbol{\sigma}))\}, \tag{3.53}$$

where $\hat{\boldsymbol{\sigma}}$ are the estimated conductivities [60]. This results in an optimisation process that requires the calculation of one or more FPs at each iteration and then updating $\boldsymbol{\sigma}$ based on the error and the optimisation technique used (Fig. 3.7). The number of FPs required at each iteration and the number of iterations needed for convergence on a solution are dependent on the optimisation technique used and the complexity of the solution space. For

realistic 6-compartment head models, considering all compartments and the interior-point optimisation technique this can be of the order of thousands.

The computational load of the IP clearly rises significantly if the FP becomes computationally intense. With the number of FPs required to solve, this can quickly make the IP intractable. This is particularly the case for refined realistic head models, where the FP becomes computationally intensive (taking many minutes to solve on a single PC). Working within this constraint, researchers are currently forced to consider only a subset of the compartments in the model (often the skull or scalp). Since the conductivity of all tissues appear to vary, ideally, we would like to consider all of the tissue compartments. With this motivation, the following sections examine, in detail, the pEIT-FP and its implementation.

3.4.2 EEG-IP

In EEG, the inverse problem consists of reconstructing the current source(s) responsible for the potential measured on the electrodes. In distributed source models, source amplitudes stored in a matrix $\boldsymbol{S}$ are estimated for each dipole in the source space, resulting in a distribution of sources that contribute to a signal. Many algorithms have been formulated to solve for this distribution, most of which are based on minimum norm estimations (MNE) with varying constraints or regularisation [150, 164]. The minimum norm approach exhaustively searches the leadfield matrix for the highest inverse least-squares solution with the measurement potentials.

One popular approach is the low resolution electromagnetic tomography algorithm (LORETA), which uses a weighted minimum norm approach with a Laplacian operator, producing a spatially smooth solution [128]. In chapter 5 we use the standardised LORETA (sLORETA) algorithm, which is formulated as follows [129]: If the measured potentials are stored in the vector $\boldsymbol{y} \in \mathbb{R}^L$, finding the corresponding source amplitudes requires solving the problem

$$\min(||\boldsymbol{y} - \boldsymbol{L}_f\boldsymbol{S} - c\mathbf{1}||_2^2 + \lambda||\boldsymbol{S}||_2^2) \tag{3.54}$$

where c is the potential at the reference electrode, $\mathbf{1} \in \mathbb{R}^L$ is a vector of ones and λ is a Tikhonov regularisation parameter. This regularisation achieves a zero-error localisation in a noise-less scenario with the solution

$$\hat{\boldsymbol{S}} = \boldsymbol{L}_f{}^T\boldsymbol{H}[\boldsymbol{H}\boldsymbol{L}_f\boldsymbol{L}_f{}^T\boldsymbol{H} + \lambda\boldsymbol{H}]^\dagger\boldsymbol{y}, \tag{3.55}$$

where $\hat{\boldsymbol{S}}$ are the estimated source amplitudes (usually sparse), † is the Moore-Penrose pseudoinverse,

$$\boldsymbol{H} = \boldsymbol{I} - \frac{1}{L}, \tag{3.56}$$

and $\boldsymbol{I} \in \mathbb{R}^{L \times L}$ is the identity matrix. The matrix $\boldsymbol{H} \in \mathbb{R}^{L \times L}$ is an operator that re-references the potentials in the leadfield matrix to the average common reference (AR).

With noise-free measurement data, sLORETA can localise sources exactly, meaning a zero localisation error, and far better localisation error than other similar methods even in noisy data [129]. Additionally, in the presence of structured biological noise and measurement noise, sLORETA has no bias in the localisation [130]. These properties make sLORETA an attractive option for source localisation and we will use it for the EEG inverse problem in later chapters.

3.5 Chapter Summary and Problem Statement

In this chapter, the mathematical foundations of the pEIT and EEG forward and inverse problems have been outlined. Firstly, it was shown that the IP for pEIT requires multiple successive FPs to converge on a vector of conductivities σ for each tissue compartment in a head model. Then it was shown that FP solutions require a large linear system of equations to be solved, with the same dimensions as the nodes in the FE mesh of the head model. Combined with the number of FPs needing to be solved, this makes pEIT highly computationally expensive.

In a similar way, the EEG IP was described as requiring as many FPs as the number of sources in a source space, which can be of the order of thousands. Although the use of a transfer matrix can reduce this computational burden, this still requires as many FPs to be solved as the number of electrodes minus one. Given the system to solve is the same size as pEIT, the same problem occurs and computational cost of generating a leadfield matrix to use in the IP for EEG is substantial.

For both pEIT and EEG, the FP is dependent on the head model, specifically its geometry and conductivity field. When combined with the knowledge from the previous chapter regarding the importance of individual head models in ESI and the impact of its variation amongst the population, the difficulty with performing personalised pEIT and EEG IPs is clear.

The key contribution of this thesis is the application of a dimensionality reduction technique called reduced order modelling (ROM) to both of these techniques. After a training phase this technique allows the solution of the pEIT and EEG forward problems in real-time

for any set of tissue conductivities in a head model. The following chapter will detail a new framework, incorporating ROM into pEIT and EEG, with subsequent experimental validation.

Chapter 4

Reduced Order Modelling for parametric Electrical Impedance Tomography: a new framework

4.1 Overview and Commentary

In Chapter 2, we introduced the method of pEIT and its value in characterising head tissues. In Chapter 3, we outlined the mathematical foundations of both the FP and IP, highlighting the computational complexity that makes the technique prohibitive in the case of refined head models. With this motivation in mind, we apply a method for reducing this complexity in the current chapter, utilising a technique called reduced order modelling (ROM). The mathematical basis for this method is detailed before the error between the FP solution with ROM and the original FP solution is assessed. This chapter focuses on the suitability of ROM for the pEIT-FP, while the following chapter explores the use of the ROM-pEIT-FP in the IP, by evaluating its performance in real and synthetic data.

This chapter has been adapted and extended from a publication provisionally accepted by the Journal of Neural Engineering: Matthew R. Walker, Mariano Fernández-Corazza, Sergei Turovets and Leandro Beltrachini, Electrical Impedance Tomography Meets Reduced Order Modelling: a Framework for Faster and More Reliable Conductivity Estimations. Leandro Beltrachini contributed to the conceptualisation and programming of the work in this chapter. All other work is that of the author of this thesis. Further details, beyond those included in the publication, have been added to this chapter.

4.2 Introduction

Considering the CEM and an FE implementation, the dimensions of the system to solve for the pEIT-FP (eq. (3.32)) is the number of nodes in the FE mesh plus the number of electrodes modelled on the scalp. Clearly, the more refined the mesh, the larger the number of nodes and therefore the larger the system to solve. Finding a solution this system typically involves the use of an iterative solver such as the preconjugate gradient (PCG) method with preconditioners [59]. While PCGs with lumped diagonal preconditioners have been implemented on graphics processor units (GPUs) in order to highly parallelise this workload [90], the most common implementation is with lower and upper (LU) preconditioners on single threaded processors - central processor units (CPUs) - which can take several minutes to complete.

Given that the pEIT-IP requires multiple conductivity-dependent FPs to be calculated, the computational effort required to solve the IP can be prohibitive in the case of highly refined head models. Furthermore, with little or no *a priori* knowledge about the difference in conductivity between individuals, the FPs must be computed for any point in a parameter space $\mathscr{P}$. To give an idea of the scale of the problem, we consider a brief example. Under current implementations with a gradient-assisted optimisation [63], the IP typically consists of 75 or more FPs (see following chapter) for a 3-parameter search (i.e., where $\mathscr{P}$ is 3 dimensional) before convergence. For a refined head model with an FE discretisation with 800k nodes and 133 electrodes, the FP with its gradient calculations take approximately 1500 seconds on a standard PC (Intel Core i5 CPU). This totals to an IP of the order of 30 hours for a single electrode pair.

In the next two chapters, we propose and implement the use of reduced order modelling (ROM) to significantly decrease the dimensionality of the pEIT-FP and therefore minimise its computational load when being solved. Crucially, this solution can be found for any point in $\mathscr{P}$, allowing the IP to be solved utilising this reduced pEIT-FP instead of the full-order pEIT-FP. This current chapter focuses on the theoretical background and construction of the reduced model of the pEIT-FP. Importantly, this technique is verified by assessing the accuracy of the reduced model solutions by comparison with the full-order solutions across a wide parameter space.

4.3 Introduction to Reduced Order Modelling

ROM is a mathematically rigorous technique to efficiently build a low-dimensional model mapping changes in a set of conductivities to changes in the solution of eq. (3.32) [139]. This model is constructed in an offline phase using a relatively small number of $N << (n+L)$

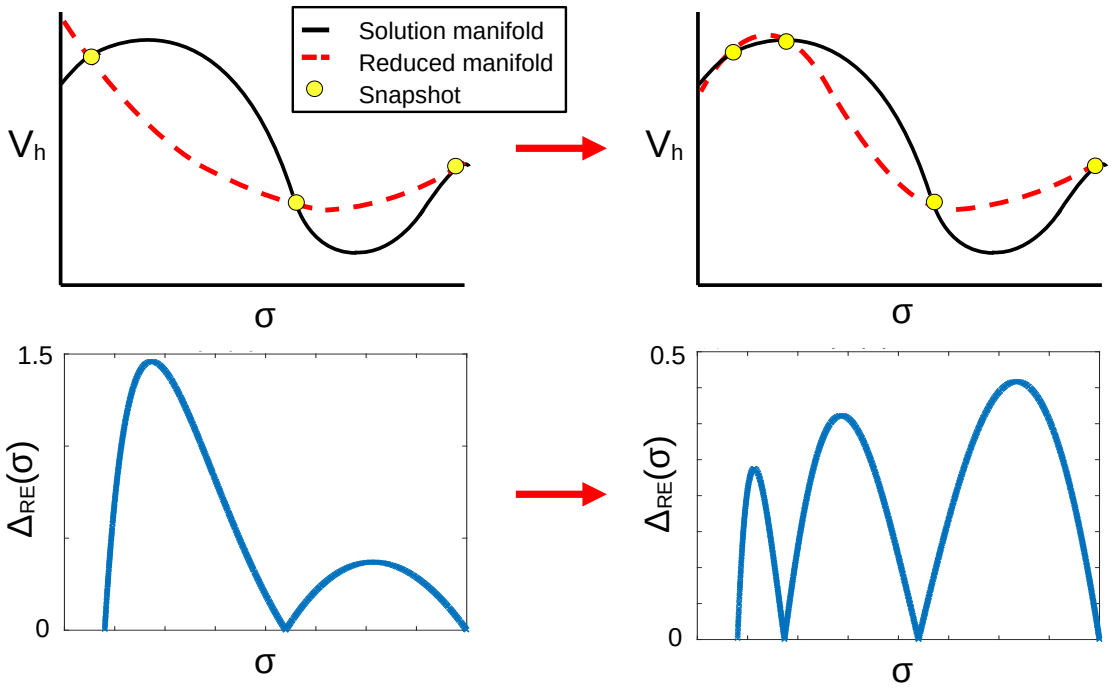

Fig. 4.1 Illustration of an example reduced manifold construction when moving from three snapshots (left) to four snapshots (right). Notice that the reduced manifold resembles the solution manifold more closely after the fourth snapshot is added. Also displayed is the relative error bound across parameter space demonstrating how a new snapshot is chosen.

strategically selected solutions of eq. (3.32) with specific conductivities, which are then used in the 'online' phase to find rapid solutions for any set of conductivities.

Taking advantage of the affine decomposition (see eq. (3.35)), massively reduced versions of the $\boldsymbol{A}_p$ and $\boldsymbol{A}_0$ matrices and vector $\boldsymbol{b}$ can be formed. These are formed by building a reduced basis space with a dimensionality of N and projecting $\boldsymbol{A}_p$, $\boldsymbol{A}_0$ and $\boldsymbol{b}$ onto the space, obtaining the N-dimensional $\boldsymbol{A}_N^p$, $\boldsymbol{A}_N^0$ and $\boldsymbol{b}_N$. These matrices can be stored, allowing the assembly of a reduced system in the online phase at any point in the P-dimensional parameter space $\mathscr{P} \in \mathbb{R}^P$ (i.e., for any set of conductivities) by simple multiplication and addition. This new system, containing only a handful of simultaneous equations, can be solved in real-time, resulting in a reduced-basis solution $\boldsymbol{u}_N \in \mathbb{R}^N$. This vector is transformed back into an n-dimensional solution $\boldsymbol{u}_a \in \mathbb{R}^{n+L}$ that approximates the solution of the high-dimensional system $\boldsymbol{u}$. Put another way, the solutions $\boldsymbol{u}$ in V_h for each point in parameter space make up a solution manifold. This manifold is approximated by the reduced manifold made of the approximate solutions $\boldsymbol{u}_a$. An example of these manifolds in a single dimensional parameter space is given in Fig. 4.1. Before describing the process of projecting the reduced matrices, we turn to constructing our reduced basis space and defining its matrix representation.

The reduced basis space is built using a number of full-order solutions, called snapshots, which are selected strategically across $\mathscr{P}$. Judiciously choosing the points with which to build the reduced model is done by employing a greedy algorithm. A distinguishing feature of ROM is the presence of a rigorous upper bound $\Delta(\boldsymbol{\sigma})$ on the error of the approximate solutions, which guides the greedy algorithm in the snapshot selection, acting as a proxy for the error [139]. This bound on the error can be calculated almost instantly for any given point in $\mathscr{P}$ and can therefore efficiently explore the space to guide the next snapshot point. During each iteration of the greedy algorithm, the bound is calculated for a finite sample set $\Xi \subset \mathscr{P}$ and a snapshot is calculated using the conductivity set that minimises it. Ξ is chosen to represent the entire P-dimensional space $\mathscr{P}$. An example of the bound being used to select the position of a snapshot is shown in Fig. 4.1. Utilising the bound to select the snapshots presents two advantages. Firstly, it allows an extremely quick assessment of the maximum error attainable at a fine discretisation of $\mathscr{P}$. Secondly, it can be used as a stopping criterion for certifying the maximum error in $\boldsymbol{u}_a$ [139]. The relationship between the *a posteriori* relative error [RE($\boldsymbol{\sigma}$)] for a given point in $\mathscr{P}$ and the *a posteriori* relative error bound [$\Delta_{RE}(\boldsymbol{\sigma})$] is [139]

$$\mathrm{RE}(\boldsymbol{\sigma}) \triangleq \frac{||\boldsymbol{u}(\boldsymbol{\sigma}) - \boldsymbol{u}_a(\boldsymbol{\sigma})||_{L_2}}{||\boldsymbol{u}_a(\boldsymbol{\sigma})||_{L_2}} \leq \frac{\Delta(\boldsymbol{\sigma})}{||\boldsymbol{u}_N(\boldsymbol{\sigma})||_{L_2}} \triangleq \Delta_{RE}(\boldsymbol{\sigma}). \tag{4.1}$$

The reduced model takes the form of a reduced-basis space, built using the snapshots calculated by the greedy algorithm. To obtain the reduced system, the full-order stiffness matrices are projected on the space during the offline phase. This reduced-basis space is represented by the matrix $\mathbb{V} \in \mathbb{R}^{(n+L)\times N}$. To construct the orthonormal basis, $\mathbb{V}$ we perform a Gram-Schmidt orthonormalisation on a snapshot, before adding it to the orthonormal basis iteratively. We begin by selecting a random parameter vector $\boldsymbol{\sigma}_1 \in \Xi$ and computing the full-order solution $\boldsymbol{u}(\boldsymbol{\sigma}_1)$. The first basis vector for the orthonormal space is simply the first snapshot, which is a full-order solution (i.e., $\boldsymbol{\zeta}_1(\boldsymbol{\sigma}_1) = \boldsymbol{u}(\boldsymbol{\sigma}_1)$). Thereafter, the orthonormalised solutions $\boldsymbol{\zeta}_j(\boldsymbol{\sigma})$ for the jth snapshot are concatenated,

$$\mathbb{V} = [\boldsymbol{u}(\boldsymbol{\sigma}_1), \boldsymbol{\zeta}_2(\boldsymbol{\sigma}_2), ..., \boldsymbol{\zeta}_N(\boldsymbol{\sigma}_N)], \tag{4.2}$$

such that $\{\boldsymbol{\sigma}_1, \boldsymbol{\sigma}_2, ..., \boldsymbol{\sigma}_N\} \subset \Xi$. Also known as the transformation matrix, $\mathbb{V}$ relates the projected stiffness matrix $\boldsymbol{A}_N(\boldsymbol{\sigma}) \in \mathbb{R}^{N\times N}$ and projected independent vector $\boldsymbol{b}_N(\boldsymbol{\sigma}) \in \mathbb{R}^N$ with the full-order versions through the expressions [139]

$$\boldsymbol{A}_N(\boldsymbol{\sigma}) = \mathbb{V}^T \boldsymbol{A}(\boldsymbol{\sigma})\mathbb{V}, \;\; \boldsymbol{b}_N = \mathbb{V}^T \boldsymbol{b}, \tag{4.3}$$

where, substituting in eq. (3.35), $\boldsymbol{A}_N(\boldsymbol{\sigma})$ becomes

$$\boldsymbol{A}_N(\boldsymbol{\sigma}) = \underbrace{\mathbb{V}^T \boldsymbol{A}_0 \mathbb{V}}_{\boldsymbol{A}_N^0} + \sum_{p=1}^{P} \sigma_p \underbrace{\mathbb{V}^T \boldsymbol{A}_p \mathbb{V}}_{\boldsymbol{A}_N^p}. \tag{4.4}$$

This results in the reduced system to solve

$$\boldsymbol{A}_N(\boldsymbol{\sigma})\boldsymbol{u}_N(\boldsymbol{\sigma}) = \mathbf{b}_N, \tag{4.5}$$

where $\boldsymbol{u}_a(\boldsymbol{\sigma}) = \mathbb{V}\boldsymbol{u}_N(\boldsymbol{\sigma})$. It is clear from eq. (4.3) that, as $N << (n+L)$, the dimensions of the resulting system are massively reduced, requiring significantly fewer operations to solve. Ultimately, this means that a FP can be calculated at any point in $\mathscr{P}$ almost instantly. Fig. 4.2 shows a flowchart of the greedy algorithm, demonstrating the construction of $\mathbb{V}$.

4.3.1 Notation

For clarity of exposition, we define some commonly used terms in this thesis chapter. The term *full-order* or *high-fidelity* refers to high-dimensional vectors, matrices or systems, that arise from the discretisation of the FP. These are not given any special notation unless clarity is needed, in which case they are marked with an h (e.g., the FE space V_h or stability factor interpolation point β_h [see following section]). The low-dimensional vectors, matrices and systems generated as a result of ROM, are noted with an N to indicate their dimension is that of the number of snapshots taken in the greedy algorithm (e.g., the solution to the reduced system $\boldsymbol{u}_N$). The term *reduced model* is used to refer to the collection of matrices and vectors used to generate reduced solutions (i.e., $\mathbb{V}$, $\boldsymbol{A}_N^p$, $\boldsymbol{A}_N^0$ and $\boldsymbol{b}_N$).

4.3.2 The Error Bound

This section addresses the basic construction and implementation of the error bound $\Delta(\boldsymbol{\sigma})$ seen in eq. (4.1). This $\boldsymbol{\sigma}$-dependent parameter is calculated (in this work) for 6000 points in $\mathscr{P}$, which forms the sample train Ξ, in each iteration of the greedy algorithm. To ensure the efficiency of its calculation, a familiar computational splitting schema and interpolation method are employed, also covered here.

Error Bound Derivation

For pEIT with CEM, deriving the bound requires some special treatment, deviating from that presented in Quarteroni et al. (2016). This difference arises from the fact that the stiffness

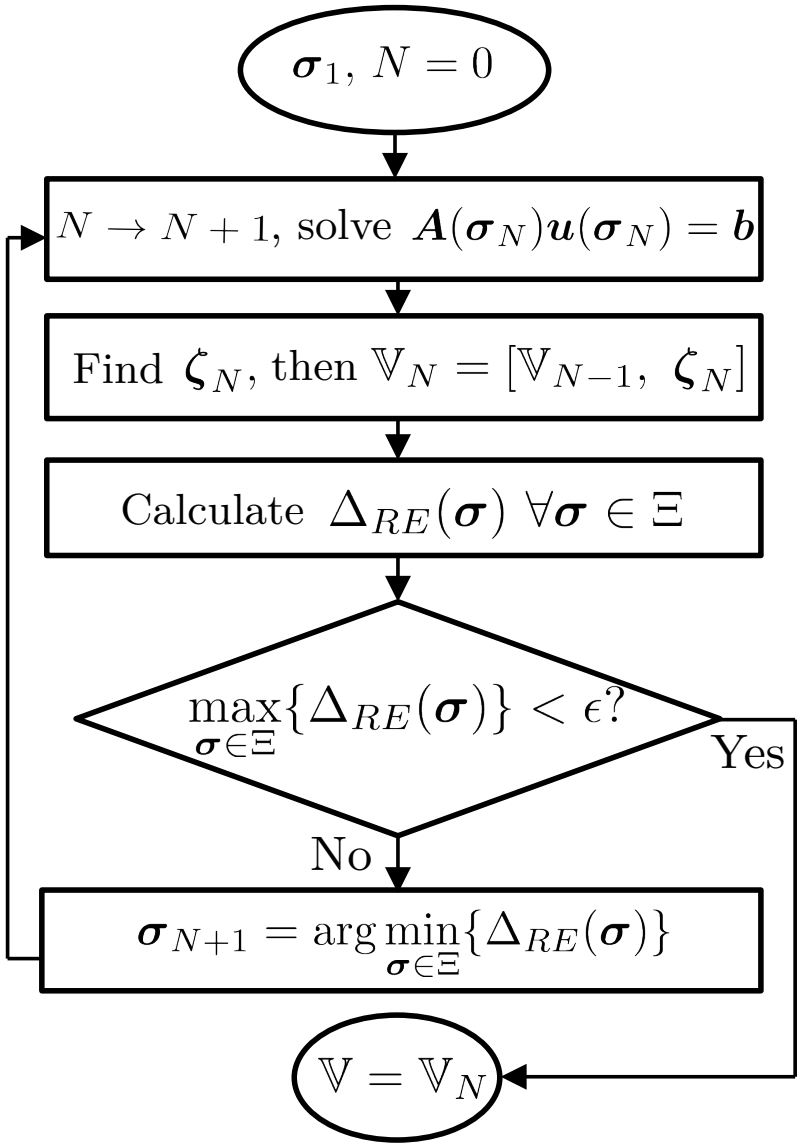

Fig. 4.2 Greedy algorithm used in the offline training phase for ROM where ϵ is some stopping threshold.

matrix $\boldsymbol{A}(\boldsymbol{\sigma})$ in our case is rank deficient, meaning its rank r is smaller than its smallest dimension (with the number of linearly independent columns or rows). This difference ultimately effects the calculation of the stability factor.

The bound is derived by first defining the error and the residual of the reduced solution projected onto the full-order space. The error $\boldsymbol{e}(\boldsymbol{\sigma})$ is defined as $u(\boldsymbol{\sigma}) - \mathbb{V}u_N(\boldsymbol{\sigma})$ and related

to the residual by [eq. (3.74) in Quarteroni et al. (2016)]

$$\boldsymbol{A}(\boldsymbol{\sigma})\boldsymbol{e}(\boldsymbol{\sigma}) = \boldsymbol{r}(\boldsymbol{\sigma}) = \boldsymbol{b} - \boldsymbol{A}(\boldsymbol{\sigma})\mathbb{V}\boldsymbol{u}_N(\boldsymbol{\sigma}). \tag{4.6}$$

To isolate the error term this relation can be rearranged. For the full rank solution, this equation is multiplied by the inverse of $\boldsymbol{A}(\boldsymbol{\sigma})$. However, due to the low rank we instead use the Moore-Penrose psuedoinverse denoted as $\boldsymbol{A}(\boldsymbol{\sigma})^\dagger$ [77], obtaining

$$\boldsymbol{e}^{ls}(\boldsymbol{\sigma}) = \boldsymbol{A}(\boldsymbol{\sigma})^\dagger \boldsymbol{r}(\boldsymbol{\sigma}), \tag{4.7}$$

where $\boldsymbol{e}^{ls}(\boldsymbol{\sigma})$ is the least squares solution of the system. Using the singular value decomposition (SVD) we can decompose $\boldsymbol{A}(\boldsymbol{\sigma})^\dagger$ into $\boldsymbol{V}(\boldsymbol{\sigma})\boldsymbol{\Sigma}(\boldsymbol{\sigma})^\dagger \boldsymbol{U}(\boldsymbol{\sigma})^T$ [p. 117 in Quarteroni et al. (2016)], where $\boldsymbol{V}(\boldsymbol{\sigma})$ and $\boldsymbol{U}(\boldsymbol{\sigma})$ are the right and left orthogonal vectors associated with matrix $\boldsymbol{A}(\boldsymbol{\sigma})$ and $\boldsymbol{\Sigma}(\boldsymbol{\sigma})^\dagger$ is a diagonal matrix containing the inverse of the singular values of the matrix, i.e. $\boldsymbol{\Sigma}(\boldsymbol{\sigma}) = diag(\kappa_1, ..., \kappa_r, 0, ..., 0)$ and $\boldsymbol{\Sigma}(\boldsymbol{\sigma})^\dagger = diag(\frac{1}{\kappa_1}, ..., \frac{1}{\kappa_r}, 0, ..., 0)$. It is important to note here that performing SVD on a rank deficient matrix results in r singular values $(\kappa_1, ..., \kappa_r)$ followed by one or more (e.g. $(n+L)-r$ in this case) zero values. Taking the L_2 norm of each side of equation (4.7) and using the properties of the norm [see eq. (1.16) in Quarteroni et al. (2007) [140]] results in

$$||\boldsymbol{e}^{ls}(\boldsymbol{\sigma})||_2 \leq ||\boldsymbol{\Sigma}(\boldsymbol{\sigma})^\dagger||_2 \, ||\boldsymbol{r}(\boldsymbol{\sigma})||_2. \tag{4.8}$$

Given that, for any matrix, the L_2 norm is equal to the largest singular value of a matrix [eq. (6.2) in Quarteroni et al. (2016)], the term $||\boldsymbol{\Sigma}(\boldsymbol{\sigma})^\dagger||_2$ becomes $\kappa_{max}(\boldsymbol{\Sigma}(\boldsymbol{\sigma})^\dagger)$ which as can we see from its definition will be $1/\kappa_r$ leading us to $\kappa_{min}^{-1}(\boldsymbol{A}(\boldsymbol{\sigma}))$ where the minimum singular value is the smallest nonzero singular value. This results in the error bound

$$||\boldsymbol{e}^{ls}(\boldsymbol{\sigma})||_2 \leq \frac{||\boldsymbol{r}(\boldsymbol{\sigma})||_2}{\kappa_{min}(\boldsymbol{A}(\boldsymbol{\sigma}))} = \Delta(\boldsymbol{\sigma}). \tag{4.9}$$

where $\kappa_{min}(\boldsymbol{A}(\boldsymbol{\sigma}))$ is called the stability factor $\beta_h(\boldsymbol{\sigma})$. Given that our test and solution spaces are the same and $\boldsymbol{A}(\boldsymbol{\sigma})$ is symmetric, finding the smallest singular value is equivalent to finding the smallest eigenvalue and therefore $\kappa_{min}(\boldsymbol{A}(\boldsymbol{\sigma}))$ can be expressed as the generalised eigenvalue problem [139]

$$\beta_h(\boldsymbol{\sigma}) = \lambda_{min}(\mathbb{X}_h^{-1/2}\boldsymbol{A}(\boldsymbol{\sigma})\mathbb{X}_h^{-1/2}), \tag{4.10}$$

where $\mathbb{X}_h \in \mathbb{R}^{(n+L)\times(n+L)}$ is the matrix representation of the norm. The norm we use in this work is the L_2 norm, whose matrix representation is an identity matrix $\boldsymbol{I}_{(n+L)\times(n+L)}$. We

solved this generalised eigenvalue problem using the BLEIGIFP MATLAB toolbox [141]. Crucially, the smallest non-zero eigenvalue was then selected from the results as the stability factor. However, selecting the smallest non-zero eigenvalue was not trivial. Limitations in computer precision leading to numerical errors meant the zero valued eigenvalues in fact had very small non-zero values. We chose the smallest eigenvalue that was part of a cluster of eigenvalues of similar values. In every case, this was the second to last eigenvalue. In future, a more automatic way of selecting the smallest non-zero eigenvalue could be developed.

Stability Factor Interpolant

In order to evaluate the bound, quick evaluations for the residual and the stability factor for any point in parameter space must be found. Calculating the stability factor of the full-order system $\beta_h(\boldsymbol{\sigma})$ consists of solving a generalised eigenvalue problem involving the full-order stiffness matrix $\boldsymbol{A}(\boldsymbol{\sigma})$. Although the matrix is sparse (see Appendix A.2), it is still large in our case (containing millions of non-zero entries), and resulting in the calculation of $\beta_h(\boldsymbol{\sigma})$ becoming quite intensive and is therefore unaffordable in a real-time setting. To circumvent this, we use radial basis functions $\Phi(r) = e^{-r^2}$ to form an interpolant $\beta_I(\boldsymbol{\sigma})$ of the stability factor that can be calculated extremely quickly in an online phase, expressed as

$$\log(\beta_I(\boldsymbol{\sigma})) = \omega_0 + \boldsymbol{\omega}^T\boldsymbol{\sigma} + \sum_{j=1}^{n_I} \gamma_j \Phi(|\boldsymbol{\sigma} - \boldsymbol{\sigma}^j|) \tag{4.11}$$

where n_I are the number of interpolation points and ω_0, $\boldsymbol{\omega} = \{\omega_1, ..., \omega_P\}$ and γ_j are interpolation weights. Setting the interpolation points to be the high-fidelity solutions to β (i.e., $\log(\beta_I(\boldsymbol{\sigma}_j)) = \log(\beta_h(\boldsymbol{\sigma}_j))$ for $j = 1, .., n_I$), then given the additional conditions, $\sum_{j=1}^{n_I} \gamma_j = 0$ and $\sum_{j=1}^{n_I} \gamma_j \boldsymbol{\sigma}_p = 0$ for $p = 1, .., P$, the weights can be found by solving the following system of linear equations

$$\begin{pmatrix} \mathbb{M} & \mathbb{P}^T & \mathbf{1}^T \\ \mathbb{P} & 0 & 0 \\ \mathbf{1} & 0 & 0 \end{pmatrix} \begin{pmatrix} \boldsymbol{\gamma} \\ \boldsymbol{\omega} \\ \omega_0 \end{pmatrix} = \begin{pmatrix} \boldsymbol{\beta} \\ 0 \\ 0 \end{pmatrix}, \tag{4.12}$$

where $\mathbf{1} \in \mathbb{R}^{n_I}$ is a vector of ones, $\boldsymbol{\gamma} = \{\gamma_1, ..., \gamma_{n_I}\}$, $\boldsymbol{\beta} = \{\log(\beta_h(\boldsymbol{\sigma}_1)), ..., \log(\beta_h(\boldsymbol{\sigma}_{n_I}))\}$ and $(\mathbb{M})_{ij} = \Phi(|\boldsymbol{\sigma}^i - \boldsymbol{\sigma}^j|)$ and $(\mathbb{P})_{pj} = \boldsymbol{\sigma}_p^j$ for $i, j = 1, ..., n_I$, $p = 1, ..., P$. In an offline phase (outside of the greedy algorithm), $\beta_h(\boldsymbol{\sigma})$ for n_I points in $\mathscr{P}$ is calculated using eq. (4.10) and the interpolation weights are found with eq. (4.12). Then, in an online phase (within the greedy algorithm), $\beta_I(\boldsymbol{\sigma})$ can be found in real-time for any point in $\mathscr{P}$.

Computational Splitting of the Residual

It can be seen from eq. (4.6) that the residual depends matrix multiplications involving the full stiffness matrix $\boldsymbol{A}(\boldsymbol{\sigma})$. These matrix multiplications also benefit from being split for a significant speed-up, allowing the real-time calculation of the residual at any point in $\mathscr{P}$. The square of the L_2 norm of the residual can be expanded to

$$\begin{aligned} ||\boldsymbol{r}(\boldsymbol{\sigma})||_2^2 =& C - 2\sum_{p=1}^{P} \sigma_p \boldsymbol{u}_N(\boldsymbol{\sigma})^T \boldsymbol{d}_p \\ &+ \sum_{p_1,p_2=1}^{P} \sigma_{p_1}\sigma_{p_2} \boldsymbol{u}_N(\boldsymbol{\sigma})^T \mathbb{E}_{p_1,p_2} \boldsymbol{u}_N(\boldsymbol{\sigma}), \end{aligned} \tag{4.13}$$

where

$$C = \boldsymbol{b}^T \boldsymbol{b}, \tag{4.14a}$$

$$\boldsymbol{d}_p = \mathbb{V}^T {\boldsymbol{A}_p}^T \boldsymbol{b}, \tag{4.14b}$$

$$\mathbb{E}_{p_1,p_2} = \mathbb{V}^T {\boldsymbol{A}_{p_1}}^T \boldsymbol{A}_{p_2} \mathbb{V}. \tag{4.14c}$$

Fig. 4.2 shows that in the greedy algorithm, the new matrix $\mathbb{V}_N$ is constructed (second square) before the bound is calculated for a fine sample train (third square). Between these two processes, the eqs. (4.14) are solved, due to their independence from conductivity parameters. These values can then be stored and readily used in eq. (4.13). Practically, this results in an evaluation of the bound at each point in the entire sample train Ξ requiring only a handful of seconds on a single CPU core.

Proper Orthogonal Decomposition

Use of a greedy algorithm is not strictly necessary for the construction of a reduced basis space. The matrix $\mathbb{V}$ can also be generated using proper orthogonal decomposition (POD). This method uses SVD to construct a reduced basis space from a selection of pre-computed snapshots. Here, the snapshots form the matrix $\mathbb{S} = [\boldsymbol{u}(\boldsymbol{\sigma}^1), ..., \boldsymbol{u}(\boldsymbol{\sigma}^N)]$. SVD is then performed on $\mathbb{S}$ and the first $N_{POD} \leq N$ left singular vectors are chosen as $\mathbb{V}$.

This approach is more commonly known as a principle component analysis (PCA), which has been applied previously to imaging EIT [177]. Although simpler to implement, we chose not to use POD to construct the reduced basis space due to the intelligent sampling brought by the greedy algorithm. For POD, the selection of snapshots points in parameter space is not guided in anyway, relying on uniform or random sampling strategies. Using the greedy

algorithm, the parameter space is sampled very finely to first estimate the best point to select a new snapshot before repeating the process and iteratively adding snapshots. This results in the minimum number of snapshots (where a large system of equations needs be solved) being calculated for a predetermined threshold for error in the reduced solution.

4.4 Implementation and Verification

4.4.1 Set-up

We used a realistic head model discretised with 5M tetrahedral elements and 800k nodes. The model was based on the Colin27 atlas [13] and processed as in previous publications [115]. A cross section is shown in Fig. 4.3a depicting different tissue compartments, i.e., scalp, compact skull bone, spongiform bone, cerebrospinal fluid (CSF), grey matter (GM) and white matter (WM). The conductivities chosen for the synthetic measurements were uniform random samples within the interquartile ranges described in Table 4.1 for each of the tissues. The minimum, lower and upper quartiles and maximum values (excluding outliers) were chosen from the work carried out by McCann et al. (2019) [116]. A reduced model for each electrode pair used was trained for conductivity parameters within these ranges.

4.4.2 Technical Implementation

For each conductivity sample, the FP was solved for each of the 132 pairs of electrodes, where the injection and extraction electrode had 20 μA and -20 μA current applied, respectively. All pairs are composed of a unique injection electrode and a sink electrode that is common for all pairs placed on the scalp above the Sagittal suture (position Cz). This choice of electrode pairs allows the flexibility to simulate any electrode pair through a simple linear combination of the solutions of the trained pairs. Electrodes were positioned according to the ABC-128 standard layout (as used in BioSemi products) with the addition of fiducial

	Scalp	Compact bone	Spongiform bone	CSF	GM	WM
Min. (S/m)	0.136	0.0008	0.001	1.388	0.060	0.065
LQ (S/m)	0.303	0.002	0.013	1.450	0.268	0.092
UQ (S/m)	0.444	0.009	0.043	1.794	0.508	0.177
Max. (S/m)	0.620	0.0131	0.088	1.794	0.739	0.228

Table 4.1 Ranges of conductivities used for training. Minimum, lower quartile (LQ), upper quartile (UQ), and maximum (excluding outliers) reported by McCann et al. (2019).

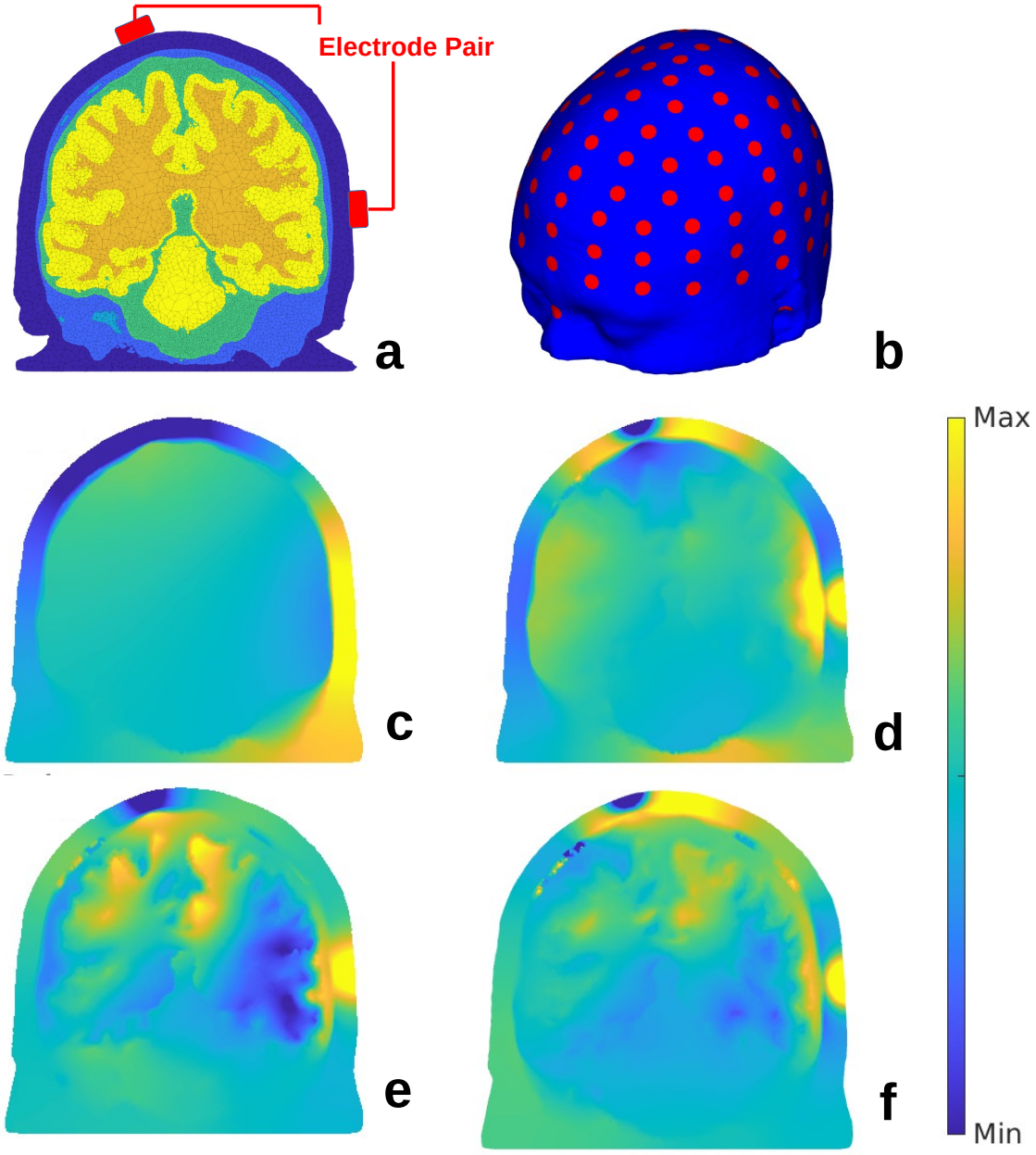

Fig. 4.3 **a**) Cross section of the FE mesh with compartments coloured separately. **b)** Electrodes (red circles) modelled on the surface of the scalp. **c-f)** Selection of the first basis vectors (ζ_2, ζ_4, ζ_7 and ζ_{11}, respectively) for the transformation matrix $\mathbb{V}$ made for an electrode pair plotted on the FE mesh. The colour indicates the value of the projected basis vector at each node that represents the additional information being encoded.

electrodes placed in the nasion, inion and left and right preauricular points and an electrode at the vertex (Cz), resulting in 133 sensors. This layout is partially displayed in Fig. 4.3b. An average common reference (AR) was applied to the potentials on the electrodes. The

133 electrodes were modelled as 1 cm diameter circles on the surface of the scalp with an effective contact impedance of 5 Ωm^2.

The systems of equations were solved with the Preconditioned Conjugate Gradient (PCG) solver with incomplete LU preconditioners [59]. They were solved with a tolerance of 10^{-10} and a maximum number of iterations of 6000. The FE method was implemented using first-order linear basis functions on the mesh nodes as used by Vauhkonen et al. (1999) [179]. Analytical expressions of the element matrices needed in eqs. (3.34a)-(3.34c) were utilised to avoid errors due to numerical quadrature [24].

The ROM method was trained using the same model, injection patterns and range of conductivities as above. We chose to train ROM for up to 100 snapshots to demonstrate the reduction in error in the FPs and IPs. However, as will become clear in the following chapter, there are a number of stopping criteria that can guide how many snapshots to take.

It should be noted that the matrix $\boldsymbol{A}_0$ in eq. (3.35) can be further affinely decomposed into a impedance ("z") independent matrix with a coefficient equal to z_l^{-1}, $l = 1, ..., L$. In this way, z_l can be trained as an additional set of parameters. However, we found that even across a large range of contact impedances, the effect on the FPs and IPs was negligible, as reported for EEG [135].

The reduced models generated for each electrode pair are completely independent, similarly to the IPs for the traditional method. Therefore, computational work was trivially parallelised by electrode pair on a cluster computer with 11 Intel(R) Xeon(R) X5660 CPU nodes at 2.80GHz. Each node had 12 cores and 16GB of memory per core.

4.4.3 ROM Performance Assessment

This assessment serves two main purposes. The first is to confirm that the pEIT-FP is meaningfully reducible in the sense that, for small N, $\boldsymbol{u}_a$ quickly converges to $\boldsymbol{u}$. The second is to validate the bound while simultaneously assessing its tightness. To achieve these aims, we plotted the average and maximum RE($\boldsymbol{\sigma}$) and $\Delta_{RE}(\boldsymbol{\sigma})$ as a function of N. The $\Delta_{RE}(\boldsymbol{\sigma})$ was calculated in the training phase during the greedy algorithm for a 6000 sample train across $\mathscr{P}$ for each electrode pair. The mean and maximum $\Delta_{RE}(\boldsymbol{\sigma})$ across the sample train were found for each electrode pair and then averaged across all electrode pairs. The RE($\boldsymbol{\sigma}$) was calculated for each electrode pair for 100 samples of $\mathscr{P}$. The average RE($\boldsymbol{\sigma}$) across all electrodes for each sample was found before plotting the average and maximum across $\mathscr{P}$. This was repeated for an increasing number of snapshots.

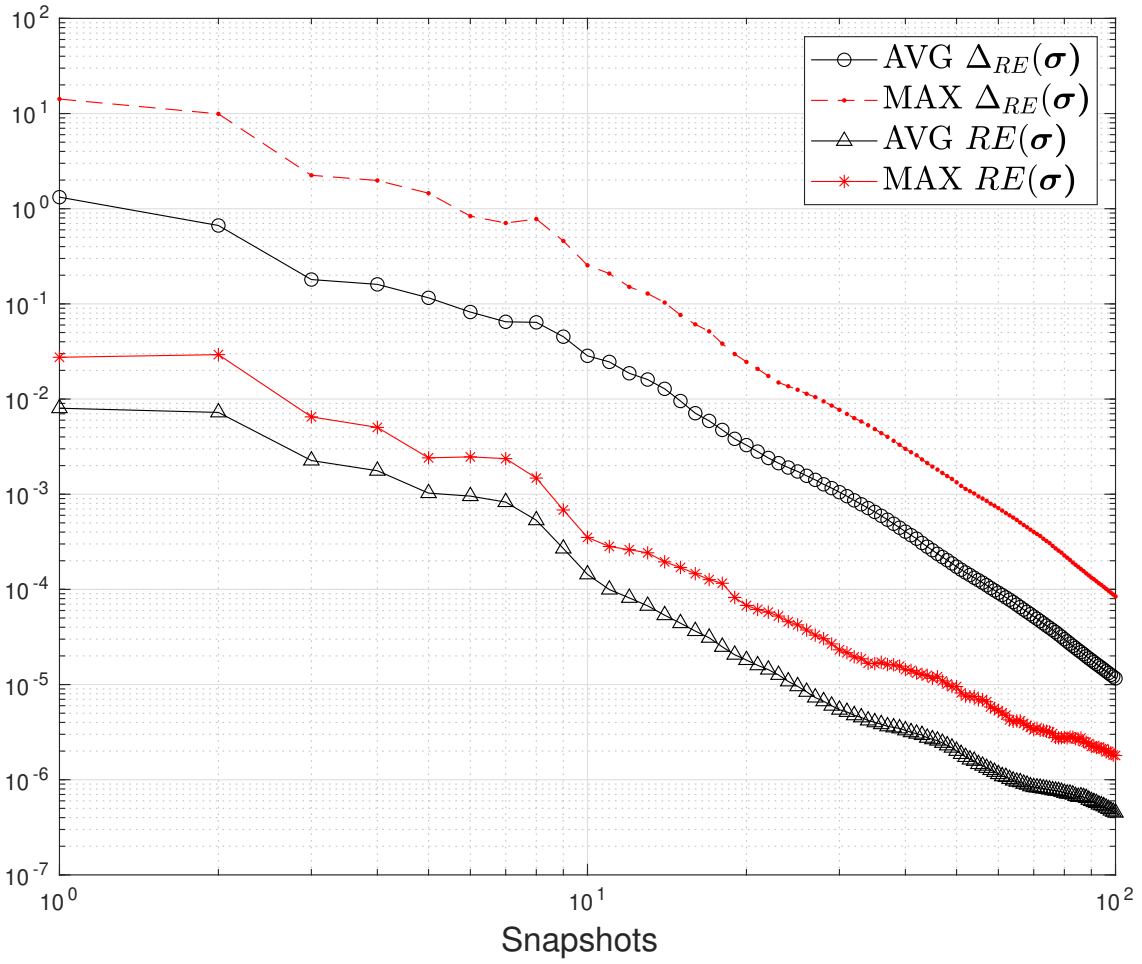

Fig. 4.4 Average and maximum $\Delta_{RE}(\sigma)$ and RE(σ) for a sample of parameters (averaged across electrodes) against the number of snapshots.

4.5 Results

Figs. 4.3b-d show a subset of the basis vectors (i.e., ζ_i for $i = 2, 4, 11$) that constitute the reduced basis space. Each additional function to the first is an orthogonal projection to the matrix $\mathbb{V}$ and encodes additional information into the reduced model. In particular, the basis vector ζ_{11} (Fig. 4.3f) shows that after the projection there is a significant difference in electrical potential solution in the brain between the previous sample conductivities and those for the snapshot. Once added, this results in a reduced model with specific information about the response of the electrical potential in the brain to conductivity changes in the model. This demonstrates the greedy algorithm in action. The same effect can be seen with the

spongiform bone with respect to the bright spots in the skull in basis vector $\boldsymbol{\zeta}_4$ (Fig. 4.3d) and $\boldsymbol{\zeta}_{11}$.

Fig. 4.4 shows the average and maximum $\Delta_{RE}(\boldsymbol{\sigma})$ and $\mathrm{RE}(\boldsymbol{\sigma})$ as a function of snapshots. The $\Delta_{RE}(\boldsymbol{\sigma})$ was calculated across the sample set Ξ and the $\mathrm{RE}(\boldsymbol{\sigma})$ was found for 100 conductivity samples. It is interesting to note that the bound becomes slightly sharper as the number of snapshots increases. Fig. 4.4 also demonstrates that $\Delta_{RE}(\boldsymbol{\sigma})$ can be used as a stopping criteria for the number of snapshots used to train the model. When set, the greedy algorithm will stop when $\Delta_{RE}(\boldsymbol{\sigma})$ for every point in the fine sample is below the threshold stated. Using this stopping criteria ensures that the $\mathrm{RE}(\boldsymbol{\sigma})$ in the FP is below the threshold. However, choosing a threshold is not trivial (see Section 5.6) and there is a risk of unnecessary training of the model.

4.6 Further Notes

A time penalty incurred by ROM is the computational cost associated with training the stability factor interpolant during the offline phase, requiring multiple solutions to a generalised eigenvalue problem. This process takes approximately 15-30 minutes per problem (for an Intel Xeon CPU at 2.8 GHz for our model) and can be parallelised on a cluster. The interpolant generated is source vector independent, and therefore can be used for all electrode pairs. Although small in comparison to the training for ROM and the traditional method, this should still be considered as part of the offline training process. There exists some techniques that minimise the computational load of this stage such as greedy algorithms to reduce the number of interpolation points needed [112]. Exploring these optimisations of the framework will be work for the future. Further, we've found that interpolating between these points in a 6-dimensional space is a non-trivial task due to the complexity of the resulting manifold and the possible noise in the interpolation data. We found that the use of too many randomly selected interpolation points led to over-fitting and consequently a poor interpolation. The more conservative strategies suggested by Manzoni et al. (2015) [112] may help tackle this class of problem and this shall be explored in future work.

In this framework, we use the L2-norm in both the $\Delta_{RE}(\boldsymbol{\sigma})$ and the projection due to its ease of implementation. However, an equally valid $\Delta_{RE}(\boldsymbol{\sigma})$ can also be calculated using the norm of the space containing the solution [139]. The solution to the variational formulation of the problem can be found in an appropriate quotient Hilbert space, equipped with a norm that can be used for this task [162]. Modifying our framework to utilise this norm may improve the sharpness of the bound. One artefact of the training noticed was the loss of orthogonality in the transformation matrix after approximately 150 snapshots. This could be

due to numerical errors introduced into the Gram-Schmidt orthonormalisation. We use the classical Gram-Schmidt process in this work, however, a well known and more numerically stable method called the modified Gram-Schmidt method could also be used [32]. Other numerically stable implementations of the Gram-Schmidt process have been developed and these may be explored in the future [38].

An additional substantial speed-up was achieved in the greedy algorithm by utilising the reduced model at each iteration to provide an initial guess for the PCG method when solving for a snapshot. As snapshots are added to the reduced model, the initial guess improves which leads to faster PCG solutions. Practically, this means that the time taken for one snapshot is halved after approximately 40 snapshots.

Fig. 4.4 shows that the pEIT-FP is highly reducible, demonstrated by the rapid reduction in relative error. This impressive performance could be explained by the solution manifold being relatively smooth across the chosen parameter space meaning fewer snapshots are required to adequately characterise it. The presence of a smooth solution manifold has been shown in other work (e.g., Turovets et al. (2008) [169]) for single tissue conductivities where the manifold took the form of a “shallow valley". If this behavior extends to a 6-dimensional parameter space, this could explain the reducibility of the problem. Please see Chapter 6 for further discussion on this topic.

4.7 Summary

This chapter has introduced reduced order modelling (ROM) and covered the basic implementation of ROM applied to the pEIT-FP. The basic theory for ROM was laid out, including the mathematically rigorous bound, and the training of the reduced model, before its implementation in a realistic head model. The reducibility of the problem was confirmed by assessing the accuracy of the reduced solutions against the solutions to the full systems of equations, while simultaneously verifying the error bound. This chapter shows most importantly that a reduced model of the pEIT-FP is a suitable replacement for the full-order system, meaning it can be used in the pEIT-IP.The main points of the chapter are as follows:

- ROM is a dimensionality reduction technique where a relatively low-dimensional model mapping changes in parameter space to changes in the solution of a system of equations is built. This reduced model is constructed with a number of solutions to the parameter-dependent system of equations with a specific set of these parameters (called snapshots). In the case of the system of equations being large and problem being sufficiently reducible, the resulting model is significantly lower in dimensionality than the system of equations.

- The property of affine decomposition is required for any system to be suitable for ROM. Therefore ROM can be applied to the pEIT-FP to obtain a reduced model that can evaluate a sufficiently accurate approximate solution for any point in the parameter/conductivity space $\mathscr{P}$.
- We implemented ROM with pEIT for a realistic head model with 800k nodes and six head tissues by constructing a reduced pEIT-FP model for each electrode injection pair considered in the pEIT protocol. The models were trained within a parameter space defined by the variability in individual tissues found in the literature.
- The selection of the snapshots used to build the reduced model is guided by a rigorous error bound, that serves as an estimate of the error between the approximate solution and the full-order solution across the parameter space. For the specific case of pEIT, this error bound is verified in this chapter.
- The accuracy of the approximate solutions found using the reduced model is assessed as a function of the snapshots required to build the models. It is shown that with only 30 snapshots to build the model, the average relative error is below 10^{-5} across $\mathscr{P}$ and for all injection pairs.

Chapter 5

Reduced Order Modelling for parametric Electrical Impedance Tomography: Implementation and Applications

5.1 Overview and Commentary

So far, the computational cost of the pEIT-FP and a solution for reducing this cost using ROM have been suggested. In this chapter, the original motivation for pEIT is revisited by utilising the newly trained ROM-pEIT-FP in the pEIT-IP. The metrics of conductivity estimation accuracy and computational cost are used to compare and contrast ROM-pEIT and the current state-of-the-art approach. A brief primer on the use of a gradient-assisted method in pEIT is given before its comparison with ROM-pEIT using synthetic and real data. We find a significant improvement in speed, leading to a practical improvement in the estimation accuracy. After this verification, additional use cases are explored that this new framework now allows, including the estimation of previously unreachable tissues and anisotropic tissues, estimation depending on reference electrode placement and using new pEIT protocols.

This chapter has been adapted and extended from a publication provisionally accepted by the Journal of Neural Engineering: Matthew R. Walker, Mariano Fernández-Corazza, Sergei Turovets and Leandro Beltrachini, Electrical Impedance Tomography Meets Reduced Order Modelling: a Framework for Faster and More Reliable Conductivity Estimations. Leandro Beltrachini contributed to the conceptualisation and programming of the work. Mariano Fernández-Corazza and Sergei Turovets collected the real data used in this chapter. All other work is that of the author of this thesis. Similarly to the last chapter, further details, beyond

those included in the publication, have been added to this chapter and more exploratory analysis provided.

5.2 Introduction

With the ROM-pEIT-FP trained and verified to be a suitable replacement for the full-order pEIT-FP, we can now perform the pEIT-IP where the FPs are generated in real-time. The resulting IP is therefore orders of magnitude faster than the original full-order version. This speedup in the IP yields many benefits, which are explored in detail this chapter. This work is placed in the context of the literature by comparison with the state-of-the-art technique. The current best effort to address computational load of the IP is to reduce the number of solutions required for the pEIT-IP to converge by utilising a gradient assisted optimisation method [61]. This approach has proven successful for estimating scalp and skull conductivities from *in vivo* and synthetic measurements to a good level of accuracy [63, 60]. However, this method requires the additional calculation of a gradient in each iteration, which itself is computationally costly. Furthermore, estimating the conductivity of some tissues proves challenging. For example, the conductivity of the spongiform bone inside the skull has been estimated with a coefficient of variation as large as one [63].

This chapter compares the current state-of-the-art and ROM-pEIT in both synthetic and real data. With the synthetic data, we are able to simulate a range of possible scenarios, to thoroughly test the feasibility of ROM-pEIT, and highlight its advantages. The use of real data allows the validation of ROM-pEIT in a real world setting. Throughout, we show that this new ROM-pEIT framework yields significant improvements in the speed of the estimation of all tissues in the head, assimilating the new capability to confidently estimate conductivities previously unreachable with traditional approaches.

5.3 Experiments with Synthetic Data

5.3.1 Setup

To generate synthetic pEIT signal data, the full-order FP for each injection pair is solved for a range of conductivity sets $\boldsymbol{\sigma}$, where the injection pairs are the same used to train the ROMs in the previous chapter. Gaussian noise was then added to the measurements that had a standard deviation of 0.82 μV, which is similar to the noise found in real measurements [63].

Similarly to other work [63], we have removed some erroneous estimations from injection patterns where the IP has either not converged or has given an unrealistic conductivity (e.g.,

negative conductivities), which may occur for the traditional method only as it is based on an unconstrained optimisation technique.

5.3.2 Experiment 1 - IP Performance

To assess how useful the ROM-pEIT framework is, we considered two important metrics in pEIT: the accuracy of the estimations from the inverse problem and the computational cost required to achieve them. To that end, we compared our results with the best approach currently in the field, which provides reliable estimations for scalp and compact skull electrical conductivities [63]. This method minimises eq. (3.53) using the gradient-assisted quasi-Newton method. However, this requires the calculation of the gradient of the solution for each FP, for each of the parameters being searched for [55, 63]. The gradient can be found using [63]

$$\frac{\partial \mathbf{A}^{-1}(\boldsymbol{\sigma})\mathbf{b}}{\partial \sigma_p} = -\mathbf{A}^{-1}(\boldsymbol{\sigma})\mathbf{A}_p\boldsymbol{u}. \tag{5.1}$$

From eq. (5.1), it is clear that finding each of the gradients requires solving another large system of equations similar to the FP. This results in a significant overhead in terms of computational cost, especially when multiple parameters are being estimated simultaneously. Inserting this into the loop in Fig. 3.7 shows that, for each iteration in the optimisation, the number of large systems of equations to solve is equal to the FP plus the number of tissues being estimated. Henceforth, we shall refer to this method of gradient assisted optimisation using the full-order FP as the traditional method.

A further consequence of using the reduced system of eqs. (4.5) is that the derivative (5.1) can no longer be calculated and therefore neither can the quasi-Newton method be utilised efficiently. However, using quasi-Newton methods to reduce the computational cost is no longer of concern, and we are free to explore other methods, such as the interior-point optimisation approach. Although this method requires more loops and therefore more systems to solve than the quasi-Newton algorithm, the cost of the new optimisation is still negligible compared to the traditional technique.

Therefore, we have chosen to compare the computational cost of the ROM-pEIT framework and the traditional method by using the number of $(n+L)\times(n+L)$ linear systems of equations needed to be solved for each electrode pair. For ROM, all of these systems are solved in the offline phase. Given that these systems embody the bulk of the computational work, it is an appropriate metric for comparison. Making the comparison independent of the electrode pairs means that the savings are the same irrespective of the injection protocols used.

For the traditional method, the IP was run as a 3-parameter search, optimising for the scalp, compact skull and spongiform bone simultaneously. For the conductivities not being optimised (CSF, GM, WM), they were fixed to the ground truth values used to make the synthetic measurements. We chose this format to isolate and assess the estimation of the three conductivities stated only. To assess the improvement in the IP, we redefined the relative error (RE) as

$$RE = |\hat{\sigma} - \sigma|/\sigma, \tag{5.2}$$

where $\hat{\sigma}$ and σ are the estimated and the ground truth scalar conductivities, respectively. The estimation progress was logged at each iteration and plotted as the RE between the estimation and the sample parameters. The ROM IP was run as a 6-parameter search to estimate all of the compartments in the model. All optimisations were started from the centre point of the ranges specified in Table 4.1.

The mean of the RE in the estimation for each tissue for each number of iterations (and function evaluations within those iterations) was calculated, and then averaged across 10 randomly selected conductivity samples from a uniform distribution. We used 10 samples due to the computational cost of the traditional method. The IP with ROM was then run for a further 90 samples of $\mathscr{P}$ and plotted separately with the average RE across the samples and electrodes displayed for all tissues.

To further assess the estimations, we repeated the ROM-pEIT IP with the reduced model containing 30 snapshots for various signal-to-noise ratios by increasing the standard deviation in the additive Gaussian noise. The RE in each tissue was averaged across all electrode pairs and samples.

5.3.3 Experiment 2 - Anisotropy

It has been shown that the inclusion of the spongiform bone in head models reduces the error in the EEG-FP and IP [115]. However, in the event of missing spongiform information, the skull may be modelled as a single compartment with anisotropic conductivity [60, 49]. Therefore, a separate experiment aimed to demonstrate the adaptation of ROM-pEIT to model a homogeneous and anisotropic skull conductivity.

Firstly, we modified the realistic head model by merging the compact and spongiform bone to create one homogeneous skull compartment. We then trained another ROM model with the new head model where the conductivity tensor field for the skull compartment has been transformed from a Cartesian basis to a radial and tangential basis relative to the centre point of the brain. The range of values used for both radial and tangential conductivities were

from the minimum compact skull (0.002 S/m) to the maximum spongiform skull (0.043 S/m) used in the previous experiments. This was to accommodate for a wide range of possible skull compositions, from entirely compact skull to significant proportions of spongiform bone.

We analysed the sensitivity of the ROM-pEIT framework to anisotropic conductivities in the skull by assessing the RE in each compartment. To achieve this, we created 100 synthetic measurements using the full-order model with noise. The model was adapted by merging the compact and spongiform skull and given an anisotropic conductivity in the same range used for ROM. These measurements were then used to run the IP with a new reduced model, trained with radial and tangential conductivities in the whole skull. We plotted the RE in the estimation for each tissue compartment to assess the sensitivity of the reduced basis IP to the radial and tangential components of the skull conductivity. As before, the IP was run as a 6-parameter estimation, this time estimating the radial and tangential values, replacing the compact and spongiform skull conductivities.

To create an anisotropic model we first defined a conductivity tensor with a basis that is radial and tangential with respect to the surface of the scalp as

$$\boldsymbol{\sigma} = \begin{pmatrix} \sigma^t & 0 & 0 \\ 0 & \sigma^t & 0 \\ 0 & 0 & \sigma^r \end{pmatrix}, \tag{5.3}$$

where σ^t is the tangential component and σ^r is the radial component of the conductivity. To use this for the construction of the stiffness matrix, this tensor has to be transformed back to a Cartesian basis using two rotations described by the matrix

$$C = \begin{pmatrix} cos(\theta)cos(\phi) & -sin(\theta) & cos(\theta)sin(\phi) \\ sin(\theta)cos(\phi) & cos(\theta) & sin(\theta)sin(\phi) \\ -sin(\phi) & 0 & cos(\phi) \end{pmatrix}, \tag{5.4}$$

where C is a change of basis matrix, and θ and ϕ are angles of rotation which are specific to each element and calculated using the difference between a vector from the element and the closest triangle on the mesh surface to that element and the Cartesian basis. The tensor is transformed by

$$\boldsymbol{\sigma}_{cart} = C\boldsymbol{\sigma}C^T. \tag{5.5}$$

5.3.4 Experiment 3 - Response to Reference Choice

A common reference electrode is standard in EEG setups to ensure unbiased readings between amplifiers. This electrode is most often fixed in place at the vertex (electrode Cz). However, it has been suggested that a more flexible reference could yield fewer artifacts in EEG data [86]. Although choosing a reference for the potential measurements has been investigated thoroughly through the lens of “re-referencing" techniques in EEG, to our knowledge, no such analysis has been performed for pEIT. Furthermore, although re-referencing allows the use of average reference (AR) and the reference electrode standardisation technique (REST), these methods still encode the information of the originally referenced potentials and, as such, are impacted heavily by the use of realistic head models [39, 109, 200]. In this context we used ROM-pEIT to investigate the impact of the original choice of reference electrode in a situation of missing spongiform bone information.

Firstly, we trained a reduced model with the compact and spongiform bone merged into a single whole skull compartment. The conductivity ranges used in training for each tissue were the interquartile ranges in Table 4.1 where the whole skull compartment was trained between the lower quartile for compact bone and upper quartile for spongiform bone. We created a current injection protocol comprising 106 injection-extraction electrode pairs with a single common reference. These pairs included a set of 106 unique injection electrodes, where the extraction electrodes were selected to be the opposite side of the head (with electrodes repeating no more than twice). This strategy was chosen to obtain maximum coverage of the head and probe deep tissues [60]. We repeated the protocol sequentially changing the reference to every electrode position (and omitting pairs involving such an electrode). This resulted in 133 sets of synthetic measurements with a unique reference electrode in each set. Next, we ran the IP for each electrode pair in the protocol in all sets, totalling over 14,000 IPs.

To assess the effect of the reference selection on the estimations, we monitored the standard deviation in the IP skull estimations in each set and then plotted this value on the reference electrode of that set, before interpolating across the skull. We then reported the estimations and standard deviations for the reference electrode that has the most variability.

5.3.5 Experiment 4 - Staged Optimisation

During the inverse problem, the interior-point optimisation explores the 6-dimensional parameter space, searching for the global minima. However, it is unclear how complex the solution manifold in this many dimensions is, and therefore how many local minima the optimisation could be caught in. In this experiment, we utilise a custom pEIT protocol to

extract more accurate conductivity estimations with the aim of simplifying the solution space to search. To do this, we adapt the protocol in two ways that are now possible thanks to ROM. The first is the use of a staged optimisation process, eliminating the scalp and compact skull from the final optimisation step and therefore reducing the parameter space. The second is combining the inverse problems of each injection pattern into a single simultaneous optimisation, utilising the measurements from all patterns at once.

Up to this point we have considered injection patterns that contain one injection electrode and one sink electrode, separated by a considerable distance for the majority of patterns. In the real data case, the injection and sink electrodes were opposite sides of the head to the probe deeper tissues (e.g. grey matter and white matter). For injection and sink electrodes that are close together (i.e. adjacent), it can be shown that the sensitivity of a pattern to deeper tissues is reduced due to most of the current being shunted through the scalp [64, 2]. However, we propose using this shunting to our advantage, by performing two sets of measurements. The first utilises 20 adjacent patterns, where the injection electrode is kept constant and the 20 patterns are chosen where the sink electrode is adjacent or close to the injection electrode. The injection electrode in this case was chosen to be one approximately half way between the vertex electrode Cz and the left-side preauricular point. The second set was the same used for the synthetic data previously (i.e., 132 injection pairs with a common sink electrode). All pattern measurements were referenced using AR. The staged optimisation can be broken down into the following steps:

1. Estimate the scalp conductivity using the adjacent injection patterns. Fix this conductivity for the following optimisations.

2. Estimate the compact skull conductivity using the second set of patterns (i.e. the same as previous experiments). Fix this conductivity for final optimisation. The initial guess was the result of the previous estimation.

3. Estimate the remaining tissue conductivities all together with the second set of injection patterns. The initial guess was the result of the previous estimation.

This process was repeated for 50 random conductivity samples and for up to 50 snapshots used to build the reduced model, where the data was generated synthetically. For each snapshot number, the average relative error in the estimations was plotted for each tissue.

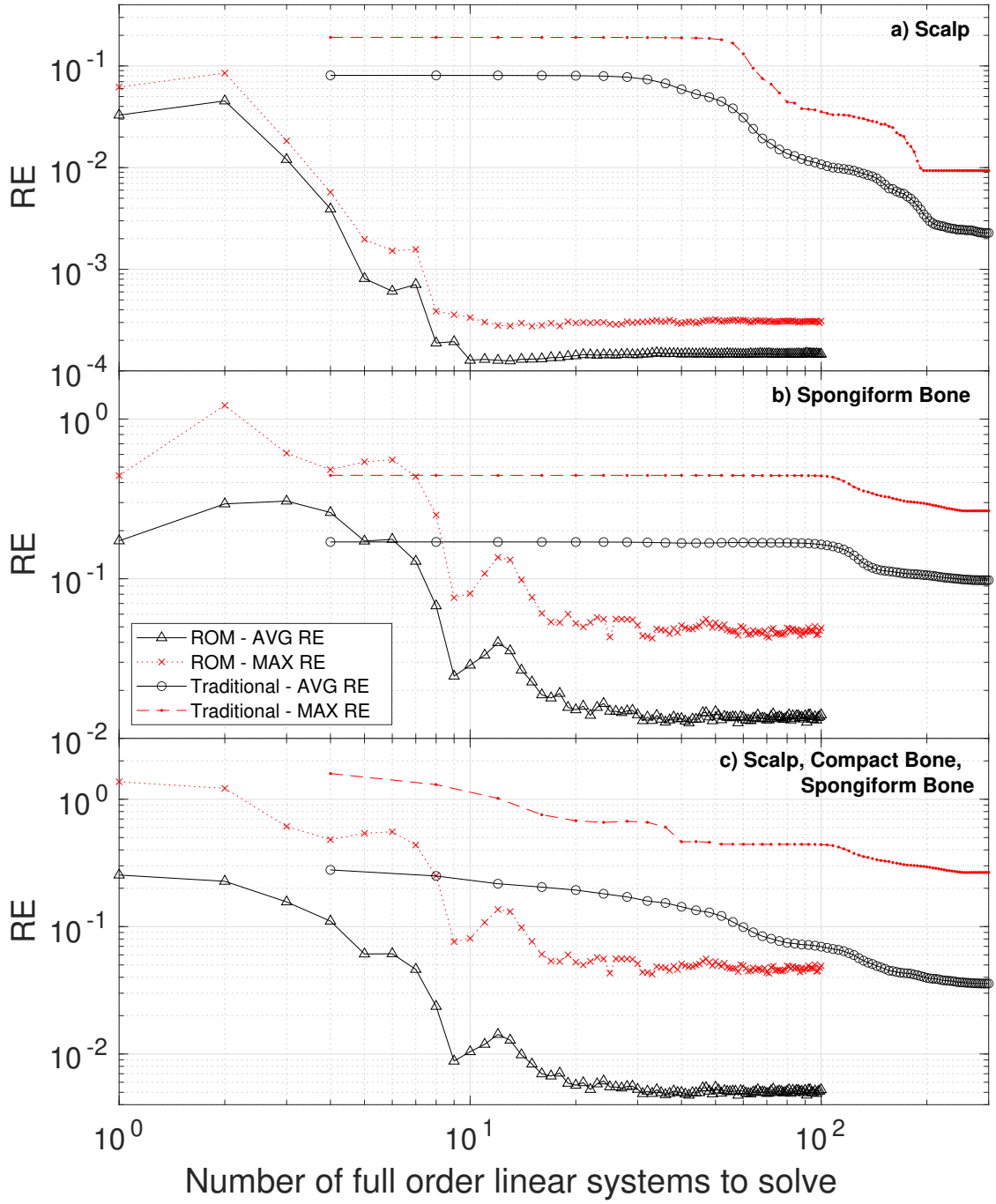

Fig. 5.1 Average (black lines) and maximum (red lines) of the RE in the estimation of the conductivities across multiple electrode pairs and for 10 sets of synthetic measurements with uniformly distributed conductivity samples. The red and black dotted lines in each figure correspond to the traditional method and the red and black full lines with crosses and triangles respectively are for ROM.

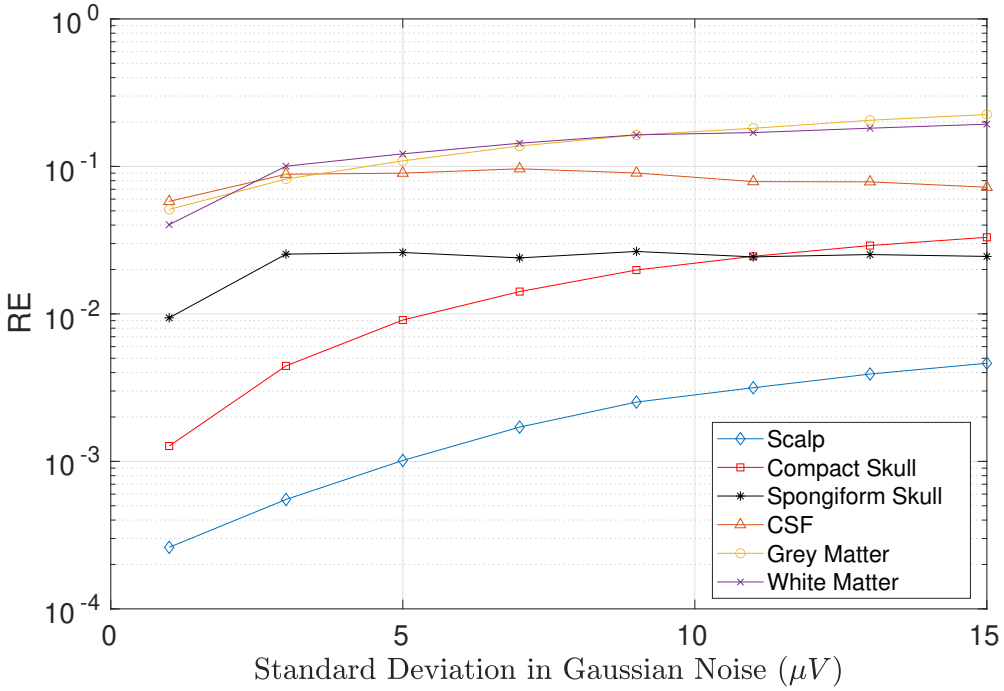

Fig. 5.2 RE in the conductivity estimations for each tissue as a function of the standard deviation of the Gaussian noise added to the measurements used in the IP.

5.4 Results with Synthetic Data

5.4.1 Experiment 1 - IP Performance

Displayed in Fig. 5.1 is the average and maximum RE in the conductivity estimations for ROM and the traditional method across 10 samples and all electrode pairs. It can be seen that there are improvements in computational cost and accuracy of the ROM-pEIT framework compared to the traditional method. This is shown for the first three compartments of the head model (scalp, compact skull and spongiform bone) and the scalp and spongiform bone separately. Focusing on the three compartment graph (Fig. 5.1c), we can see that the RE in the IP estimation averaged across compartments, injection patterns, samples of parameter space improves by nearly an order of magnitude, with the number of linear systems to solve reducing by an order of magnitude too. The maximum error for any injection pair for any sample is displayed in red crosses and also demonstrates an improvement over the average of the traditional method.

The number of injection pairs removed from the traditional estimations due to erroneous results was approximately 30 for two of the samples and none for the rest. All injection pairs were preserved for the ROM-pEIT IPs.

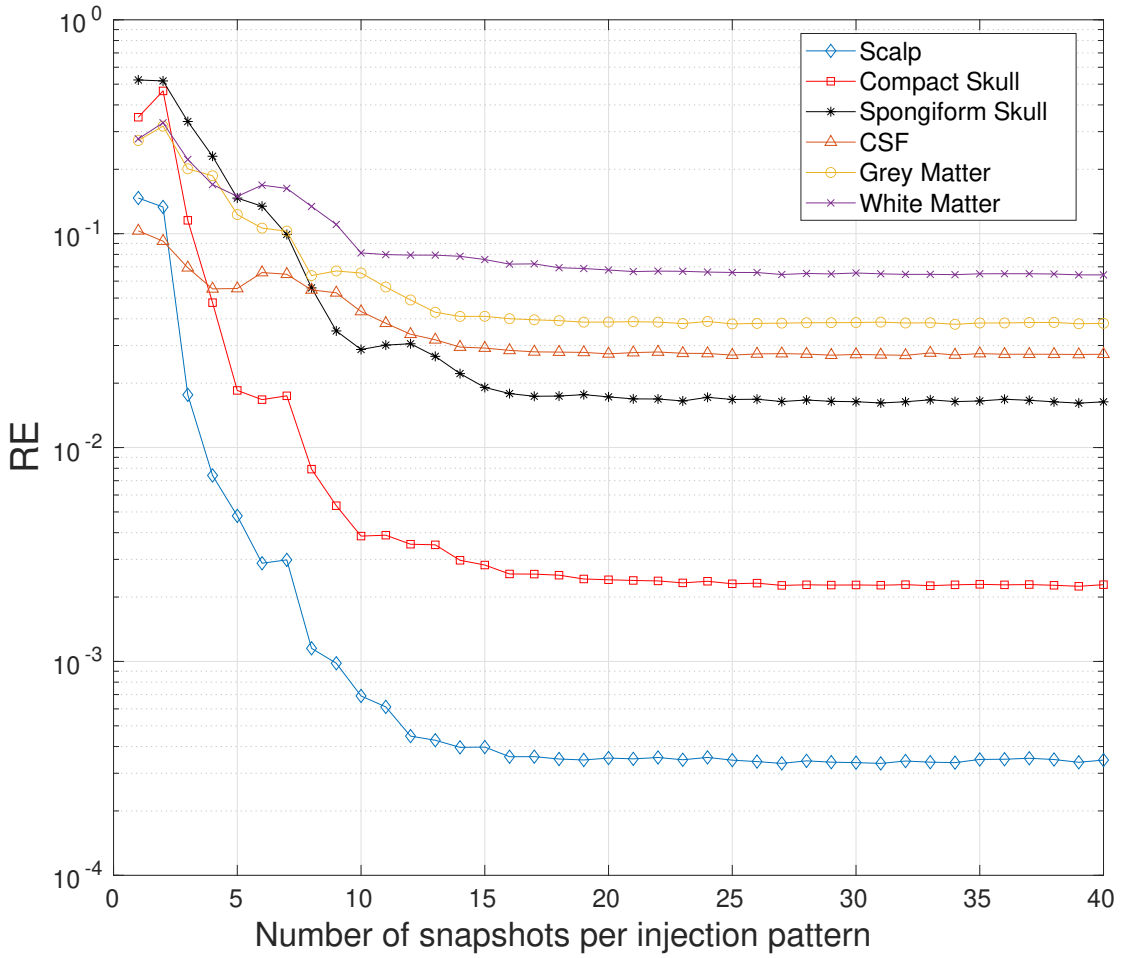

Fig. 5.3 RE for each individual compartment as a function of snapshots across 100 samples and 132 injection pairs using the ROM-pEIT method.

It is useful to separate all of the conductivities to see which are contributing the most to the REs seen in Fig. 5.1c. The RE for the scalp is shown in Fig. 5.1a, where the improvement in accuracy and computational effort due to the ROM-pEIT framework is most apparent with a reduction in systems to solve from 250 to 10 maintaining an order of magnitude improvement in RE. In Fig. 5.1b, we see that the traditional method cannot obtain a reliable estimate for the spongiform bone with the optimisation implementation used. However, the ROM-pEIT framework is able to estimate the conductivity of the spongiform bone down to an average RE of almost 1% and a maximum RE of 5%.

As previously mentioned, the benefits of using ROM become most clear during a 6-parameter search where the IP can optimise for all compartments in the model. Fig. 5.3 shows the average RE for ROM but for all tissue compartments, as a function of the number of snapshots used in the estimation. The figure shows us that with ROM and the optimisations

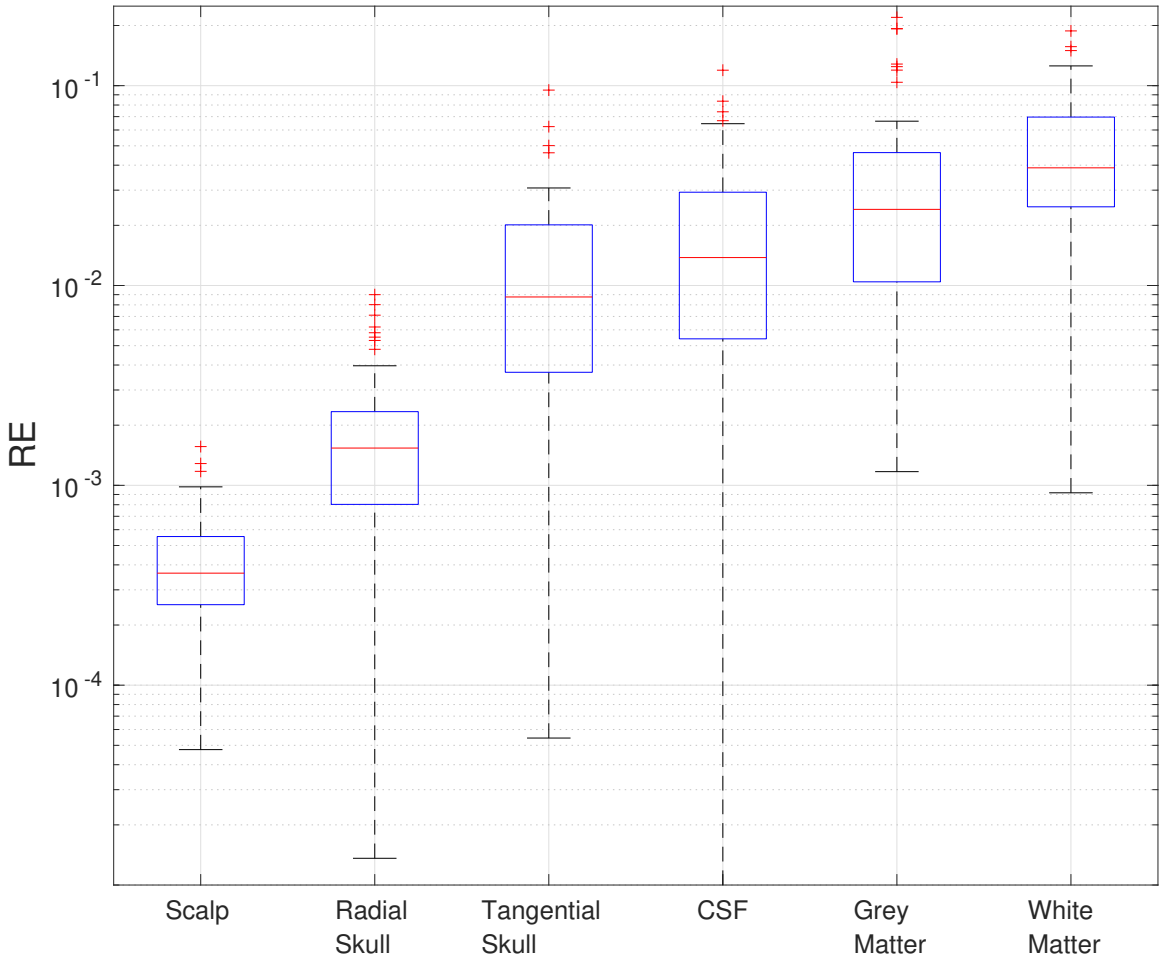

Fig. 5.4 Sensitivity Analysis across 100 samples for the reduced basis anisotropic model. The estimations are for the full 6-parameter space using 30 snapshots for each electrode pair. Each box plot shows the estimation error in a single tissue that is labelled.

it allows, the IP is able to estimate CSF, GM and WM in the brain to approximately a 3%, 4%, 7% RE, respectively. It is also worth noting that the coefficient of variation in the electrode estimations was between 0.001 and 0.1 for all tissues after 30 snapshots.

From Figs. 5.1 and 5.3 it is clear that the accuracy of the IP with ROM stops improving after 30 snapshots. Therefore, we chose to only train the anisotropic reduced model in Experiment 3 up to this number to perform the sensitivity analysis.

Each traditional method function evaluation required approximately 250 s for each PCG followed by 1200 s for the full gradient calculation (consisting of 3 additional PCGs and 3 large matrix calculations). Each PCG in a greedy algorithm took a similar time as the traditional method plus 10 seconds for the overhead of calculating the bound and orthonormalising the solution to the transformation matrix.

	Scalp	Skull	CSF	GM	WM
True	369	(5.9/38)	1626	421	134
Est.	362 ± 22	8.7 ± 1.2	1602 ± 157	325 ± 98	101 ± 25

Table 5.1 Ground truth and estimated conductivities in the situation of a missing spongiform bone compartment. Units in mS/m.

An additional substantial speed-up was achieved in the greedy algorithm by utilising the reduced model at the previous iteration to provide an initial guess for the PCG method when solving for a snapshot. As snapshots are added to the reduced model, the initial guess improves, leading to faster PCG solutions. Practically, this means that the time taken for one snapshot is halved after approximately 40 snapshots.

Times varied substantially due to innate variability in compute nodes, even of the same species and differences in convergence speeds. However, we found that the traditional method took, on average, 30-40 hours to converge using 75 function evaluations while trivially parallelised on a cluster. Conversely, the greedy algorithm used to train the reduced model took only 1.5 hours to reach 40 snapshots. The resulting 132 ROM-pEIT IPs (one for each pair) took approximately 20 seconds to complete in series on a single compute node.

Fig. 5.2 shows the response of the IP estimations for each tissue to varying intensities of noise, while utilising the interior-point optimisation and ROM-pEIT FPs. As expected, the RE in most tissues increase as noise increases. Of particular interest, is the RE in the spongiform bone, which remains stable under noise that is 1.5 orders of magnitude greater than the noise obtained from real measurements [63].

5.4.2 Experiment 2 - Anisotropy

The results of the sensitivity analysis described in Section 5.3.3 are displayed in Fig. 5.4. From this analysis we can see that the framework presented is sensitive to the tangential and radial conductivity components of the skull while remaining sensitive to the inner compartments.

5.4.3 Experiment 3 - Response to Reference Choice

Fig. 5.5a displays the ratio of spongiform bone to compact bone in the skull from 0 to 1. This shows the distribution of the spongiform bone within the skull. Plotted across the skull in Fig. 5.5b are the standard deviations in the estimations for the skull compartment across electrode pairs as a function of the reference electrode used. In other words, the colour at each point on the skull represents the variability in 106 IP skull estimations if the reference

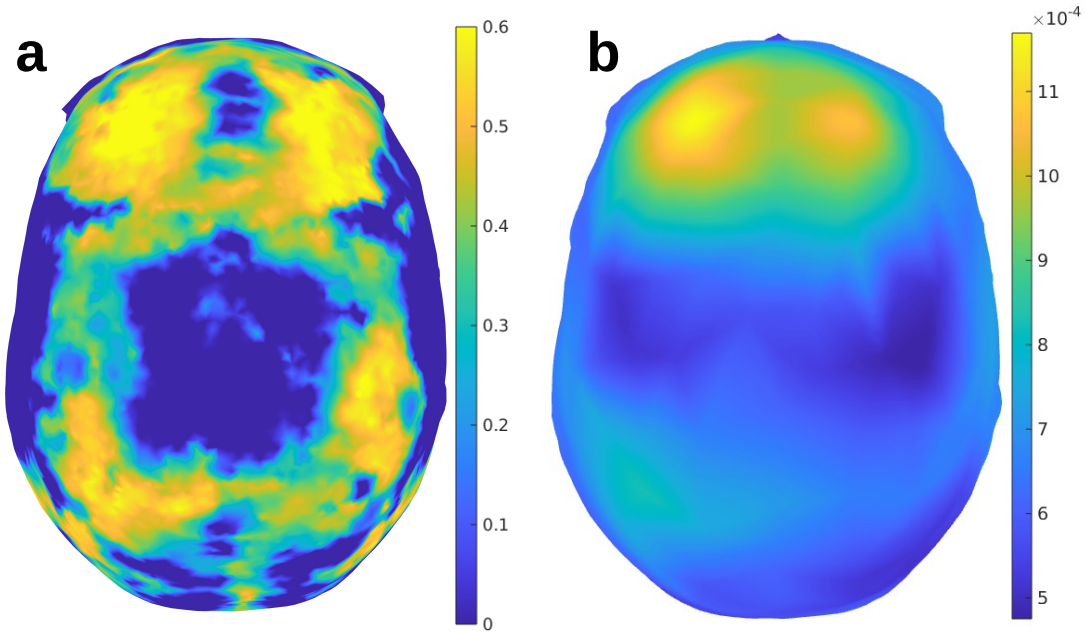

Fig. 5.5 **a)** Ratio of spongiform bone to compact bone that makes up a given point in the skull. **b)** Standard deviation (S/m) in the skull estimations in all electrode pairs plotted as a function of the reference electrode used and then interpolated over the skull.

electrode were placed over that point. Note that the bright yellow areas clearly correlate with the spongiform bone information that is missing, indicating that when the reference electrode is close to a modelling inaccuracy, the estimations become less stable. The generation of Fig. 5.5b required over 14,000 IPs and at least 10 million FPs, needing only 30 minutes to complete on a single PC (Intel(R) Core(TM) i5-6500 CPU at 3.20GHz). Within reason, this analysis could not be possible without ROM-pEIT.

Table 5.1 contains the ground truth conductivities for the synthetic measurements and the estimated conductivities with standard deviations for all pairs when considering the reference electrode corresponding to the bright yellow spot in Fig. 5.5. Note that the standard deviation is high in all compartments, as well as the skull, demonstrating the impact of incorrect skull modelling on the conductivity estimations.

5.4.4 Experiment 4 - Staged Optimisation

Fig. 5.6 displays the average conductivity estimation for each number of snapshots in the reduced model across 50 random conductivity samples. Through a comparison with Fig. 5.3, there is clearly a substantial improvement of almost one order of magnitude in spongiform bone estimation, with mild improvements in scalp and white matter conductivities. The effect

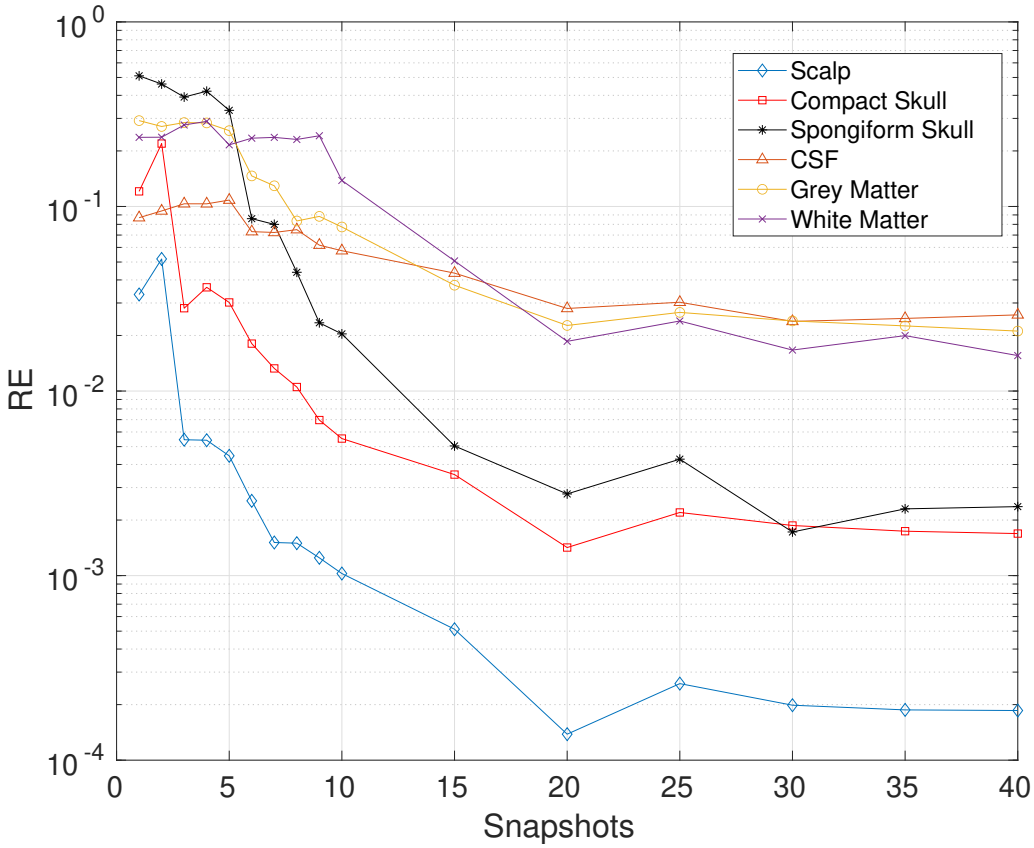

Fig. 5.6 Average RE in each tissue for 50 conductivity samples when estimated using the staged ROM-pEIT protocol.

on the spongiform bone estimation accuracy was only noticed when using the combination of simultaneous pattern estimation and staged optimisation. Furthermore, the affect on the spongiform bone estimation was far less profound when steps 2 and 3 were merged into one estimation. It is unclear why this was the case.

We set the maximum number of function counts per optimisation to 3000, however, we found no improvement when increasing this number. This was especially true for each estimation after the first, given the initial guess improves with each stage.

5.5 Validation with Real Data

We use real pEIT data from 44, 46 and 52 year old male subjects labelled AM (Atlas Man), CA (Caucasian Atlas) and AA (Asian Atlas), respectively. The head tissues for these subjects were segmented from a T1-weighted MRI co-registered with a CT scan and the FEM models

were generated with the *iso2mesh* package [138]. The data was acquired using a 128 sensor net from EGI (Electrical Geodesics, Inc.) with one reference electrode (Cz) where 62 unique injection patterns were applied using a current of ±20 μA at a frequency of 27 Hz. Further details on the image processing and data acquisition are described in Fernández-Corazza et al. (2018) [63]. The data was cleaned by removing measurements from 3 bad channels and removing patterns whose data was also noisy. This resulted in 36, 47 and 42 patterns with usable data, respectively, each with one injection, one extraction and 123 measurement electrodes. The injection and extraction electrodes were approximately diametrically opposite sides of the head.

All research protocols involving human subjects complied with the ethical standards in the Helsinki Declaration of 1975 and approved by EGI's Institutional Review Boards (IRB). Informed consent was obtained for each subject.

The ranges used to train the reduced models for each subject were initially expanded to the minimum and maximum conductivities given in Table 4.1. We then trained secondary reduced models with the conductivity range for spongiform bone expanded to [0.001, 0.3] S/m to include the values estimated by Fernández-Corazza et al. (2018).

To replicate those results, we first ran the IP considering the scalp, compact bone and spongiform bone compartments to be estimated and all others fixed to the same values used in [63] for both ranges of conductivities. We then ran the IP considering all compartment conductivities to be estimated simultaneously, for the ranges given in Table 4.1.

5.5.1 Results

Table 5.2 shows the average and standard deviation in the conductivity estimations obtained for the three participants considering the full conductivity ranges in Table 4.1. Similarly,

Subject	Scalp (mS/m)	Compact bone (mS/m)	Spongiform bone (mS/m)
AM	243 ± 45	5.5 ± 2.0	34 ± 14
CA	287 ± 62	4.8 ± 1.3	48 ± 30
AA	360 ± 88	4.8 ± 1.9	11 ± 17
AM	214 ± 58	5.5 ± 2.5	195 ± 128
CA	277 ± 64	4.1 ± 1.1	225 ± 103
AA	345 ± 98	4.8 ± 2.1	174 ± 143

Table 5.2 Conductivity estimations by subject data and compartment considering all intracranial compartments fixed using reduced model trained in the ranges from Table 4.1 (top three rows) and the expanded spongiform range (bottom three rows).

the values estimated considering the expanded spongiform bone range can also be found in Table 5.2. These values are in strong agreement with the results obtained by Fernández-Corazza et al. (2018) who obtained (for AM, CA and AA, respectively) scalp values of 249, 291, and 362 mS/m and compact skull values of 4.16, 4.22 and 4.25 mS/m with similar standard deviations [63]. Table 5.3 contains the estimations for all tissues, found simultaneously, considering the ranges in Table 4.1. Note that in the interest of lowering the standard deviations of the estimations, we arbitrarily expanded the ranges used to train the reduced models for all tissue compartments and found no improvement. Similarly, we increased the number of snapshots taken to build the model up to 130 and still found no improvement over estimations made with 40 snapshots. The spongiform bone estimations are more difficult to compare, given the change in the estimations when the training ranges were altered, and the significant standard deviations in the estimations across the electrode pairs, suggesting estimations instability. However, the coefficient of variation in the spongiform bone estimation is similar to that obtained by Fernández-Corazza et al. (2018).

It took approximately two hours to train each of the models up to 40 snapshots and 10 seconds to run all IPs for each subject. This is much faster than the estimations obtained by Fernández-Corazza et al. (2018), which took days.

5.6 Discussion

We have presented a framework for the solution of the pEIT-FP using ROM, where we have demonstrated a significant reduction in computational expense, resulting in a framework at least 30 times faster than that of the current state-of-the-art approach. Similarly, we have

Subject	Scalp (mS/m)	Compact bone (mS/m)	Spongiform bone (mS/m)
AM	237 ± 42	6.4 ± 2.5	35 ± 14
CA	271 ± 64	6.0 ± 2.7	45 ± 29
AA	337 ± 94	5.9 ± 2.8	18 ± 27
	CSF (mS/m)	GM (mS/m)	WM (mS/m)
AM	1455 ± 145	303 ± 278	118 ± 72
CA	1448 ± 138	231 ± 219	114 ± 63
AA	1433 ± 219	219 ± 259	99 ± 60

Table 5.3 Conductivity estimations of all compartments by subject data using reduced model trained in the ranges from Table 4.1.

shown that huge improvements can be achieved in conductivity estimations for all tissues, many previously unreachable by pEIT in a reasonable time frame due to computational effort.

5.6.1 Synthetic Data

We have validated this approach experimentally by testing both methods on a realistic 6-layered head model to emulate typical use cases. Fig. 5.1 exhibits the speed up and accuracy improvement of using ROM-pEIT over the traditional method when the inner tissue conductivities are assumed to be known. A more realistic scenario would be that the inner tissue conductivities are unknown. In this instance, we found that after 200 full order systems solved the error in scalp estimations was half an order of magnitude higher than that achieved assuming the inner conductivities known (Fig. 5.1). We also found that the spongiform bone could not be estimated reasonably for the traditional algorithm.

For models that have been built from only T1-weighted MRI images, where segmenting spongiform bone in the skull accurately is not feasible, it has been shown to reduce errors in the EEG FP and IP when the anisotropy of the skull conductivity is considered [193]. In this context, ROM-pEIT also extends to such a situation. Fig. 5.4 also shows us that this IP is more sensitive to the radial conductivity than the tangential conductivity, which is consistent with reported findings [60]. The reduced anisotropic model is also bounded and we found that, for 30 snapshots, the mean $\Delta_{RE}(\boldsymbol{\sigma})$ was approximately 10^{-2} and the mean $\mathrm{RE}(\boldsymbol{\sigma})$ was 10^{-4}.

The interior-point optimisation afforded by the use of ROM-pEIT FPs was chosen based on its flexibility to handle large and small scale problems and the accuracy it provided in the IP estimations. In Experiment 2, this algorithm performed well, however, it is useful to assess its stability in the presence of different intensities of noise. Fig. 5.2 displays the results for this analysis. For the purposes of pEIT, this optimisation technique appears robust, however, other methods could be explored. With the speed of ROM-pEIT the analysis of other optimisation algorithms would become a less onerous task.

Furthermore, we provided evidence that the choice of reference electrode clearly effects the amount of standard deviation in the estimates substantially, as shown in Fig 5.5b. This value is most affected over areas of modelling inaccuracy and vary by as much as 1.5 times the average. Fig 5.5b demonstrates that errors in the potential at the reference electrode in the FP are propagated to all other electrodes, resulting in larger standard deviations in the estimations of each IP. Therefore, regardless of re-referencing scheme, the original reference can have a substantial impact when modelling inaccuracies are present.

This observation has wide implications in the field of EEG, TES and pEIT given that the reference electrode is often fixed in commercial electrode arrays to the centroparietal

midline [86]. Therefore, we suggest this standard practice be revisited to allow more flexible control of the position of the reference electrode.

It is worth noting that ROM-pEIT is useful for a pEIT setup with any number of electrodes. Here, we have provided a sensitivity analysis of ROM-pEIT applied to a typical pEIT setup, however, to further assess the validity of this methodology under different pEIT conditions, this analysis should be extended. This extension would include the impact of electrode position error, different sensor layouts and numbers, and contact impedance variability. These parameters are beyond the scope of this thesis, however, they will be subject to further investigation.

In addition, we found that, even with noiseless data, the estimation accuracy of all tissues was limited by the optimisation algorithm due to the complexity of the solution space being explored. This could b a limitation of the interior-point algorithm although other methods were briefly explored and no additional accuracy was found. For example, the particle swarm/multi-start approach was briefly explored, where the same optimisation is run with many combinations of starting conditions. However, this saw little benefit and the number of particles needed to sample a 6-dimensional space meaningfully was questioned. This difficulty was partially solved with the use of adjacent injection patterns and a custom pEIT protocol with staged optimisation, where the spongiform bone estimation improved, as exhibited in Fig. 5.6.

5.6.2 Real Data

The ROM-pEIT framework has demonstrated strong agreement with the traditional method for the real pEIT data from three subjects [63]. It was expected that, given the additional freedom of the other compartments being estimated, the standard deviation in the estimations across the electrode patterns may reduce thanks to the entire model becoming more individualised, therefore removing errors introduced by incorrectly assigned conductivities. In this context the ROM-pEIT framework has proven in simulated data that searching the parameter space of this dimensionality is trivial. However, as seen in Tables 5.2- 5.3, the coefficient of variation of the spongiform bone, CSF, GM and WM all remained high. When the ranges were expanded, the coefficient of variation in all tissues remained approximately the same.

Combined with the analysis of the reference placement and the importance of anatomically correct head models, confirmed in Table 5.1, this leads us to hypothesise that a standard modelling assumption could be causing the variability in the estimations of a single subject. Given the standard deviations in the estimations of all compartments, the assumption of a homogeneous scalp layer could be playing a role. This may be reasonable to challenge due to its complex structure [58], role in EEG source localisation [187] and fat content [144].

Additionally, sutures in the skull have been shown to significantly influence the EEG FP and IP [115]. Although its effect on pEIT is less certain, it is likely to have a similar effect given the large differences in conductivity between pure compact bone in the skull and sutures [41].

From these observations, an investigation into the common modelling assumption of a single homogeneous scalp layer is warranted, and could have wide implications for the field of EEG, which relies heavily on these models. Crucially, this *strongly* emphasises the need of pEIT and specifically the ROM-pEIT framework to challenge modelling assumptions. Without these tools, investigations of this nature would be incredibly taxing. We believe the framework we present is an essential tool for researchers in this context. Furthermore, as shown with the synthetic data, estimation stability is affected significantly by the presence of model inaccuracies. This instability can even be manipulated by the positioning of the reference electrode. The instability in estimations, which would be represented by large standard deviations in the conductivity estimations across electrode pairs, could be a key metric for the assessment of the validity of modelling assumptions.

The real data used here was taken from male subjects with similar ages, between 44 and 52. This could be a transitional period for skull conductivity given that many sutures in the skull are hypothesised to decrease in conductivity up until this age range approximately [115]. This may explain why subject AM has a higher skull conductivity than the others, being a younger subject. The methodology we present could be used to aid research into changes in skull conductivity with age, particularly given that reduced models could be reused and therefore subjects could be monitored over time with ease.

5.6.3 Related Work

Some efforts have been made to avoid the computational expense of pEIT while retrieving subject-specific conductivity values. Akalin Acar et al. (2016) [5] and Costa et al. (2017) [46] demonstrated techniques for the simultaneous estimation of the conductivity of the skull and the location of the source of electrical activity. Others have used a pre-calibration technique for combined EEG and MEG where an initial conductivity value for the skull is given and then tuned before the source localisation by using somatosensory evoked potential data [198, 16, 10]. However, these techniques have only been demonstrated for estimating the skull and brain conductivities. Moreover, the method presented in [5] which uses only EEG data requires computational effort to converge, reported to be in the order of days by the authors. Using ROM-pEIT allows all compartments to be estimated simultaneously in a reasonable time frame.

The computational costs of ESI related methods become particularly prohibitive when performing sensitivity analyses, where effects of conductivity uncertainty in specific head tissues is explored. One way this problem has been circumvented is through the use of generalized Polynomial Chaos (gPC) expansions, where a result distribution is described by a linear combination of multivariate orthogonal polynomial basis functions and corresponding coefficients [155, 184]. Similarly to ROM, this method involves the calculation of the model output at multiple points on a sparse grid with specific parameters required to weight the coefficients. This technique was utilised by Schmidt et al. (2015) [155] for a sensitivity analysis in transcranial Direct Current Stimulation (tDCS) and by Vorwerk et al. (2019) [184] in EEG. Generalised PC has also been used for a conductivity uncertainty analysis in transcranial magnetic stimulation (TMS) and tDCS by Saturnino et al. (2019) [153]. Although resulting in an essential reduction in computational effort for these experiments, they still required the evaluations of the full FP at hundreds of points in parameter space for gPC convergence. The framework we present requires only a few dozen full order FP evaluations to reach a low RE in the FPs and IPs.

A closely related work by Maksymenko et al. (2020) also demonstrates a reduced order technique for fast solutions of the EEG FP [111]. Similarly, this framework used a set of full-order solutions at points in parameter space chosen via a greedy algorithm. This model could generate approximate lead field matrices for any conductivity set in parameter space very rapidly. There are, however, some notable differences between this framework and the one that we present in this work. Firstly, the implementation differs, where the former is applied to the EEG FP and solved using the Boundary Element Method with a small number of nodes in a model with 3 tissue compartments. Although it is suggested that it could equally be applied to FEM, this is not shown. Fundamentally, we present a rigorous *a posteriori* bound on the error in the reduced FP solution, and explicitly show this using a set of samples across the parameter space. Whereas, in the aforementioned publication [111], the error is not properly bounded.

Similarly, work by Codecasa et al. (2016) [44] has merged the techniques of ROM and gPC to perform an uncertainty analysis in TMS, where the model order reduction is used to guide the selection of the conductivity samples used for the polynomial chaos expansion. This work resulted in a significant speed up over gPC with regression, demonstrating the power of reduced order model techniques. There are a few differences in our work that make it distinguishable from this, such as a bound on the approximation error, application to pEIT, and the investigation of 3 additional tissues (scalp, compact skull and spongiform skull).

For studies involving gPC, where a model is trained using hundreds of support points, all were sensitivity analyses. Due to the nature of this work it is essential to have a highly

trained model. However, for personalised conductivity field reconstruction, there is more interest in reducing the time from measurement to result. This is one of the strengths of ROM-pEIT. Shown in Figs. 5.1 and 5.3, only $10-30$ support points per injection pattern are required for accurate estimations in all tissues.

McCann et al. (2019) showed that spongiform bone varies between subjects and measurement techniques and that few attempts have been made to measure the conductivity of this tissue *in vivo*. Fernández-Corazza et al. (2017) [63] used pEIT but with a significant standard deviation and Aydin et al. (2014) [16] used the pre-EEG calibration method. The latter found a spongiform conductivity of 84 mS/m [16] while the former found 173 ± 151 mS/m [63]. In the case of the former, a mixture of random error and numerical error (both present when using real data) may be responsible for the large standard deviation, however, the comparisons we draw above only consider numerical error. Clearly, *in vivo* measurements of spongiform bone have been challenging and the distribution of conductivity of this tissue among the population remains poorly understood as a result. The framework that we present is able to estimate spongiform bone to a high level of precision *in vivo* at the frequencies used for ESI, which as of writing has not been achieved by any other validated method in the literature. Furthermore, to the best of our knowledge, only two studies on non-invasive *in vivo* estimations of the CSF are present in the literature, with large errors in the estimations reported [127, 67]. Although, highly invasive *in vivo* measurements of CSF have found very little variance over a handful of subjects, non-invasive methods such as the one presented could verify this with large studies [21].

It is worth emphasising the difference between imaging EIT and pEIT. For the imaging modality of EIT, dimensionality reduction techniques have been explored in the form of basis constraints [177] and autoencoders [159], amongst others. Fundamentally, these approaches are tuned towards imaging EIT, which is a different type of problem to parametric EIT, distinguished by how ill-posed the IP is. For imaging, the conductivity at each pixel/voxel is reconstructed from only a handful of electrode measurements, whereas, in parametric EIT, only a handful of conductivities are estimated from as many as 256 electrode measurements. In the case of both aforementioned techniques, an approximate solution manifold is made, similarly to ROM. However, with basis constraints, the support points are hand selected, whereas, with autoencoders, the number of support points required is over 20,000 for a 16-channel system. The ill-posed nature of imaging EIT also requires stabilisation techniques such as Tikhonov regularisation [178]. This type of stabilisation does not apply here.

5.6.4 Future Work

A key feature of this work is the certified upper bound on the error in the FP. Although it guarantees a maximum error for each snapshot number, its usefulness as a stopping criteria is limited given the sharpness of the bound. A further challenge is that drawing a connection between the error in the FP and IP is not trivial. However, from Figs. 5.1 and 5.3 it is clear that optimal performance was achieved after 30 snapshots. Additionally, when the error between the full-order and the RB signal becomes much smaller than the noise, eq. (3.53) becomes approximately the norm of the noise over the electrodes. Relative to the measurements, that becomes approximately $4-5\times10^{-6}$ RE($\boldsymbol{\sigma}$) (for the noise we have used), which on Fig. 4.4 corresponds to about 30 snapshots, as observed in the IP. For our head model, this connects the observations in the FPs and IPs and therefore we suggest 30 snapshots as the optimal number and this can serve as a stopping criteria. However, this could change between participants, and more work is needed to confirm how variable this would be.

However, we emphasise that this choice in snapshot number could change depending on the head model discretisation, level of noise in the measurements, and the number of conductivities to estimate (as this will affect the dimensionality of the parameter space). When applied to the head models of the real participants, we found no change in estimation stability past 40 snapshots. This further supports the idea that we should challenge our modelling assumptions. Nevertheless, a full analysis to characterise this value is due.

McCann et al. (2022) also investigated the effect of sutures on the EEG FP and IP and found that omission of the sutures from a head model led to significant source localisation errors [115]. It is unclear how the inclusion of sutures in a realistic head model may affect the training of the reduced order model, however this should be considered in future models. Moreover, with the possibility of estimating inner tissue compartments, the impact of including sutures on the estimation of the inner compartments could be assessed.

TDCS has been shown to produce a greater intensity and focality of the electric current at a point of interest when highly accurate head models are considered [188] and optimal injection patterns are generated [148]. ROM could reduce the time constraints involved and in an online process estimate the conductivities and optimal injection patterns together almost instantly. Future work could involve producing a pipeline for TDCS such that the number of measurements taken from the patient are kept to a minimum.

Another avenue for future development is exploring the effect of injection patterns on the estimation accuracy. The staged optimisation we present partially explores this, however, it introduced many variables, with unknown effects if changed. For example, the position of the injection electrode for the for the first set of patterns was chosen arbitrarily, and changing this position may effect the estimation of the scalp. Similarly, the second set were chosen to

be comparable with the first experiments in synthetic data, however, they could possibly be chosen to be more sensitive to the inner tissues (e.g. white matter) and possibly improve the white matter estimations. A full sensitivity analysis on the effect of injection pattern protocol on the estimation accuracy in each tissue is warranted. Such investigations are now made much more accessible by the ROM-pEIT framework.

Many modern EEG systems have the capability of estimating the contact impedance of each electrode placed on the scalp, while some work has attempted to reconstruct the impedances form EIT data [35, 181]. The contact impedance for the electrodes in this work were set as constant, justified by previous work, and the small size of the electrodes. However, it is possible this reconstruction could be added to the framework and this may be explored in future.

In conclusion, this new framework embodies a fresh approach to pEIT that will change its accessibility and reliability, recasting its role in the generation of personalised realistic head models used for ESI methods.

The software developed for this research can be found here:
https://github.com/09nwalkerm/ROMpEIT.

5.7 Summary

Chapter 4 described the training and accuracy of the reduced model for its use in the pEIT-FP. This chapter has explored its incorporation into the pEIT-IP and the affect this has on the accuracy and speed of the technique as a whole. A new framework, has been suggested utilising the interior-point optimisation method to solve the IP, replacing the traditional gradient-assisted Newton optimisation. This framework was then extensively tested in a variety of common use cases. The main findings of this chapter can be summarised as follows:

- The IP performance of ROM-pEIT framework (including training) is significantly faster than the traditional method. For a 3-parameter optimisation in the traditional method, ROM-pEIT is approximately 30 times faster, even when estimating 6 parameters simultaneously. Due to its infeasibility, a 6-parameter search could not be performed with the traditional method, showing the significant improvement obtained by using ROM-pEIT. Consequently, the new capability to estimate every tissue in the head model has been unlocked, allowing a far more effective characterisation of individual tissue conductivities.

- It is shown that the framework presented is also robust in the presence of high amounts of noise. For Gaussian noise with a standard deviation 10 times greater than that found in real measurements, the relative error in the conductivity of the scalp is less than 3×10^{-3} when using the new framework.

- The use of an anisotropic conductivity in the skull was also demonstrated in the new ROM-pEIT framework, with similar results regarding time saved and the accuracy of the tissue conductivities estimated.

- With a speed-up of orders of magnitude, new experiments can be designed, previously impossible in a reasonable time frame. This is demonstrated by assessing the impact that the choice of reference has on the standard deviations in the estimations of all injection pairs, in the context of missing spongiform bone information. This experiment was performed by training the reduced models for pEIT without any spongiform bone in the skull and generating synthetic measurements with the spongiform in the skull. The results show that the choice of reference location has a noticable impact on the standard deviation of the estimates from each injection pair.

- ROM-pEIT was also validated using real pEIT data, but comparing the estimations with the previous state-of-the-art method. Our results agree strongly.

- Analysis of the standard deviations in the real data estimations suggest that there is something missing from our models. This discovery could only be possible with ROM-pEIT, now that the computational limitation has been removed.

- With the computational limitation removed, the complexity of the solution space hinders further accuracy improvements as the optimisations becomes stuck in local minima. To overcome this, new pEIT protocols were explored where injection patterns that target the scalp conductivity were used to reduce the dimensionality of the solution space, thus improving the accuracy of further IPs. This expanded pEIT protocol led to improved spongiform bone estimation.

Chapter 6

Fast Simultaneous Conductivity Estimation and Source Localisation in EEG using Reduced Order Modelling

6.1 Overview

Previous chapters have detailed ROM applied to the pEIT-FP. This chapter utilises the same reduced models with the adjoint problem for the EEG-FP. The Primal-Dual Equivalence is first described, and the pEIT-FP is linked to the EEG-FP. The use of ROM in the pEIT-FP then being exploited in the EEG-FP is highlighted. This theory is then implemented and validated in a similar way to previous chapters. The fundamental improvement this allows is the ability to generate an entire leadfield matrix for any conductivity set. This enhancement is then utilised for simultaneous conductivity and source localisation.

This chapter has been adapted from the work prepared for publication: Matthew R. Walker and Leandro Beltrachini, Fast Simultaneous Conductivity Estimation and Source Localisation in EEG using Reduced Order Modelling. Leandro Beltrachini contributed to the conceptualisation and programming of the work. All other work is that of the author of this thesis.

6.2 Introduction

In Chapter 2, we highlighted the importance of realistic head models and their impact on the ESI techniques that rely on them. In the following chapter, we introduced the leadfield matrix as a representation of the potentials on the electrodes for many sources, generated by

computationally expensive EEG-FPs. Given that the number of sources can be very large (sometimes up to 30,000), generating leafield matrices can be extremely costly. However, the use of EEG-IPs with head models untailored to a patient have been shown to have practical implications in real world use cases such as the localisation of epileptogenic zones [122, 119].

The skull is often touted as the most influential tissue in EEG source reconstruction. The modelling of its structure has been shown to impact the EEG-FP and EEG-IP strongly, making the case for anatomically accurate head models to be used [49, 119, 104, 42, 185, 175, 106, 19, 115]. Often overlooked is the use personalised conductivity parameters for the skull and other tissues, due to the lack of individual specific information. In this case literature values are often used as a substitute. However, it has been shown that the mischaracterisation of skull conductivity has a significant impact in EEG (as well as TES) and is as important as the structure [120, 153, 155, 18, 6, 172]. In the case of erroneous conductivities assigned to the skull, there is a clear impact on the depth the reconstructed source [184].

Concern over the skull conductivity is justified given the variations reported in the literature values from *in vivo* and *in vitro* measurements [41, 7, 8, 170, 116]. However, significant work has shown that all tissue conductivities impact the EEG-FP and EEG-IP, motivating the need for a more involved approach to conductivity estimation [184, 187, 81, 83, 193, 88]. One way to achieve a decent approximation of multiple tissues is through the use of pEIT (specifically ROM-pEIT, as shown in previous chapters [189]) thanks to the strong SNR in the signal [63, 53, 103, 79, 67, 47, 149, 125, 43, 132]. Unfortunately, this is not yet standard practice in the field, largely due to lack of equipment.

To partially address this problem, many have suggested the use EEG and MEG data such as SEP/SEF (somatosensory evoked field) readings to calibrate the skull and/or brain conductivities [10, 79, 23, 93, 198, 157, 70, 16]. SEP/SEF data is an attractive option because of how well it has been characterised in the literature as has been shown [195, 11, 10, 9]. To circumvent the cost associated with MEG, others have presented frameworks for the use of SEP-only data to calibrate conductivities [80, 173, 111]. Some have even suggested the use of any EEG data to tune conductivities [5, 101, 46]. Additionally, avoiding the need for calibration of the skull entirely has been explored through the selection of the inverse algorithm [163] and using Bayesian inference [145, 101].

A common disadvantage amongst all of these these methods is that they are plagued by computational constraints, often imposed by the calculation of leadfield matrices, limiting the techniques to calibrate only one or two tissues. The use of fast transfer matrices [196] and GPU implementations [90] can (and are) employed to aid these efforts, but are still too computationally expensive to explore more than one tissue for a refined realistic head model.

In this chapter, we propose the integration of ROM in the adjoint EEG-FP (pEIT-FP) to generate fast lead field matrices of the order of 3 seconds for any set of tissue conductivities. This allows the use of optimisation methods for simultaneous source localisation and conductivity estimation of all modelled tissues with only EEG data. Therefore, we employ synthetically generated SEP data to calibrate these tissue conductivities in a realistic 6-layered head model and explore the improvements in the FP and IP from the resulting tuned conductivity sets.

6.3 Methods

6.3.1 Reduced Order Modelling in the Dual Problem

In Chapter 3, we covered the treatment of the EEG-FP as a primal problem with a corresponding dual problem. The key aim of any primal-dual formulation is to isolate the solution values of interest in the primal problem, and find a dual problem that solves for only these value. In practical scenarios where these problems are solved numerically, the computational savings can be significant [75]. In the case of the EEG-FP, we are interested in only the potential on the electrodes, and the pEIT serves as its dual problem resulting in only $L-1$ problems to solve (see Chapter 3 for details).

With the pEIT-FP identified as the dual problem for the EEG-FP, we can now utilise our ROM-pEIT implementation from previous chapters to provide real-time solutions for the $L-1$ dual problems for any tissue conductivity set. The primal-dual equivalence can be shown in matrix form quite straightforwardly by multiplying the EEG-FP system eq. (3.41) by a selection matrix $\boldsymbol{H} \in \mathbb{R}^{(L-1)\times(n+L)}$, obtaining

$$\boldsymbol{H}\boldsymbol{u}_j^c(\boldsymbol{\sigma}) = \boldsymbol{H}\boldsymbol{A}(\boldsymbol{\sigma})^{-1}\boldsymbol{b}_j^{EEG}(\boldsymbol{\sigma}), \tag{6.1}$$

where

$$\boldsymbol{H} = \left[\mathbf{0}^{(L-1)\times n} \quad | \quad \boldsymbol{I}_{(L-1)\times(L-1)} \quad | \quad -\mathbf{1}^{(L-1)}\right] \tag{6.2}$$

and $\boldsymbol{b}_j^{EEG}(\boldsymbol{\sigma})$ and $u_j^c(\boldsymbol{\sigma})$ are the source vector and correction potential for the jth source, respectively. With some simple manipulation is can be seen that $\boldsymbol{H}\boldsymbol{A}(\boldsymbol{\sigma})^{-1}$ from eq. (6.1) can be transformed into $L-1$ pEIT-FP solutions in the following way

$$\boldsymbol{H}\boldsymbol{A}(\boldsymbol{\sigma})^{-1} = \boldsymbol{A}(\boldsymbol{\sigma})^{-1}\boldsymbol{H}^T = \boldsymbol{A}(\boldsymbol{\sigma})^{-1}\boldsymbol{b}_l^{EIT} = \boldsymbol{u}_l^{EIT}(\boldsymbol{\sigma}) \text{ for } l = 1, ..., L-1, \tag{6.3}$$

where, the reduced solution found with ROM-pEIT can be used as a replacement for the full-order pEIT-FP solution:

$$\boldsymbol{u}_l^{EIT}(\boldsymbol{\sigma}) \approx \mathbb{V}_l \boldsymbol{u}_l^N(\boldsymbol{\sigma}) = \boldsymbol{u}_l^N(\boldsymbol{\sigma})^T \mathbb{V}_l^T. \tag{6.4}$$

Substituting eq. (6.3) and eq. (6.4) into eq. (6.1) we find

$$\boldsymbol{H}\boldsymbol{u}_j^c(\boldsymbol{\sigma}) = (\boldsymbol{u}_l^N(\boldsymbol{\sigma}))^T \underbrace{\mathbb{V}_l^T \boldsymbol{b}_j^{EEG}(\boldsymbol{\sigma})}_{\mathscr{V}_{lj}(\boldsymbol{\sigma})} \tag{6.5}$$

where $\boldsymbol{u}^N(\boldsymbol{\sigma})$ can be calculated in real-time using eq. (4.5). With the reduced pEIT-FP model trained, eq. (6.5) already represents a significant speed-up, given that the biggest computational expense is now in the calculation of $\boldsymbol{b}_j^{EEG}(\boldsymbol{\sigma})$, which is far less than that of a full EEG-FP. While this can still be intensive when using the subtraction approach, as noted in Chapter 3, the use of faster source modelling approaches such as the St Venant approach could improve this.

At this stage, to generate a leadfield matrix with a specific set of tissue conductivities $\boldsymbol{\sigma}$ requires solving $L-1$ ROM-pEIT-FPs (requiring milliseconds to compute) and n_s source vectors (approx. 1 minute each on a standard PC for the analytical subtraction approach), due to its dependence on the conductivity. This is still too computationally intensive for a real-time setting. Therefore, in the next section, we construct source vectors that are independent of the conductivity, allowing the further splitting of the computational effort.

6.3.2 Affine Decomposition of $\mathscr{V}_{lj}(\boldsymbol{\sigma})$

The aim of this section is to formulate $\mathbb{V}_l^T \boldsymbol{b}_j^{EEG}(\boldsymbol{\sigma})$ into $\boldsymbol{\sigma}$-dependent and $\boldsymbol{\sigma}$-independent components. To achieve this we exploit the property of affine decomposition in the source vector, a property shared with the stiffness matrix. This allows the $\boldsymbol{\sigma}$-independent vectors to be precomputed, multiplied with $\mathbb{V}_l^T$ and then stored for each source for later use in the real time generation of leadfield matrices. The affine decomposition can be expressed mathematically as

$$\boldsymbol{b}_j^{EEG}(\boldsymbol{\sigma}) = \frac{1}{\boldsymbol{\sigma}^\infty}(\boldsymbol{b}_j^{CEM} + \sum_{p=1}^{P-1} \sigma_p^c \boldsymbol{b}_{jp}^v) + \boldsymbol{b}_j^s, \tag{6.6}$$

where P is the number of tissues in the model, $\boldsymbol{b}_v^p$ and $\boldsymbol{b}_s$ are the made with the first and second terms in eq. (3.44) respectively from the analytical method and $\boldsymbol{b}_{CEM}$ contains the

contribution from the final term in eq. (3.44). Multiplying eq. (6.6) by $\mathbb{V}_l^T$ leads to

$$\underbrace{\mathbb{V}_l^T \boldsymbol{b}_j^{EEG}(\boldsymbol{\sigma})}_{\mathscr{V}_{lj}(\boldsymbol{\sigma})} = \frac{1}{\boldsymbol{\sigma}^\infty}(\underbrace{\mathbb{V}_l^T \boldsymbol{b}_j^{CEM}}_{\mathscr{V}_{lj}^{CEM}} + \sum_{p=1}^{P-1} \sigma_p^c \underbrace{\mathbb{V}_l^T \boldsymbol{b}_{jp}^{v}}_{\mathscr{V}_{ljp}^{v}}) + \underbrace{\mathbb{V}_l^T \boldsymbol{b}_j^{s}}_{\mathscr{V}_{lj}^{s}}, \tag{6.7}$$

where the matrices $\mathscr{V}_{lj}^{CEM} \in \mathbb{R}^N$, $\mathscr{V}_{ljp}^{v} \in \mathbb{R}^N$ and $\mathscr{V}_{lj}^{s} \in \mathbb{R}^N$ for $l = 1, ..., L-1$, $j = 1, ..., n_s$ and $p = 1, ..., P-1$, can be precomputed and stored. The calculation of these matrices will be referred to as an offline phase, where the complementary online phase consists of linearly combining $\mathscr{V}_{lj}(\boldsymbol{\sigma})$ with eq. (6.7).

The affine decomposition above is performed for all sources separately. Therefore, the full decomposition of $\mathscr{V}_{lj}(\boldsymbol{\sigma})$ for $l = 1, ..., L-1$ and $j = 1, ..., n_s$ results in $P+1$ stored matrices with dimensions $N \times n_s \times (L-1)$.

6.3.3 Online Evaluation of a Leadfield Matrix

Finding $\mathscr{V}_{lj}(\boldsymbol{\sigma})$ requires only matrix multiplication and addition for relatively small matrices, which can be done very quickly. Combined with the speed of finding the reduced solution, resolving eq. (6.5) is almost real-time and, by extension, the leadfield matrix can made extremely quickly, even for a large n_s. For a highly refined realistic head model with 830,000 nodes, we were able to generate full leadfield matrices for 30,000 sources and any given $\boldsymbol{\sigma}$ in only 3 seconds.

6.4 Implementation and Experiments

6.4.1 Setup and Implementation

We used a realistic model of the head based on the Colin27 atlas, made with 830k nodes and over 5M elements and processed as in previous publications [115]. The number of electrodes modelled was 165 and six head tissues were segmented into different compartments. This model was processed from the same imaging data as used in Chapter 4, (see Fig. 4.3). The reduced models for the pEIT-FP were trained in the same way as in chapter 4 where the injection patterns all had electrode 165 as the common sink. This electrode was placed above the sagital suture in the Cz position. The source space contained 29,018 sources in the left hemisphere of the brain with orientations normal to the cortical surface and magnitudes of 2 nAm. The source vectors were calculated using the analytical subtraction approach [27].

The work was parallelised by distributing the sources on a cluster of 11 Intel(R) Xeon(R) X5660 CPU nodes at 2.80GHz. Each node had 12 cores and 192 GB of random access memory (RAM), and was responsible for processing $\mathscr{V}_{lj}^{CEM} \in \mathbb{R}^N$, $\mathscr{V}_{ljp}^{v} \in \mathbb{R}^N$ and $\mathscr{V}_{lj}^{s} \in \mathbb{R}^N$ for $l = 1, ..., L-1$ and for 700 sources (j). The high amounts of RAM is needed to simultaneously work on the 700 sources (each with seven source vectors - see decomposition) and at least one $\mathbb{V} \in \mathbb{R}^{(n+L)\times N}$ at any given time. The infinity potential $\boldsymbol{b}^{\infty}$ is calculated and stored separately and can be added to the leadfield matrix in real time after a simple multiplication with $\boldsymbol{\sigma}^{\infty}$.

6.4.2 Numerical Leadfield Error

To verify the validity of this method and confirm the reducibility of the EEG-FP, the leadfield matrix generated using ROM is compared to the leadfield matrix constructed using standard EEG-FPs (i.e. the primal problem). The source space first needs to be reduced to make this validation feasible. A source subspace of 1000 dipoles is selected uniformly across the cortical surface to form leadfield matrices with 1000 sets of electrode potentials, all referenced to electrode 165 (Cz). Both leadfield matrices were made for 50 random conducitivty samples, selected within the IQ range shown in Table 4.1. This was repeated for 100 snapshots used in the pEIT-FP (i.e. the dual problem). To compare the leadfield matrices, we used the relative error (RE) between the two sets of potentials for a particular source. First we define a general RE between two values a and b as

$$RE(a,b) = \frac{||a-b||_2}{||b||_2}. \tag{6.8}$$

Then the RE between two sets of potentials is $RE(\boldsymbol{U}_j^P, \boldsymbol{U}_j^D)$, where $\boldsymbol{U}_j^P$ is the set of potentials for the jth source in the leadfield matrix made from the primal problem and $\boldsymbol{U}_j^D$ is the dual equivalent. This was repeated for each source, conductivity sample and snapshot number. The maximum and average of these values was plotted as a function of snapshot. To demonstrate the reduction in RE, the maximum value across the conductivity samples was plotted on an inflated cortex for snapshot numbers 10, 15, 20 and 30.

6.4.3 Simultaneous Conductivity Estimations and Source Localisation

Synthetic SEP Data

The first SEP components have been suggested to originate from single dipoles or combinations of single dipoles in the brain stem, and primary somatosensory cortex with both tangential and radial orientations [36]. The tangentially orientated dipole source is thought to

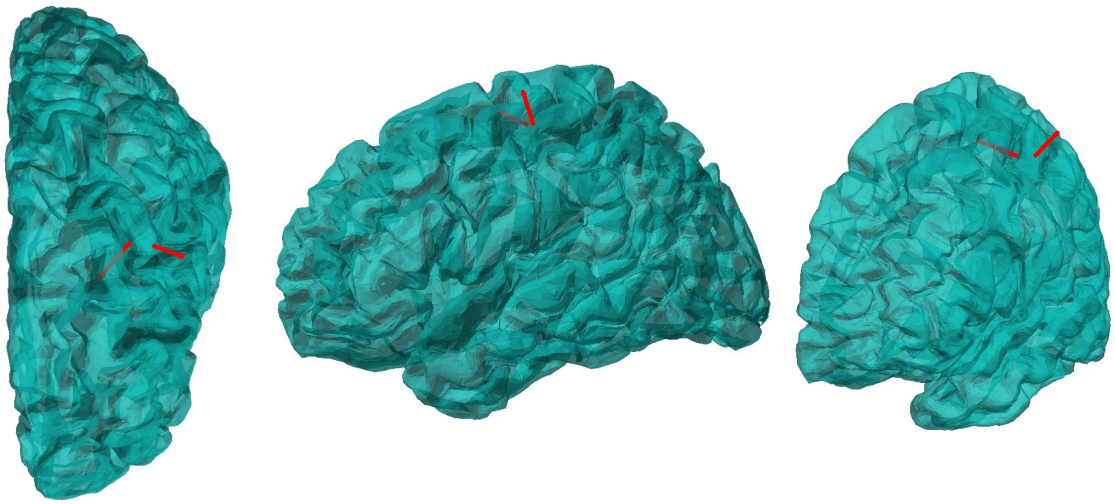

Fig. 6.1 Position of quasi-radial and quasi-tangential dipole sources (red arrows) on the left hemisphere of the cortex. The views are (from left to right) in the axial plane, saggital plane and half way between the saggital and coronal plane.

be responsible for the P20/N20 component with a radially orientated source responsible for the P22/N22 component [36, 22]. Significant work utilising SEP/SEF data for conductivity calibration thus far has focused on the use of the tangentially oriented dipole source due to MEGs insensitivity to radially oriented sources [86]. However, work has been done to extract brain and skull conductivities using simultaneously simulated (and reconstructed) tangential and radial dipoles [108, 70]. Here we use a similar paradigm, however, we generate two distinct sets of measurements to replicate both the P20/N20 and P22/N22 component; one from a single quasi-tangential source on the anterior wall of the postcentral gyrus (Brodmann area 3b) and one from a single quasi-radial source on the top of the postcentral gyrus (Brodmann area 1). Fig. 6.1 shows the positions of these two dipoles on the cortical surface. For each component we generated three sets of noisy measurements with different SNRs for 50 different conductivity sets. We used additive Gaussian noise with SNRs of 40 dB, 25 dB and 20 dB, as used in previous studies [108], where 25 dB has been found in real data [108, 70].

Simultaneous Optimisation of Sources and Conductivities

With the new capability to generate leadfield matrices with very little computational effort, new methods that were previously infeasible can be conceptualised. We present an algorithm for the simultaneous reconstruction of conductivities and dipole sources from two SEP components. The measurements for each SEP component would be the potentials on the

electrodes at the post-stimulus time associated with the component. The principle approach here is to minimise the RE (RE_{20} and RE_{22}) between the SEP component measurements ($\boldsymbol{y}_{20}$ and $\boldsymbol{y}_{22}$) and the electrode potentials ($\boldsymbol{U}(\boldsymbol{\sigma},\boldsymbol{r}_{20})$ and $\boldsymbol{U}(\boldsymbol{\sigma},\boldsymbol{r}_{22})$) of a set of reconstructed sources ($\boldsymbol{r}_{20}$ and $\boldsymbol{r}_{22}$) made with the conductivity set $\boldsymbol{\sigma}$. This can be expressed mathematically as

$$\begin{aligned}\underset{\boldsymbol{\sigma},\boldsymbol{r}_{20},\boldsymbol{r}_{22}}{\arg\min}\{&(\boldsymbol{y}_{20}^T\boldsymbol{y}_{20})^{-1}(\boldsymbol{y}_{20}-\boldsymbol{U}(\boldsymbol{\sigma},\boldsymbol{r}_{20}))^T(\boldsymbol{y}_{20}-\boldsymbol{U}(\boldsymbol{\sigma},\boldsymbol{r}_{20}))\\ &+(\boldsymbol{y}_{22}^T\boldsymbol{y}_{22})^{-1}(\boldsymbol{y}_{22}-\boldsymbol{U}(\boldsymbol{\sigma},\boldsymbol{r}_{22}))^T(\boldsymbol{y}_{22}-\boldsymbol{U}(\boldsymbol{\sigma},\boldsymbol{r}_{22}))\},\end{aligned} \tag{6.9}$$

where the RE for each component is $RE_{20} = RE(\boldsymbol{U}(\boldsymbol{\sigma},\boldsymbol{r}_{20}),\boldsymbol{y}_{20})$ and $RE_{22} = RE(\boldsymbol{U}(\boldsymbol{\sigma},\boldsymbol{r}_{22}),\boldsymbol{y}_{22})$. For this minimisation task we employ the interior-point optimisation algorithm to search for the conductivity set while each function evaluation in the optimisation contains a nested sLORETA algorithm to search for the reconstructed dipoles. The full optimisation can be summarised as follows,

1. Set initial guess $\boldsymbol{\sigma}_{new} = \boldsymbol{\sigma}_0$ (mid point of ranges in Table 4.1).
2. Generate leadfield matrix with $\boldsymbol{\sigma}_{new}$.
3. Perform sLORETA algorithm with $\boldsymbol{y}_{20}$ and leadfield, reconstructing dipole position.
4. Perform sLORETA algorithm with $\boldsymbol{y}_{22}$ and leadfield, reconstructing dipole position.
5. Select dipole position for each component from leadfield matrix and find the sum of the RE [i.e., $(RE_{20}+RE_{22})$].
6. Repeat steps 2-6 (one function evaluation) until interior-point algorithm chooses new conductivity set $\boldsymbol{\sigma}_{new}$.
7. Repeat steps 6 until a minima is found.

In a similar way to Chapter 5, our first experiment aims to assess the accuracy of the reconstructed conductivities. We consider again the RE in the conductivity estimations as a function of the number of snapshots used in the dual problem. Here, the RE is the same as defined in eq. (5.2) and the snapshots in the dual problem is the number of iterations in the greedy algorithm used to train the reduced models used in the adjoint pEIT-FP. We ran the optimisation detailed above for 50 sets of conductivities and three different SNRs in the synthetic SEP data and for each number of snapshots. We the plotted the average RE for each tissue conductivity estimated across the 50 conductivity samples and for each of the SNRs.

Additionally, we also considered the scenario where the CSF, spongiform bone and GM are known, to replicate a common modelling case where only the skin, skull and brain are considered in the estimation. The same procedure is repeated and results are plotting in the same way as above.

Forward and Inverse Errors

It is important to explore how meaningful the conductivity estimations are and ultimately if they lead to lower errors in the FP or IP. To assess the error in the FP, we generated leadfield matrices using the true conductivity values of each of the 50 sample conductivities, followed by leadfield matrices with the estimated conductivities (at 30 snapshots) for each of the samples, for each of SNR. Leadfield matrices were also made the conductivities from the middle of the ranges in Table 4.1 as a comparison. The leadfield matrices were made using the same adjoint framework, but with 150 snapshots used to train the reduced pEIT-FP, to guarantee low errors for the entire source space.

The RE between the potentials in the true leadfield matrix and the others was found for each source, and the maximum and average for each source across all samples was plotted on an inflated cortex. This was repeated for each level of noise and the mid-point conductivities. The RE here is defined as $RE(\boldsymbol{U}^j_{EST}, \boldsymbol{U}^j_{TRUE})$, where $\boldsymbol{U}^j_{EST}$ are the potentials for source j in the leadfield matrix generated using either one of the estimated conductivities or the mid-point conductivities and $\boldsymbol{U}^j_{TRUE}$ are the potentials for source j in the leadfield matrix generated using the true conductivities.

For the IP, the sLORETA algorithm was performed using both the leadfield matrices generated from the conductivities estimated from the 25dB SNR signal and mid-point conductivities, where the true conductivity leadfield matrices were used as the measurements (i.e., without any noise in the measurements). For both leadfield matrices and each source, the maximum and average localisation error in millimeters across all conductivity samples was plotted on the inflated cortex.

6.4.4 Simultaneous EIT and EEG Conductivity Estimation

Finally, as an exploratory experiment, we combined the strengths of both pEIT-based conductivity estimation and SEP-based conductivity estimation. We used the same signals generated previously for the 50 conductivity samples and 3 SNR values. Firstly, we used ROM-pEIT to estimate the scalp and skull conductivities using the staged algorithm described in Section 5.3.5. Secondly, we use a combination of the staged algorithm and the algorithm described in Section 6.4.3 to reconstruct the final tissues. This combination consists of

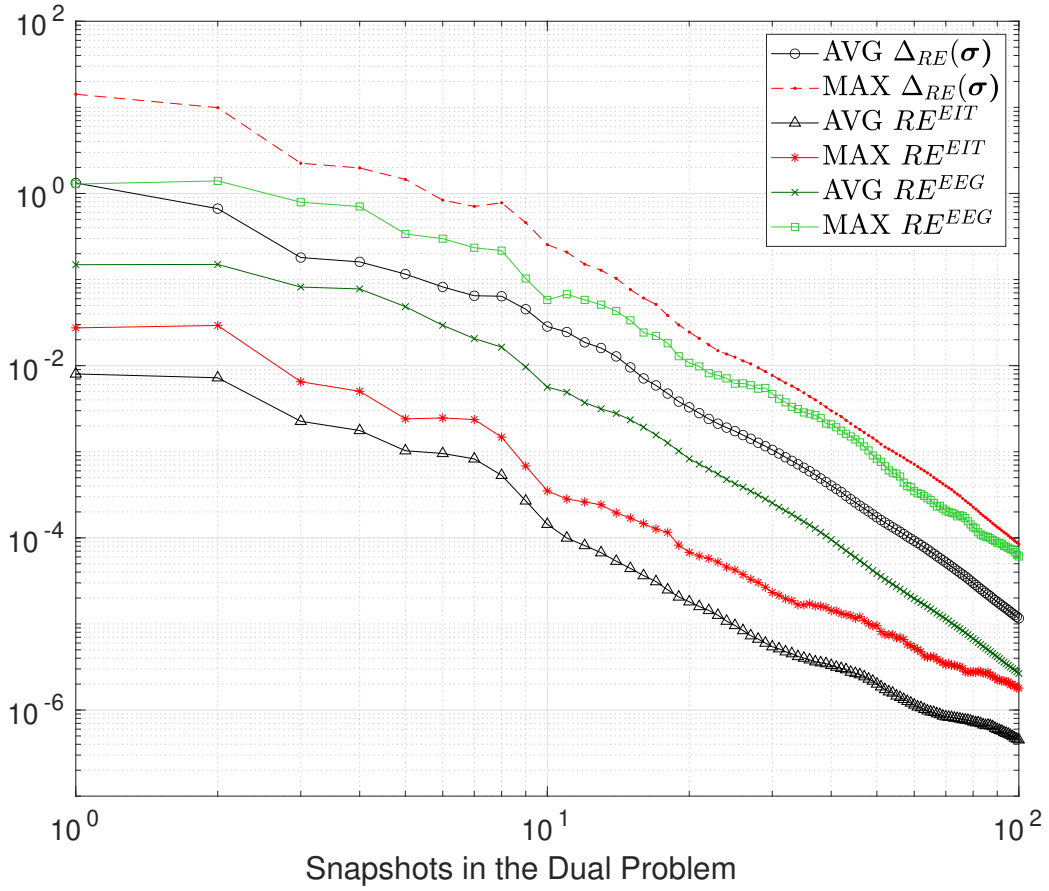

Fig. 6.2 Overlaid on Fig. 4.4 is the maximum and average RE (light green and dark green, respectively) in 1000 dipoles in the leadfield matrices generated for 50 conductivity samples as a function of the snapshots used to train the dual problem (ROM-pEIT). Here, RE^{EEG} is $RE(\boldsymbol{U}_{EST}, \boldsymbol{U}_{TRUE})$ and $RE^{EIT} = RE(\boldsymbol{\sigma})$ and $\Delta_{RE}(\boldsymbol{\sigma})$ are defined in eq. (4.1).

minimising both the pEIT-based RE and then SEP-based RE simultaneously. The pEIT measurements used for estimation used the same protocol as described before, with the same Gaussian noise with standard deviation 0.82 μV. The average RE (defined in eq. (5.2)) in the conductivity estimations across the 50 samples was plotted per tissue for each of the SNR values.

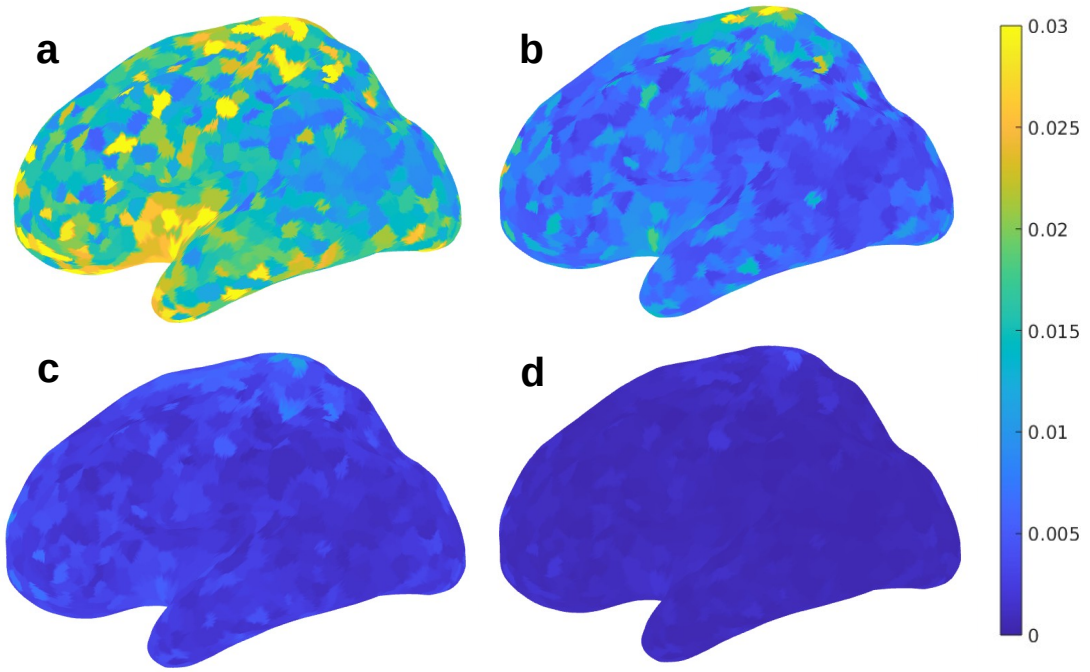

Fig. 6.3 Maximum RE in the FP across 50 conductivity samples for 1000 sources plotted on an inflated cortex for **a)** 10, **b)** 15, **c)** 20 and **d)** 30 snapshots used to train the dual problem (ROM-pEIT).

6.5 Results

6.5.1 Numerical Leadfield Error

Fig. 6.2 displays the maximum and average RE in 1000 dipole sources in the leadfield matrix for 50 conductivity samples for each number of snapshots used in the dual problem as described in Section 6.4.2. Additionally, Fig. 6.2 shows a comparison between the RE in the leadfield matrix and the RE in the dual problem (ROM-pEIT) with the relative error bound $\Delta_{RE}(\boldsymbol{\sigma})$ also displayed. Notice how $\Delta_{RE}(\boldsymbol{\sigma})$ decreases at the same rate as the RE in the leadfield matrix and appears to also tightly bound this error.

We also show in Fig. 6.3 the maximum RE across all conductivity samples for each source and plot this on an inflated cortex for different number of snapshots used in the dual problem. From this figure, it is clear that the RE in the sources across the entire cortex are decreasing with increasing snapshots and that 30 snapshots is sufficient to obtain maximum relative errors below 0.005 for any conductivity parameter and source combination.

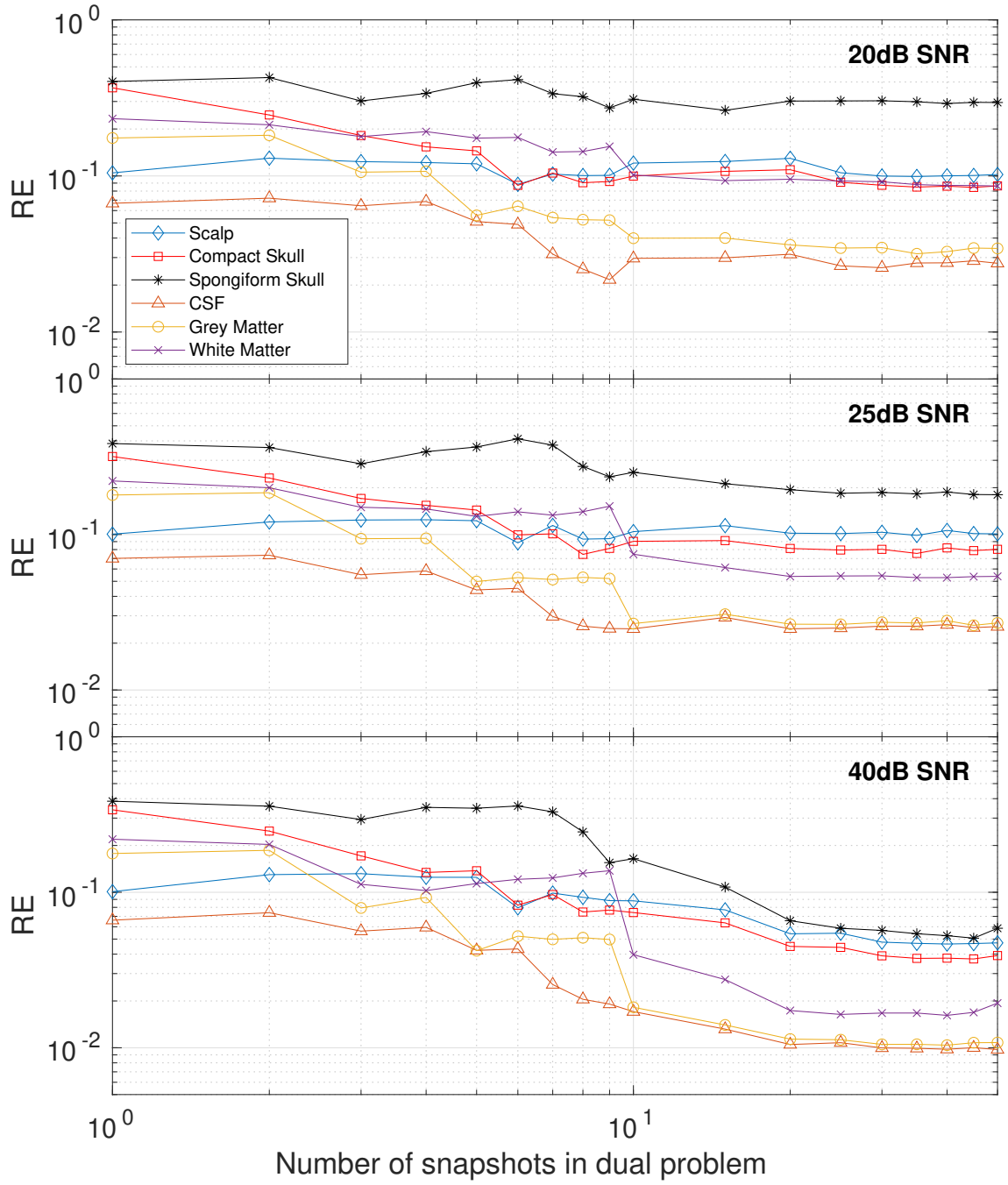

Fig. 6.4 Average RE in each tissue conductivity estimation using simultaneous reconstruction of SEP sources as a function of the number of snapshots used to train the dual problem (ROM-pEIT). Results are displayed for varying numbers of SNRs (20dB, 25dB and 40dB) in the synthetic SEP data. All tissue conductivities are freely estimated.

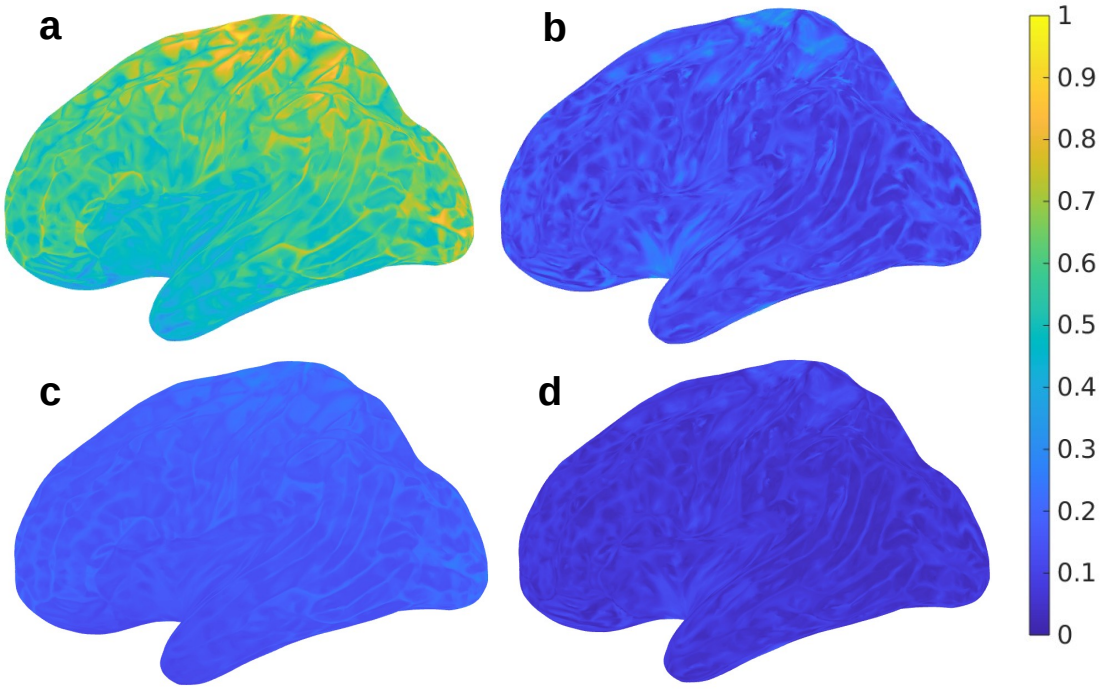

Fig. 6.5 Maximum (top) and average (bottom) RE in each source across 50 conductivity samples **a,c)** in the leadfield matrix made with the mid-point conductivities and **b,d)** in the leadfield matrix made with the estimated conductivities from the 25dB SNR signal.

6.5.2 Simultaneous Conductivity Estimations and Source Localisation

Fig. 6.4 shows the average RE for each tissue across 50 samples in the estimates obtained using the SEP data with simultaneous source reconstruction. These values are plotted as functions of the number of snapshots used in the dual problem (ROM-pEIT). This is shown for different amounts of noise in the SEP data, where the SEP signals had SNR values of 40 dB, 25 dB and 20 dB. It can be seen that in all noise cases there is an improvement in the GM and CSF as the snapshots increase. For the 40 dB case there is a decrease in the RE for every tissue as the snapshots increase. However, for the 20 dB case there is a flat response for the spongiform bone and scalp, which coincides with no improvement in the estimation of the spongiform bone or scalp over the standard literature values.

The reconstruction of both sources was exact for every conductivity sample and SNR. Each optimisation took roughly 5 minutes on a single CPU core, where the number of function evaluations in the optimisation affected the overall time. The maximum function evaluations for the optimisation was set to 3000, however, we found no improvement in the estimations with a higher value.

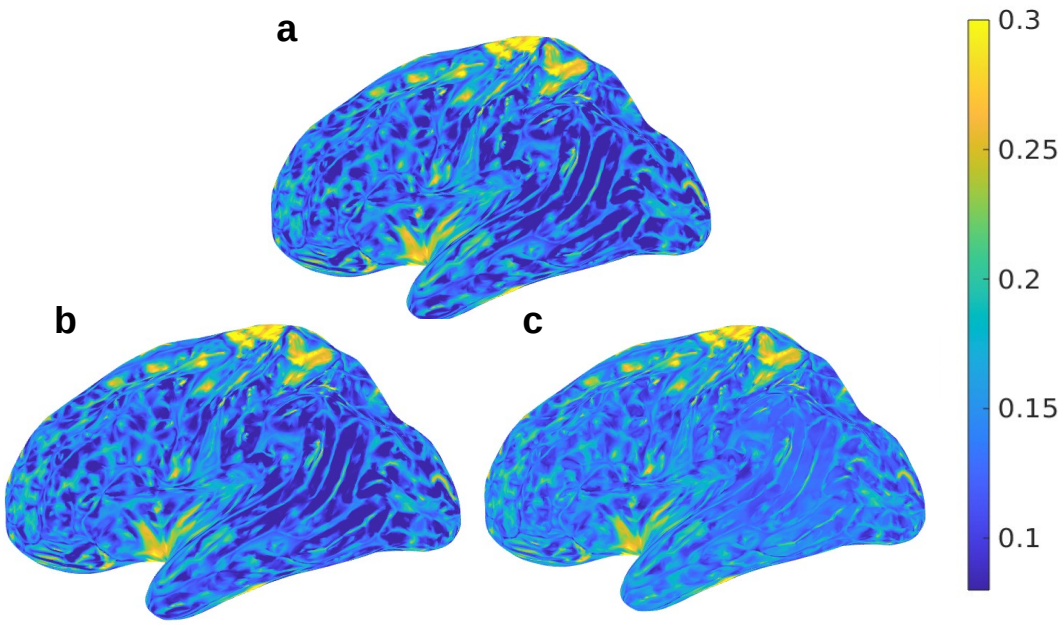

Fig. 6.6 Maximum RE in each source across 50 conductivity samples in the leadfield matrix made with the estimated conductivities from the **a)** 40 dB, **b)** 25 dB and **c)** 20 dB SNR signals.

In Fig. 6.5 a comparison is displayed in the RE in the EEG-FP for each source in the source space between FPs solved with the mid-point conductivities and solutions with the estimated conductivities from the 25 dB SNR SEP signals. Clearly, there is a substantial reduction in the RE in the EEG-FP when the calibrated conductivities are used over the standard literature values.

Shown in Fig. 6.6, is a comparison in the RE in the EEG-FP between the estimated conductivities of different SNRs in the SEP data. There is very little difference between the 3 plots, suggesting that even noisy data can be used to extract a calibrated conductivity set that improves the EEG-FP. This becomes even clearer when compared with Fig. 6.5.

Fig. 6.7 plots the source localisation error for each source in the source space when the leadfield matrix used in the sLORETA algorithm is made with the mid-point conductivities and the estimated conductivities (25 dB SNR). From this plot, there is a clear improvement across the entire cortex in source localisation when the conductivity is calibrated with the SEP optimisation we present.

The plots in Fig. 6.8 are similar to the plots in Fig. 6.4, however, they represent the scenario where the three tissue conductivities are known (WM, CSF and spongiform bone). There is a clear improvement in the estimation of the scalp, skull and grey matter for all SNRs. The improvement in the scalp conductivity estimation for the 20 dB SNR SEP data is

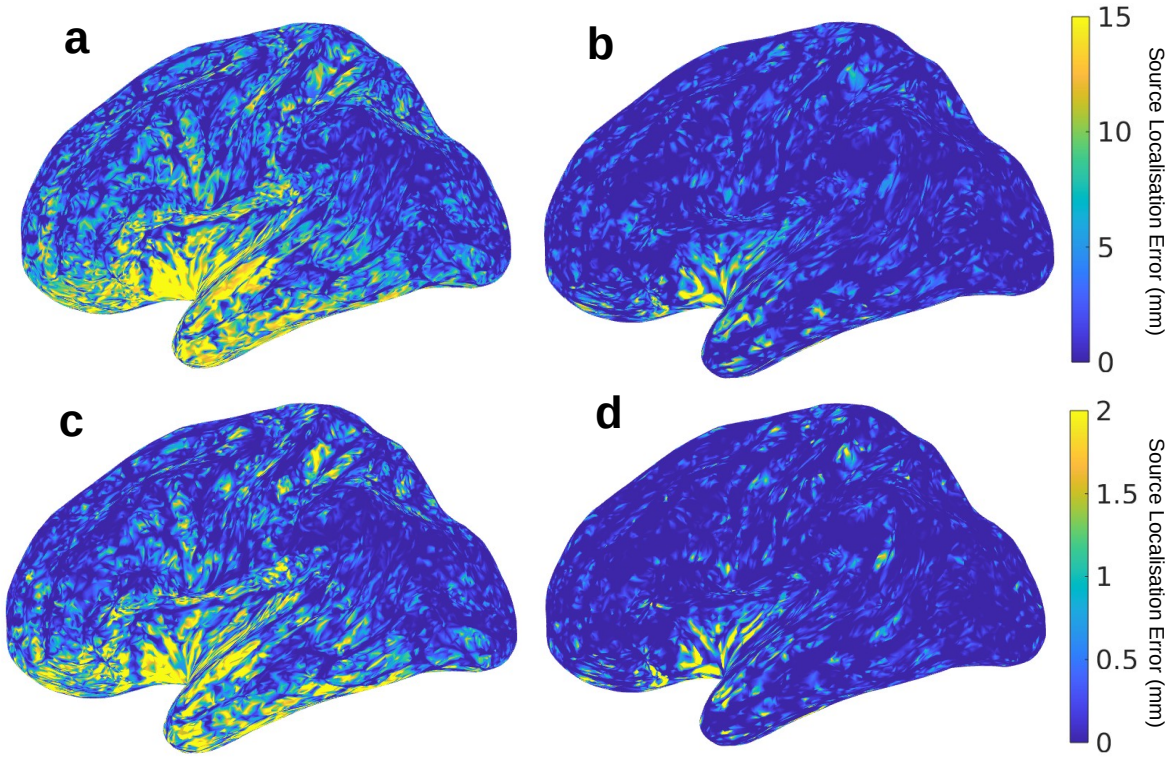

Fig. 6.7 Maximum (top) and average (bottom) localisation error in millimeters for each source across the conductivity samples when using the sLORETA algorithm with the leadfield matrices made with the **a,c)** mid-point conductivities and **b,d)** estimated conductivities (25 dB SNR).

particularly noticeable. Again, the source reconstructions of the radial and tangential sources were exact in all cases.

The total time required to compute $\mathscr{V}_{lj}^{CEM}$, $\mathscr{V}_{ljp}^{v}$ and $\mathscr{V}_{lj}^{s}$ for 29018 sources, 150 snapshots and 5 tissue compartments was approximately 11 hours parallelised on the 11 nodes mentioned in the Setup and Implementation Section.

6.5.3 Simultaneous EIT and EEG Conductivity Estimation

Finally, Fig. 6.9 shows the RE in the estimations of the tissue conductivities from the combined pEIT-based and SEP-based estimations (described in Section 6.4.4) as a function of the snapshots used to train the dual problem. The results are again split by the SNR of the SEP signal used in the optimisation.

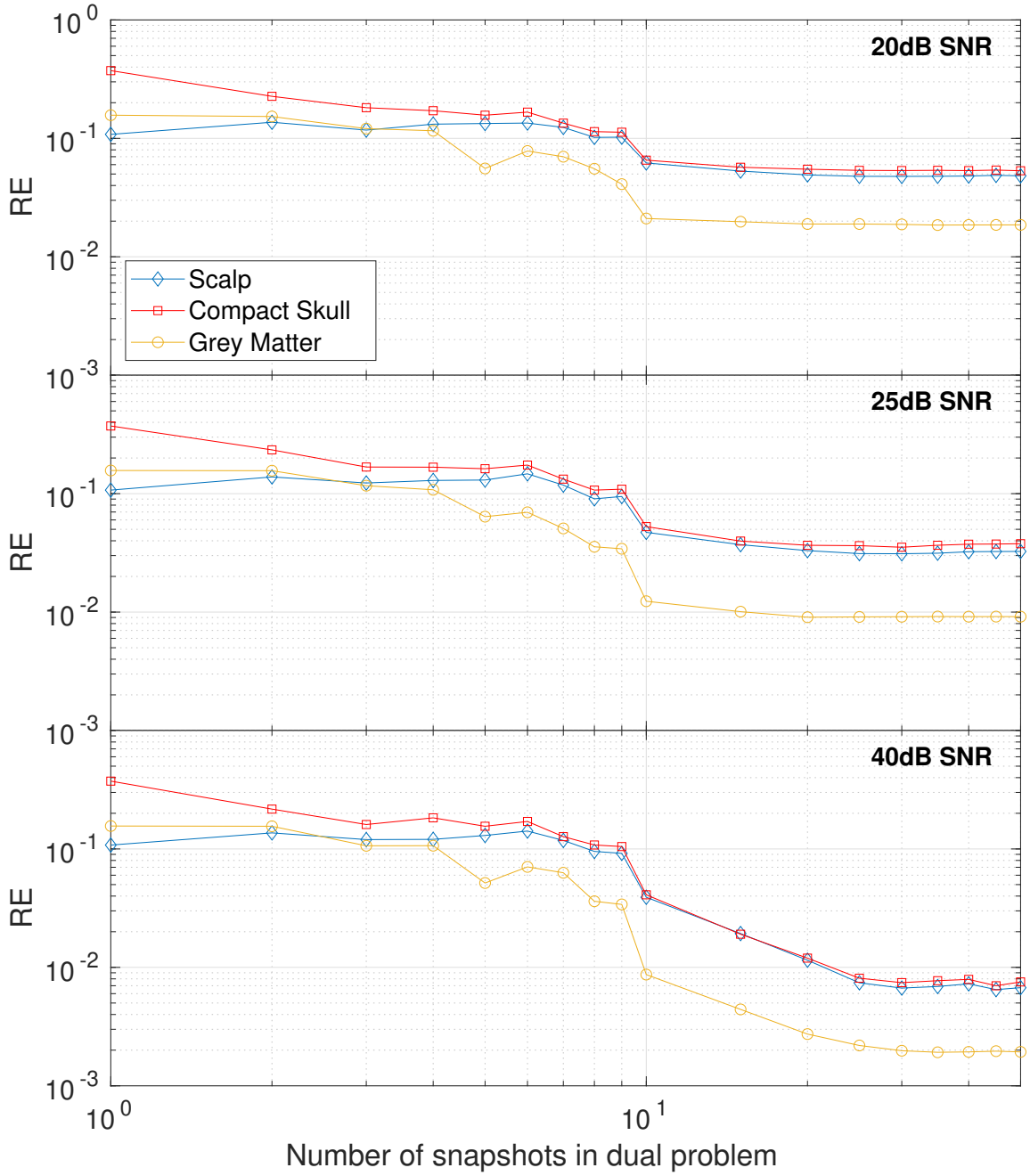

Fig. 6.8 Average RE in each tissue conductivity estimation using simultaneous reconstruction of SEP sources as a function of the number of snapshots used to train the dual problem (ROM-pEIT). Results are displayed for varying numbers of SNRs (20dB, 25dB and 40dB) in the synthetic SEP data. Here, the conductivities of WM, CSF and spongiform bone are fixed to their known values, with 3 conductivities (scalp, compact bone and GM) freely estimated.

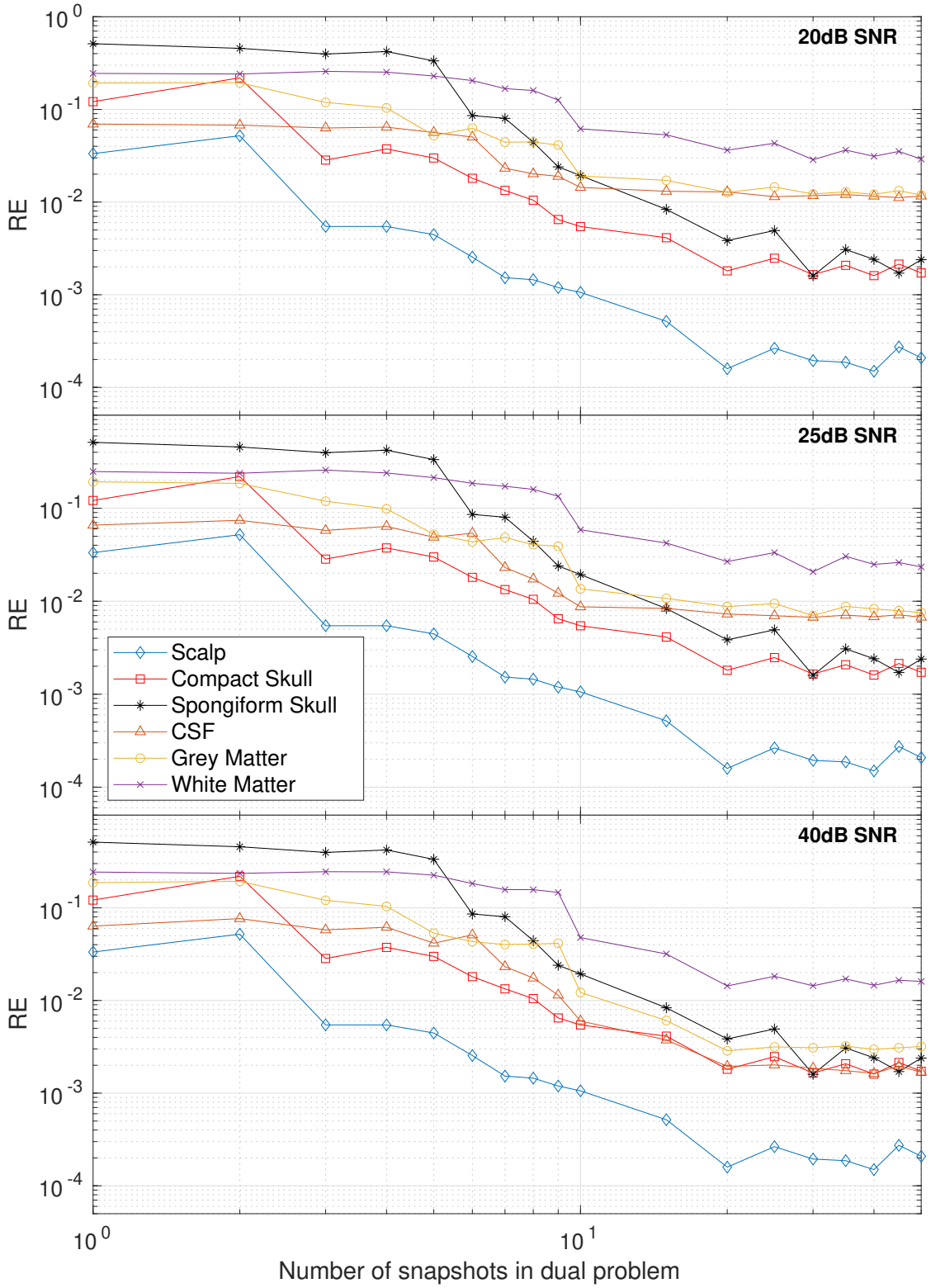

Fig. 6.9 Average RE in tissue conductivity estimations across 50 conductivity samples utilising the combined ROM-pEIT-SEP based method of optimisation, as a function of snapshots used for ROM-pEIT. Each plot represents a different SNR of the SEP signal used.

6.6 Discussion

In this chapter, we have presented a framework for the use of ROM-pEIT as the dual problem in the EEG-FP to rapidly generate leadfield matrices for any conductivity set. Consequently, this allowed us to implement a fast optimisation method for the simultaneous reconstruction of SEP dipole sources and multiple head tissue conductivities. The resulting calibration of these head tissues has led to significantly lower REs in the FP and lower localisation errors in the IP.

Firstly, we confirmed that the reduced version of the EEG-FP (ROM-EEG) was a suitable replacement for the full-order equivalent by comparing the potentials for 1000 dipoles in the leadfield matrix. Fig. 6.2 indicates that the difference between these techniques tends to zero as the number of snapshots used to train the dual problem increases. After 100 snapshots, this figure shows that the maximum error in the ROM-EEG-FP is below 10^{-4}, which is negligible in comparison to the numerical errors in the EEG-FP [24]. Furthermore, Fig. 6.2 shows that the relative error bound in the dual problem (ROM-pEIT) could serve as a practical bound for the relative error in the ROM-EEG-FP.

We then validated the simultaneous optimisation technique in a realistic 6-layered head model using synthetically generated SEP data. Fig. 6.4 shows that for high SNR values in the SEP signals, all modelled tissue conductivities can be estimated well with only 30 snapshots needed to train the dual problem. For lower SNR values, some tissues are no longer estimated well but the GM and CSF still remain well characterised (at least down to 20 dB). Importantly, Figs. 6.5, 6.6 and 6.7 show that, for 25 dB SNR, a substantial improvement can be obtained in the EEG-FP and EEG-IP for almost any source in the cortex when utilising the calibrated conductivity set.

Additionally, the results for estimating all tissues suggested that the complexity of the solution manifold in the 6-dimensional parameter space, could be the main limiting factor for further reductions in the RE of the conductivity estimations. We removed 3 of the dimensions from the estimation and found an improvement in the RE of the estimations for the remaining tissues as shown in Fig. 6.8. This shows the benefit of having some *a priori* information about the conductivities from a technique such as pEIT.

Lastly, combining the strengths of both ROM-pEIT and ROM-EEG, we can obtain an accurate characterisation from all tissues in the head model when using high SNR SEP data. From Fig. 6.9 it is clear that for high SNR values, the estimations are better than either technique alone. For low SNR values, the estimation clearly tends to the values obtained by ROM-pEIT, with diminishing contribution from the SEP part of the optimisation. This is a strong advocation for the pEIT method itself as a tool for conductivity characterisation.

However, given both of these techniques require the same hardware as EEG (with minor alterations for pEIT), and can be performed in a reasonable time frame.

For all of the above experiments, loading the stored values $\mathscr{V}_{lj}^{CEM}$, $\mathscr{V}_{ljp}^{v}$ and $\mathscr{V}_{lj}^{s}$ for $l = 1, ..., L-1$, $j = 1, ..., n_s$ and $p = 1, ..., 5$, required 80 GB of RAM. Even though only a single CPU was needed to operate on the values, the large amount of RAM is of course much higher than for a standard PC. However, for these experiments, the full 150 snapshots in the dual problem were loaded. As seen in Figs. 6.4 and 6.8, 30 snapshots in the dual problem is more than sufficient, and further snapshots did not provide any improvements in estimation accuracy. Therefore, the stored values could easily be cut down to 30 snapshots to reflect this and require only 16 GB of RAM, which is much closer to standard RAM provisions. The same improvement would be found for the pre-computation stage, where reducing the size of matrix $\mathbb{V}$ could improve the RAM and computational requirements significantly.

A further improvement could even be found by cutting the source space down to only sources in the postcentral gyrus, central sulcus and postcentral gyrus (a reasonable assumption to make about the origin of SEP signals). This would shrink the source space to 1831 sources in our case and not only reduce the RAM required but speed up the estimations. We found this led to an 8-fold increase in the speed of the optimisation.

Of the time taken to precompute $\mathscr{V}_{lj}^{CEM}$, $\mathscr{V}_{ljp}^{v}$ and $\mathscr{V}_{lj}^{s}$ for $l = 1, ..., L-1$, $j = 1, ..., n_s$ and $p = 1, ..., 5$, the vast majority was to calculate the source vectors of the subtraction approach. These then had to be held in memory as non-sparse vectors. This has considerable memory and computational demands. By exploring other source vector representations that have far smaller RAM and computational requirements (such as St Venants approach), this process could be made considerably faster. Given that the construction of the source vector can be arbitrarily changed, this could be left to the user of the framework to decide. However, it should be noted that the use of source vector representations other than the subtraction approach will introduce theoretical issues due to a lack of existence and uniqueness in the solution, and it is unclear how the framework would behave in this scenario [75].

Previous approaches to minimising the computational burden of generating leadfield matrices include the use of a transfer matrix (see Chapter 3, Section 3.3.1). This method reduces the number of large systems to solve down to the number of electrodes minus one. However, this is only applicable to a previously defined conductivity set. Building the reduced models is computationally more expensive than a single transfer matrix, but results in the significant advantage of generating a leadfield matrix for any conductivity set afterwards. Subsequently, this leads to the ability to estimate conductivities very quickly, which would not be possible with the transfer matrix approach.

6.6.1 Related Work

The most closely related work to ours is by Maksymenko et al. (2020), where a similar dimensionality reduction technique is employed to approximate leadfield matrices [111]. This approximation is then used to obtain tissue conductivities for unspecified simulated EEG data and real SEP data, with only 10 snapshots (called *support points* in their work) needed. Our technique differs in a number of ways. The first is in the implementation. We demonstrated our method in a realistic FE head model with 6 tissue compartments whereas, Maksymenko et al. (2020) use only a 3-layered boundary element (BE) method head model, reducing the computational complexity significantly. Secondly, their method is only shown to estimate 3 tissue conductivities (brain, scalp and skull) in the synthetic data and 2 (brain and skull) in the real SEP data, while we consider 6 conductivities (massively increasing the size of the conductivity space). Thirdly, the error bound they present, although rigorously derived, does not appear to bound the real error (see Fig. 3a in Maksymenko et al. (2020)). We present a rigorous error bound in the dual problem (pEIT-FP), that is not only certified in bounding the real error, but appears to be a good approximation of the error in the EEG-FP.

Another relevant piece of work by Lew et al. (2009) describes the use of Low-Resolution Conductivity Estimation (LRCE) that uses simulated annealing (SA) to minimise a cost function with the aim of simultaneously tangential and radial dipoles from simulated and real SEP data [108]. Their method discretises the conductivity space and then utilises the transfer matrix approach to generate full-order leadfield matrices for multiple combinations of conductivities and sources. For high SNRs this work achieved low source localisation errors and accurate conductivity estimations in the synthetic data, however the technique struggled with SNRs around 20 dB. Our method stands apart from this in a few ways. Firstly, the computational cost of the optimisation step was much higher, where the SA took 17 hours in one case. Our optimisation step takes only a handful of minutes. The precompute time for their method was much lower, however, they utilised a much coarser head model and used the St. Venants approach in the source vector. Secondly, we implement the CEM in our experiments, as opposed to the PEM in Lew et al. (2009). Thirdly, due to the number of full-order leadfield matrices needing to be generated being proportional to the conductivity space and its discretisation, they only estimated the brain and skull conductivities. For our technique, once the dual problem is trained, the leadfield matrix can be calculated for any point in a continuous n-dimensional conductivity space where n is arbitrary. Therefore, for high SNRs, we were able to estimate all tissue conductivities accurately.

Another popular approach is the use of SEP and SEF data to calibrate the skull conductivity [79, 93, 16, 108, 10, 198, 157, 70, 23]. The main principle here is to combine the advantages of both techniques and reduce the disadvantages of each. Specifically, MEG is

better at localisation of tangentially oriented sources with little known information on the conductivity and EEG is sensitive to the conductivity field and radial sources. Therefore, the MEG-SEF data can be used to localise and fix the source in place while the EEG-SEP data is used to find the orientation and magnitude of the source and estimate the skull conductivity. A crucial distinction between this popular approach and our technique is the necessity for MEG. Our approach allows for the characterisation of many tissues while reconstructing the source with high accuracy without the need for SEF data. This is an important aspect, given the availability of MEG and cost of owning and operating MEG systems. Furthermore, most studies cited only tune the skull conductivity, while our approach attempts to reconstruct all tissues in the head model. On the other hand, a strength of these works in comparison to this one is the reconstruction of the orientation and magnitude of the sources. Investigating the impact of incorporating this additional calibration will be considered future work.

Three other closely related pieces of work are that of Gutierrez et al. (2004), Vallaghe et al. (2007) and Costa et al. (2017) [80, 173, 46]. All of these works use EEG data only to estimate tissue conductivities in a head model. In the case of the former, they assume a known dipole source and their technique could not be applied to realistic head models. Vallaghe et al. (2007) implements an optimisation that searches to minimise a cost function connecting the conductivities and source location with the measured signal. However, they use a 3-layered BEM model with approx. 800 vertices for each of the 3 surfaces and only 4000 possible source positions on the cortical surface. This dramatically reduces the complexity of the problem, allowing the EEG-FP to be computed very quickly but suffers from a lack of anatomical accuracy compared to a highly refined model with more compartments. In the latter, Bayesian methods are also employed with Markov Chain Monte Carlo (MCMC) based optimisation, utilising a polynomial matrix to approximate the leadfield matrix and aid sampling in the MCMC. The polynomial matrix is built using the full-order leadfield matrices as support points. This method showed an improvement over the previous methods from Gutierrez et al. (2004) and Vallaghe et al. (2007) and demonstrated their technique with real Auditory Evoked Potentials (AEP) data. However, the polynomial matrix still required 10 support points for one tissue (skull), which are chosen linearly across the conductivity space. We utilised a greedy algorithm in the dual problem that selects the support points (snapshots) in a robust way, that only requires 30 in order to characterise a 6-dimensional conductivity space.

Finally, work by Akalin Acar et al. (2016) used sensitivity matrices to reduce the number of full leadfield matrices needing to be calculated and therefore calibrate the the brain to skull conductivity ratio (BSCR), in an EEG data set. While this technique appeared to work well, it was only shown for a low resolution FEM mesh (240,000 nodes) and estimating one

conductivity ratio, and in this scenario took up to 4.6 days to converge on a single workstation. Our method is shown to calibrate 6 tissues, in a highly refined, realistic head model (830,000 nodes).

6.6.2 Future Work

During the experimental process it was noticed that, when running the first simultaneous estimation including all tissues in the case of a noiseless SEP signal, with a dual problem trained with 150 snapshots, yielded no better results than with a signal with an SNR of 40 dB result at 30 snapshots. One possible explanation for this is the solution manifold in a 6-dimensional parameter space being very complex, with many local minima. This was the motivation for the reduced compartment number experiment (as previously mentioned). Many local minima that trap the optimisation procedure could be responsible for limiting the estimation accuracy of many tissues. This makes intuitive sense given that multiple combinations of conductivities can explain the same EEG data. An example of this is given in Fig. 6.10, where the RE in the FP for a tangential source is plotted as a function of the conductivity in the scalp and the GM. From this figure it can be seen clearly that there are many possible combinations that could explain the data almost perfectly (indicated by the red dotted line). Here, the RE is between a FP made with known conductivities (black dot) and an FP made with varying conductivities.

Future work would focus on exploring ways to navigate the conductivity space better in the sense of finding the global minima more reliably. Changing the optimisation method could be one way to compensate for many local minima. For example, particle swarm approaches have been known to help with poorly determined problems with smooth valley solution manifolds and have recently been used in EIT imaging for stroke detection [110]. Other methods like SA have been used by others for similar problems [169, 108]. Similarly, tuning the hyperparameters of the dual problem (e.g. the bound sample train) may yield some benefit (see previous chapter).

Another avenue for further research would be to investigate the impact of setup changes on the estimations (e.g., number of electrodes and position of reference electrode). Furthermore, testing the effect of missing tissue information (similarly to the last chapter with pEIT) should be essential work for the future. From the previous chapter, the impact of a missing tissue compartment on forward and inverse solutions to the pEIT problem is large. Coupled with the findings from real pEIT data which suggest that a modelling inaccuracy is present, this impact is even more topical. This could prove especially important in EEG given the source of current is separated by several compartments from the measurement electrodes (conversely to pEIT). On this note, if additional compartments (e.g., a layer of fat) were to be

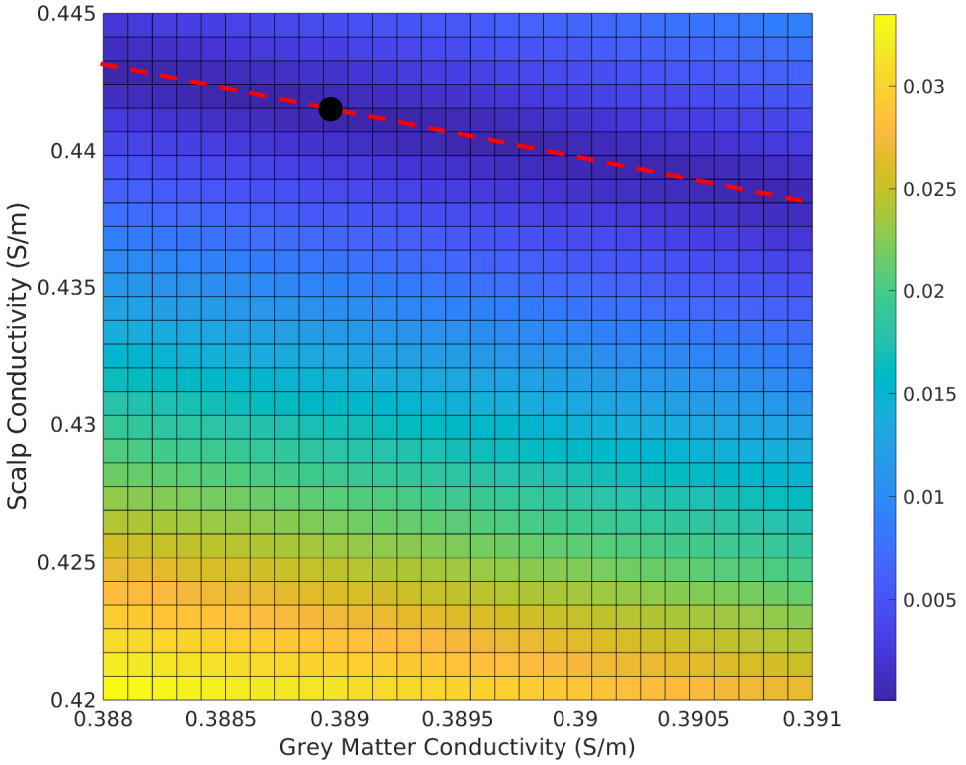

Fig. 6.10 RE (colourbar) in the FP of a tangential dipole source between one with known conductivity (black dot) and varying GM and scalp conductivities plotted as the function of the conductivities. The red dotted line indicates combinations of conductivities that produce extremely similar FP solutions.

included in the head model, this would increase the dimensions of the conductivity space and therefore accentuate the problems mentioned in the previous paragraph. The likelihood of a large modelling error could also potentially limit meaningful tests on real EEG data.

This study focuses on the reconstruction of a tangential and radial dipole source that could be likely generators of the SEP P20/N20 and P22/N22 components respectively. However, in principle this estimation procedure should be possible with a range of potential readings from dipole source generators. For example, AEP, laser evoked potential (LEP) and visual evoked potentials (VEP) data could all be used provided the SNR in the data is relatively high. Even within the SEP response data, there are multiple other components that could be explored (e.g., P35/N35), both in the short-latency and long-latency classes. Additionally, depending on the data used, there could be an impact due to the depth of the source being reconstructed.

The dual problem was trained in the conductivity ranges that were reported to explain most of the variance in individual conductivities [116]. This range could be arbitrarily

expanded however, to capture a wider conductivity space. This would likely require more snapshots to be used in the dual problem, but would provide even greater improvements in source localisation error if the same experiments were run again.

The approach we present has enabled the individual characterisation of multiple tissue conductivities with a simultaneous source localisation from EEG-SEP data. This represents a crucial step towards fully personalised head models that are essential for ESI techniques. The savings in the FP and IP we demonstrate suggest the power this technique has to transform the accuracy of EEG.

6.7 Summary

In this chapter, have presented a framework for integrating the ROM-pEIT technique developed in previous chapters into the EEG-FP via a primal-dual splitting of the problem. We showed that this new framework allowed the generation of fast leadfield matrices for any conductivity set. Consequently, we are able to employ simple optimisation methods to tune a set of conductivities and therefore lower the forward and inverse errors for EEG. The main conclusions of this chapter are as follows:

- The adjoint problem for the EEG-FP is the pEIT-FP. Therefore, we were able to simply substitute the pEIT-FP for the ROM-pEIT developed in previous chapters. This allowed us to develop a framework for the rapid generation of an EEG-FP via a set of ROM-pEIT, for any conductivity set. Further, we can now generate entire leadfield matrices seconds, opening up new possibilities for experimentation.

- With the ability to make almost instant leadfield matrices, we were able to tune the conductivity set until it matches an EEG-FP solution. Additionally, we could add in the localisation of the source of the EEG-FP to simultaneously reconstruct both of these parameters.

- We show that the ability to simultaneously localise the source of EEG data and the conductivities of the tissue of the head can be achieved with the well characterised SEP components P20/N20 and P22/N22. Although in principle this could be achieved with any EEG data.

- The reconstruction of the sources is exact in all cases, even for signals with SNR values of 20 dB. Furthermore, the accuracy in the FP and IP for the entire cortex is substantially improved when using the tuned conductivity set as apposed to the standard literature values.

- Many other methods proposed in the literature that have similar aims only consider the one or two conductivities and/or use very course head models due to computational limits. The approach presented in this work considers many tissue conductivities in a refined realistic head model. The other main advantage to our method is that there is no need for MEG data.
- This method also highlighted the complexity of the solution space for the EEG-FP when multiple conductivity dimensions are considered, showing that simple optimisation methods are prone to falling into local minima.
- Finally, this framework is flexible enough to allow pEIT and EEG to be used in conjunction with one another to provide highly accurate conductivity estimates for every tissue. This highlights the need for pEIT to become a standard procedure for ESI.

Chapter 7

Conclusions and Future Directions

7.1 Thesis Overview

Characterising the electrical activity in the brain is essential to our understanding of its function. To study this activity we use EEG, where electrical potential readings are taken on the scalp to infer the sources of current. This inference comes with a computational cost, that rises with the inclusion of more detailed anatomical information in the head models constructed for EEG. Additionally, including information about the conductivity profile of each biological tissue in EEG can be achieved with pEIT, however, this is also computationally intensive. The cost of both methods can be prohibitive in some cases, especially when trying to include personalised conductivity parameters. This results in compromises such as standard literature-based conductivity values being assigned to head models. The computational expense of these methods is therefore a barrier to widespread personalisation of EEG methods.

This thesis has proposed the use of ROM to alleviate the computational demand of pEIT and EEG. Effectively, ROM is able to formulate, after some training, a reduced EEG-FP and pEIT-FP, that can be evaluated for any conductivity set in real-time. As a result, both techniques can be used for the estimation of head tissue conductivities assigned to personalised head models, with varying sensitivities to different tissues.

7.2 Contributions and Findings

In Chapter 4, the application of ROM to the pEIT-FP was demonstrated in a realistic 6-compartment head model with 132 electrodes modelled on the scalp. The relative error bound for ROM in the FP was verified by comparing 100 full-order numerical solutions with

the reduced solutions. Simultaneously, it was shown that the problem is reducible and we found that after 30 snapshots, the average RE for between the forward solutions was below 10^{-5}. This showed that with only 30 snapshots, a highly accurate map between conductivity changes in the parameters space $\mathscr{P}$ and the FP solution was found. Although it was noted that this may change, subject to other parameters in the FP.

Chapter 5 focused on the applications of the ROM-pEIT framework. Primarily, this chapter assessed the inverse performance using the metric of RE in the tissue conductivity estimation for each tissue. This metric was assessed in a number of scenarios. Firstly, the use of ROM-pEIT was compared to the previous state-of-the-art method which used a gradient-assisted Newton's optimisation method in the inverse problem. The ROM-pEIT framework utilised the interior-point optimisation due to being unable to calculate a gradient. A comparison of the REs obtained against the computational force needed between each method was performed. It was found that not only does ROM-pEIT speedup the time to estimations by orders of magnitude, but additionally, this now makes it feasible to estimate more tissues than previously possible. Secondly, a thorough sensitivity analysis was performed, demonstrating the robustness of the new framework (including ROM-pEIT-FPs and the interior-point optimisation) to noise, tissue compartments with anisotropic conductivities and varying snapshot numbers. 30 snapshots appears sufficient for the accurate estimation of many tissue with more snapshots adding no improvement. This observations appears to hold for anisotropic compartments and for varying levels of noise. Thirdly, the use of novel injection and measurement patterns was explored, with noticeable improvements in the conductivity estimation of many of the inner tissue compartments. This experiment hinted at the complexity of the solution space, and the possible manipulation of pEIT protocols to help navigate it.

The placement of the reference electrode in the case of missing tissue information was tested, showing that the large standard deviations between electrode pair estimations are possible when the reference is chosen poorly and the information is missing from the model. Furthermore, this aided the explanation of the results from real data, which showed large standard deviations and strongly suggested a missing tissue layer in the head model. Given that our head model had most tissues considered in modern literature, this indicates that a common modelling assumption could be erroneous. This is a significant finding, that can only be made now that ROM-pEIT has removed the computational barrier.

In the final experimental chapter, the use of the ROM-pEIT-FP as the dual problem to the EEG-FP was demonstrated in a realistic head model with 165 electrodes and 6 tissue compartments. This enabled the new capability to make extremely fast leadfield matrices (of the order of 3 seconds) for any set of conductivity parameters. Ultimately, this enabled

the simultaneous reconstruction of conductivities and current sources using synthetically generated SEP components. Even with noisy EEG data with SNRs down to 20 dB, the additional conductivity calibration afforded by the fast leadfield matrices resulted in a zero error localisation for the SEP component generators. Consequently, a reduced source localisation error across the whole cortex was found using the calibrated conductivities.

The complexity in the solution space were again noted as a limiting factor for the accuracy of conductivity estimation in ROM-EEG, similarly to ROM-pEIT. Therefore, the two techniques were merged in Chapter 6 to navigate the solution space more effectively. Given that each technique is sensitive to different tissues, the combination has shown improvement in estimation accuracy over any one technique alone for SNRs in the EEG data around 40 dB.

Fundamentally, the application of ROM allows for exhaustive optimisation methods to be used, which, aside from providing new tissues to be estimated, practically means that the accuracy tissue conductivity estimations can be improved. Table 7.1 shows a comparison of the accuracy of the conductivity estimations resulting from all the methods presented in this thesis and, as such, provides a summary of the work. The values in the table are the RE of the estimations with their standard deviations across a range of conductivity samples. Included in this table are the RE values for the traditional method as a display of the starting point of this thesis. From here, it is clear that the application of ROM to pEIT leads to a substantial increase in the RE for the tissues of scalp, compact bone and spongiform bone while enabling the capability of estimating CSF, GM and WM. This comparison even gives the traditional method the advantage of knowing the exact inner tissue conductivities (which may not be realistic). Furthermore, the addition of a staged optimisation utilising a new pEIT protocol and an EEG-based optimisation utilising SEP data has shown that sensitivities to different tissues change as the source(s) of current change. This was exploited by combining pEIT and EEG data in a single optimisation process, utilising both ROM-pEIT and ROM-EEG frameworks to achieve accurate electrical conductivity estimations in all tissues. This final result represents the potential for a large shift in the field, allowing for a comprehensive and holistic characterisation of conductivity field in head models used for ESI.

Method	Scalp ($\times 10^{-4}$)	Compact bone ($\times 10^{-4}$)	Spongiform bone ($\times 10^{-4}$)	CSF ($\times 10^{-4}$)	GM ($\times 10^{-4}$)	WM ($\times 10^{-4}$)
Traditional pEIT	23 ± 32	64 ± 61	1037 ± 824	N/A	N/A	N/A
ROM-pEIT	3.18 ± 3.51	22 ± 21	168 ± 215	283 ± 235	395 ± 311	671 ± 543
ROM-pEIT (staged)	1.99 ± 4.08	19 ± 29	17 ± 31	238 ± 226	240 ± 264	167 ± 350
ROM-EEG (25 dB)	1034 ± 876	803 ± 699	1864 ± 1520	257 ± 222	273 ± 248	542 ± 563
ROM-EEG (40 dB)	377 ± 478	327 ± 390	437 ± 568	68 ± 100	80 ± 105	155 ± 167
ROM-pEIT/EEG (staged - 25 dB)	1.94 ± 4.07	16 ± 29	16 ± 31	67 ± 46	70 ± 47	207 ± 206
ROM-pEIT/EEG (staged - 40 dB)	1.94 ± 4.07	16 ± 29	16 ± 31	19 ± 15	31 ± 26	144 ± 125

Table 7.1 Mean and standard deviation of RE of conductivity estimations for all tissues for each estimation method presented in this thesis. The first and second rows are the traditional pEIT and ROM-pEIT method presented in Section 5.3.2, where the values were computed with 10 and 100 conductivity samples respectively. The third row represents the staged ROM-pEIT optimisation method using a new protocol described in Section 5.3.5, utilising 50 conductivity samples. Rows four and five represent the simultaneous source localisation and conductivity estimation using ROM-EEG and SEP data, described in Section 6.4.3, where the data had SNRs of 25 dB and 40 dB, respectively. Finally, rows six and seven represent the combination of the staged ROM-pEIT and ROM-EEG with SEP data as described in Section 6.4.4, where the SEP data had SNRs of 25 dB and 40 dB respectively. Rows four to seven had mean and standard deviations in the RE calculated over 50 conductivity samples. For each method using ROM, the models were trained with 30 snapshots.

7.3 Limitations

One of the limitations of this work has been the use of the same mesh when generating the reduced models and the synthetic measurements. This could be considered to be the so-called *inverse crime*, whereby the measurements are favorably generated towards the forward problems and therefore bias the results, even in the presence of noise. Similarly, in the EEG work, the source localisation used a source space where the measurements were made with dipoles in the positions on the same source space. To further test the robustness of the methods presented in this thesis, future work would include the use of alternative meshes and source spaces to generate the synthetic measurements, with the possibility of adding Gaussian noise to the source space directly. Furthermore, for the SEP measurements, single dipoles were used to generate the synthetic data. It may be more realistic to define a patch on the cortex that generates the signal when creating the measurements. The use of sLORETA would still be justified in this case as it is a distributed source inverse algorithm. Investigating this could be work for the future.

To create noisy synthetic pEIT and EEG measurements, noise was added to full-order FP simulations. In this synthetic data, we assumed a Gaussian noise model as this is typically used to model noise in EEG recordings [192]. modelling more complex noise, such as spatially and temporally correlated background noise, could be considered in future [30]. However, due to the high SNR of pEIT signals, this is expected to make negligible difference. In EEG data, however, where the SNR is much lower, future work would include modelling more complex noise sources.

Similarly, the results shown in Fig. 6.7 include the source localisation across the whole cortex with no noise in the synthetic measurements. Noise was not included to demonstrate the potential maximum benefits of having tuned conductivities (found using noisy SEP measurements) over population average ones. In future work, adding noise to these measurements would highlight whether these benefits would still be visible.

Uptake of pEIT in clinical practice could also be a limitation. To the best of our knowledge, no commercial high-density pEIT system exist and previous datasets have been obtained with *ad hoc* setups [169]. This could prevent the adoption of pEIT. The SEP-based tuning could be more easily integrated into clinical pipelines, however, given that that the methods of collection of evoked potentials data is already well established in the community, more so than pEIT. For pEIT to be adopted more readily, standardised equipment and training in its use should be developed, along with attitudes towards the method in the field changing. Furthermore, the frameworks presented here show that they stumble when modelling inaccu-

racies exist. This suggests that much more work is needed into the modelling assumptions made in the field before widespread clinical adoption is considered.

Table 4.1 shows the ranges of conductivities used to the train the reduced models. While these ranges represent the spread of the conductivities within the population according to McCann et al. (2019), some ranges have a wide relative spread compared to others. For example, maximum value of the spongiform bone is 88 times the minimum, whereas, the CSF maximum is only 1.3 times the minimum. The small relative range in the CSF could make it a good candidate for assuming the value as a population average to remove a dimension in the estimation process (as highlighted to be beneficial in previous chapters. Conversely, the large ratio in the spongiform bone could be responsible for more snapshots being needed and would therefore benefit from narrowing the range down to be as narrow as possible. Similarly, the ratio in the compact bone of the skull is 16.4. Given that the skull is highly influential in EEG (see Vorwerk et al. (2024) [187]), reducing the relative size of the range could lead to lower snapshot numbers. These ranges could potentially be reduced by further distinguishing constituent tissues (e.g., skull sutures or bone plates).

To solve the large full-order systems in this work, we used an iterative PCG method with incomplete LU preconditioners. Other methods could be considered for faster solutions, such as multigrid or incomplete Cholesky preconditioners, as well as GPU implementations [59, 33, 90]. Other improvements could include the use of block conjugate gradient methods for solving multiple systems with the same stiffness matrix but different right-hand side vectors [124]. This could lead to a significant speed up with the possibility to reduce the workload by sharing the effort for each snapshot between the reduced models. However, all these variations would have a similar impact on both the traditional methods and the presented reduced methods, which is one of the reasons we chose the number of systems to solve as the metric for computational effort.

A limitation of the comparison between the traditional and presented ROM-pEIT method is the number of conductivity samples used when testing the traditional method. While the ten samples were taken randomly from a uniform distribution, this may not be enough to adequately represent the 3-dimensional conductivity space. This limitation was imposed by the computational expense of the traditional method. If this computational cost could be alleviated (e.g., with one of the methods above), or if more computational power were available, then a more thorough comparison could take place.

7.4 Future Directions

These latest capabilities of these methods has allowed new questions to be asked. This section will touch on some of the avenues of research that could be most fruitful.

7.4.1 modelling Assumptions

One of the biggest hurdles to overcome toward better EEG source localisation is inaccuracies in the head models utilised. These models typically contain some assumptions about the physical aspects of the head, (e.g., that the scalp is one single homogeneous layer with a single conductivity). These assumptions are usually made based on the imaging data and computational power available. However, as highlighted in Chapter 2, there is continuing debate over which layers are essential to characterise, and to what degree. For example, segmentation and inclusion of the CSF in head models has been shown to be important, however, it has been suggested that standard literature values are sufficient for the conductivity.

Verification of modelling assumptions is also a challenge. Mostly, studies with synthetic measurements are used to verify the impact of modelling variations in the forward and inverse problems. While this is effective for assessing the impact of individual compartments and properties, real data is needed to verify if the model is refined enough to explain the measurements.

In EEG, verification through real data is a challenge due to the multiple unknown quantities in the source of current itself (e.g., its strength, orientation, location and distribution). In pEIT, the source is exactly defined and therefore serves as a much better alternative for studying modelling assumptions. Previously, pEIT has been limited by computational constraints, preventing systemic analysis of every tissue layer and its contribution to current propagation in the head. However, with ROM-pEIT, it is now possible to perform these kinds of sensitivity studies, even in real data. Moreover, Chapter 5 showed the application of ROM-pEIT to real data and strongly suggested that there are modelling assumptions that need re-evaluating. Furthermore, the standard deviation in the estimations across injection pairs was shown to be a reasonable litmus test for missing tissue information.

Clearly, it has been heavily indicated that 6-compartment head models including the scalp, skull, spongiform bone, CSF, GM and WM are possibly not refined enough to explain real data. As highlighted in Chapter 2 and the Discussion of Chapter 5, the missing model information could be from a range of tissues (e.g., fat/adipose tissue, emissary veins, skull sutures and dura mater). A survey of these tissues with significant amounts of real data should be the primary direction of future research in this field. With both pEIT and SEP-EEG data from a large range of participants, using these new ROM-based tools could uncover vital information for the future of individual head model generation.

Within reason, the affine decomposition can be expanded such that any number of tissue compartments can be included in the head model. This opens up the possibility to partition tissues into subsections. For example, the skull can be partitioned into multiple

bone plates separated by sutures. In future work, the individual bone plate conductivity could be estimated.

7.4.2 Transcranial Direct Current Stimulation

A field closely related to EEG and pEIT is TDCS. This method aims to moderate the electrical activity in the brain and has shown promise as a treatment for many neurological conditions (e.g., depression [96]). Similarly to pEIT, this technique injects and extracts current from electrodes, however, with a motivation to optimally target a specific region of the brain, inducing high levels of current in that area. Consequently, the mathematical formulation for the TDCS-FP is identical to that of pEIT [134], and therefore relies on realistic head models. Naturally, it has been shown that TDCS is also impacted by the conductivities selected, where the focality and intensity of current at a region of interest (ROI) increases when modelling the exact conductivities [188, 114]. Further, varying configurations of injection patterns have been shown to impact localisation of current from TDCS, where multiple injection electrode montages are beneficial over typical pair montages [148]. Work has also been conducted to assess the best algorithms for finding optimal injection patterns to target a ROI [65, 62].

With ROM-pEIT, the computational splitting of work into offline and online phases means that the conducitivities could be estimated as soon as the measurements are taken, resulting in an immediate determination of the optimal injection pattern. Clinically speaking, pEIT could be easily added into a TDCS protocol to improve its effectiveness without requiring a separate visit by the patient.

7.4.3 Technical Refinement

With any machine learning method, the hyperparameters used to build a model can have a massive impact on the end result. This thesis did not cover any formal exploration of these parameters in ROM and instead relied on values found with trial and error on the basis that they were good enough to produce to the desired results. In future, there are some hyperparameters that could effect the reduced models are built and consequently the solution space. One example is the sample train used in the online evaluation of the bound (see Section 4.3.2). The number of samples of the conductivity parameter space $\mathscr{P}$ in the sample train was only 6000 in the online evaluation of the bound. Taking more samples would have represented the space better and potentially likely led to different snapshots being taken. Smarter sampling methods could also be explored, rather than random sampling, where more points are chosen where the solution manifold changes most rapidly. It is unclear how these

changes would affect the IP, however, some investigation is definitely warranted. Similarly, the number of stability factor interpolation points could be investigated.

One unexpected finding of this work is the complexity of solution manifold over the 6-dimensional parameter space. With noiseless synthetic data, it was expected that the ROM-pEIT-IP would tend towards perfect conductivity estimations with increasing snapshot number. However, it was noted in Chapter 5 that this was not the case. This situation repeated itself with the ROM-EEG conductivity estimations. One explanation for this is the optimisation algorithm could not find the global minimum in the solution manifold due to the complexity of the solution space. This confirms how ill-posed the problems are, with many local minima in the solution manifold. This problem could become even worse if additional tissue compartments are added to the model. This challenge could be tackled in a number of ways in future research. Firstly, alternative optimisation algorithms could be employed too search the space more effectively (e.g., simulated annealing or particle swarm approaches). Another way avenue to explore could be some form of regularisation which is common in imaging EIT (e.g., Tikhonov regularisation). However, regularisation requires some *a priori* knowledge about the solution, which could take the form of relationships between conductivity layers (e.g., brain-to-skull ratios). Much more research into the variability of tissue conductivity variation would be needed to assert such a condition. Additionally, Chapter 5 showed that new pEIT protocols could navigate the space more efficiently. This thesis only touched on the possibilities available here. With the ability to linearly combine injection pairs to make any pEIT pattern, new protocols could be tested easily and assessed on their sensitivity to different tissues. Work has already been done on the effect of multiple sink electrode montages for pEIT [64], and this work could now be accelerated with the use of ROM-pEIT.

A particular challenge of this work was the *ad hoc* management of memory and computing power. Often, the parallelisation was tailored to the available cluster computer. While this was trivial and could be adapted by any researcher, this is certainly an area that could benefit from being optimised and possibly automated for the use of future researchers and clinicians. A possible solution could come from the use of an message passing interface (MPI) implementation in the code. Given that MPI libraries are ubiquitous on high performance computing (HPC) systems and cluster computers, this would not introduce any portability problems to the code. This could be implemented in MATLAB (the language and environment used for this work and similar work like Zeffiro [90]) or re-written in C/C++ (the language used for the related software DUNEuro [158]). One further route of exploration could be the implementation of this work on graphic processing units (GPUs) which could also provide a health speed up.

Finally, a rigorous treatment of an error bound for the ROM-EEG-FP could be developed in future. Fig. 6.2 hinted that the bound for the dual problem (ROM-pEIT-FP) seemed to also bound the error in the ROM-EEG-FP tightly. While not rigorously derived, it does indicate that this area could be worth exploring with the aim of building the reduced models more efficiently. Bounding primal and dual problems has been explored in the literature, providing a starting point for such an analysis to be explored in future [40].

7.5 Final Conclusion and Outlook

In conclusion, the techniques of EEG and pEIT can be substantially enhanced by the use of ROM, unlocking new capabilities and thereby the potential for new levels of accuracy. The computational barrier to both methods has been lowered significantly through refactoring the costly computations into offline and online stages. This splitting has enabled additional tissue conductivities to be included in the IPs of both methods. As a result, both techniques have the potential to take up revolutionary new roles in the characterisation of brain activity.

The field of high accuracy EEG faces many challenges, one of which is the characterisation of appropriate head models. This work could mark a substantial step forward in the tools required to meet this challenge, and pave the way for more rigorous scientific analysis of common modelling assumptions. Further, with improved conductivity field characterisation, the improvement in source localisation naturally follows, as we have shown. Given the importance of source localisation in understanding brain function and the treatment and diagnosis of disease, this work could have far reaching consequences.

References

[1] Abascal, J.-F. P., Arridge, S. R., Atkinson, D., Horesh, R., Fabrizi, L., De Lucia, M., Horesh, L., Bayford, R. H., and Holder, D. S. (2008). Use of anisotropic modelling in electrical impedance tomography; Description of method and preliminary assessment of utility in imaging brain function in the adult human head. *NeuroImage*, 43(2):258–268.

[2] Adler, A., Gaggero, P. O., and Maimaitijiang, Y. (2011). Adjacent stimulation and measurement patterns considered harmful. *Physiological Measurement*, 32(7):731–744.

[3] Adler, A. and Lionheart, W. R. B. (2006). Uses and abuses of EIDORS: an extensible software base for EIT. *Physiological Measurement*, 27(5):S25–S42.

[4] Ahlfors, S. P., Han, J., Belliveau, J. W., and Hämäläinen, M. S. (2010). Sensitivity of MEG and EEG to Source Orientation. *Brain Topography*, 23(3):227–232.

[5] Akalin Acar, Z., Acar, C. E., and Makeig, S. (2016). Simultaneous head tissue conductivity and EEG source location estimation. *NeuroImage*, 124:168–180.

[6] Akalin Acar, Z. and Makeig, S. (2013). Effects of Forward Model Errors on EEG Source Localization. *Brain Topography*, 26(3):378–396.

[7] Akhtari, M., Bryant, H., Mamelak, A., Flynn, E., Heller, L., Shih, J., Mandelkem, M., Matlachov, A., Ranken, D., Best, E., DiMauro, M., Lee, R., and Sutherling, W. (2002). Conductivities of Three-Layer Live Human Skull. *Brain Topography*, 14(3):151–167.

[8] Akhtari, M., Bryant, H., Mamelak, A., Heller, L., Shih, J., Mandelkern, M., Matlachov, A., Ranken, D., Best, E., and Sutherling, W. (2000). Conductivities of Three-Layer Human Skull. *Brain Topography*, 13(1):29–42.

[9] Allison, T., Wood, C. C., McCarthy, G., and Spencer, D. D. (1991). Cortical somatosensory evoked potentials. II. Effects of excision of somatosensory or motor cortex in humans and monkeys. *Journal of Neurophysiology*, 66(1):64–82.

[10] Antonakakis, M., Schrader, S., Aydin, Ü., Khan, A., Gross, J., Zervakis, M., Rampp, S., and Wolters, C. H. (2020). Inter-Subject Variability of Skull Conductivity and Thickness in Calibrated Realistic Head Models. *NeuroImage*, 223:117353.

[11] Antonakakis, M., Schrader, S., Wollbrink, A., Oostenveld, R., Rampp, S., Haueisen, J., and Wolters, C. H. (2019). The effect of stimulation type, head modeling, and combined EEG and MEG on the source reconstruction of the somatosensory P20/N20 component. *Human Brain Mapping*, 40(17):5011–5028.

[12] Aristovich, K. Y., Packham, B. C., Koo, H., Santos, G. S. D., McEvoy, A., and Holder, D. S. (2016). Imaging fast electrical activity in the brain with electrical impedance tomography. *NeuroImage*, 124:204–213.

[13] Aubert-Broche, B., Evans, A. C., and Collins, L. (2006). A new improved version of the realistic digital brain phantom. *NeuroImage*, 32(1):138–145.

[14] Awada, K., Jackson, D., Williams, J., Wilton, D., Baumann, S., and Papanicolaou, A. (1997). Computational aspects of finite element modeling in EEG source localization. *IEEE Transactions on Biomedical Engineering*, 44(8):736–752.

[15] Aydin, Ü., Vorwerk, J., Dümpelmann, M., Küpper, P., Kugel, H., Heers, M., Wellmer, J., Kellinghaus, C., Haueisen, J., Rampp, S., Stefan, H., and Wolters, C. H. (2015). Combined EEG/MEG Can Outperform Single Modality EEG or MEG Source Reconstruction in Presurgical Epilepsy Diagnosis. *PLOS ONE*, 10(3):e0118753.

[16] Aydin, Ü., Vorwerk, J., Küpper, P., Heers, M., Kugel, H., Galka, A., Hamid, L., Wellmer, J., Kellinghaus, C., Rampp, S., and Wolters, C. H. (2014). Combining EEG and MEG for the Reconstruction of Epileptic Activity Using a Calibrated Realistic Volume Conductor Model. *PLoS ONE*, 9(3):e93154.

[17] Azevedo, F. A. C., Carvalho, L. R. B., Grinberg, L. T., Farfel, J. M., Ferretti, R. E. L., Leite, R. E. P., Filho, W. J., Lent, R., and Herculano-Houzel, S. (2009). Equal numbers of neuronal and nonneuronal cells make the human brain an isometrically scaled-up primate brain. *Journal of Comparative Neurology*, 513(5):532–541. Publisher: John Wiley & Sons, Ltd.

[18] Azizollahi, H., Aarabi, A., and Wallois, F. (2016). Effects of uncertainty in head tissue conductivity and complexity on EEG forward modeling in neonates. *Human Brain Mapping*, 37(10):3604–3622.

[19] Azizollahi, H., Aarabi, A., and Wallois, F. (2020). Effect of structural complexities in head modeling on the accuracy of EEG source localization in neonates. *Journal of Neural Engineering*, 17(5):056004.

[20] Bauer, M., Pursiainen, S., Vorwerk, J., Kostler, H., and Wolters, C. H. (2015). Comparison Study for Whitney (Raviart–Thomas)-Type Source Models in Finite-Element-Method-Based EEG Forward Modeling. *IEEE Transactions on Biomedical Engineering*, 62(11):2648–2656.

[21] Baumann, S., Wozny, D., Kelly, S., and Meno, F. (1997). The electrical conductivity of human cerebrospinal fluid at body temperature. *IEEE Transactions on Biomedical Engineering*, 44(3):220–223.

[22] Baumgärtner, U., Vogel, H., Ohara, S., Treede, R.-D., and Lenz, F. A. (2010). Dipole Source Analyses of Early Median Nerve SEP Components Obtained From Subdural Grid Recordings. *Journal of Neurophysiology*, 104(6):3029–3041.

[23] Baysal, U. U. and Haueisen, J. (2004). Use of *a priori* information in estimating tissue resistivities—application to human data *in vivo*. *Physiological Measurement*, 25(3):737–748.

[24] Beltrachini, L. (2019a). The analytical subtraction approach for solving the forward problem in EEG. *Journal of Neural Engineering*, 16(5):056029.

[25] Beltrachini, L. (2019b). A Finite Element Solution of the Forward Problem in EEG for Multipolar Sources. *IEEE Transactions on Neural Systems and Rehabilitation Engineering*, 27(3):368–377.

[26] Beltrachini, L. (2019c). Sensitivity of the Projected Subtraction Approach to Mesh Degeneracies and Its Impact on the Forward Problem in EEG. *IEEE Transactions on Biomedical Engineering*, 66(1):273–282.

[27] Beltrachini, L. (2024). The subtraction reciprocity theorem for volume conductors. *To be submitted*.

[28] Beltrachini, L., Taylor, Z. A., and Frangi, A. F. (2015). A parametric finite element solution of the generalised Bloch–Torrey equation for arbitrary domains. *Journal of Magnetic Resonance*, 259:126–134.

[29] Beltrachini, L., Von Ellenrieder, N., Eichardt, R., and Haueisen, J. (2021). Optimal design of on-scalp electromagnetic sensor arrays for brain source localisation. *Human Brain Mapping*, 42(15):4869–4879.

[30] Beltrachini, L., Von Ellenrieder, N., and Muravchik, C. H. (2013). Shrinkage Approach for Spatiotemporal EEG Covariance Matrix Estimation. *IEEE Transactions on Signal Processing*, 61(7):1797–1808.

[31] Bentley, D. E., Youell, P. D., Crossman, A. R., and Jones, A. K. (2001). Source localisation of 62-electrode human laser pain evoked potential data using a realistic head model. *International Journal of Psychophysiology*, 41(2):187–193.

[32] Björck, Å. (1994). Numerics of Gram-Schmidt orthogonalization. *Linear Algebra and its Applications*, 197-198:297–316.

[33] Booth, J. D., Chatterjee, A., Raghavan, P., and Frasca, M. (2011). A Multilevel Cholesky Conjugate Gradients Hybrid Solver for Linear Systems with Multiple Right-hand Sides. *Procedia Computer Science*, 4:2307–2316.

[34] Borsic, A., Graham, B., Adler, A., and Lionheart, W. (2010). *In Vivo* Impedance Imaging With Total Variation Regularization. *IEEE Transactions on Medical Imaging*, 29(1):44–54.

[35] Boverman, G., Isaacson, D., Newell, J. C., Saulnier, G. J., Kao, T.-J., Amm, B. C., Wang, X., Davenport, D. M., Chong, D. H., Sahni, R., and Ashe, J. M. (2017). Efficient Simultaneous Reconstruction of Time-Varying Images and Electrode Contact Impedances in Electrical Impedance Tomography. *IEEE Transactions on Biomedical Engineering*, 64(4):795–806.

[36] Buchner, H., Fuchs, M., Wischmann, H. A., Dössel, O., Ludwig, I., Knepper, A., and Berg, P. (1994). Source analysis of median nerve and finger stimulated somatosensory evoked potentials: Multichannel simultaneous recording of electric and magnetic fields combined with 3d-MR tomography. *Brain Topography*, 6(4):299–310.

[37] Bullmore, E. and Sporns, O. (2009). Complex brain networks: graph theoretical analysis of structural and functional systems. *Nature Reviews Neuroscience*, 10(3):186–198.

[38] Carson, E., Lund, K., Rozložník, M., and Thomas, S. (2022). Block Gram-Schmidt algorithms and their stability properties. *Linear Algebra and its Applications*, 638:150–195.

[39] Chella, F., Pizzella, V., Zappasodi, F., and Marzetti, L. (2016). Impact of the reference choice on scalp EEG connectivity estimation. *Journal of Neural Engineering*, 13(3):036016.

[40] Chen, P., Quarteroni, A., and Rozza, G. (2017). Reduced Basis Methods for Uncertainty Quantification. *SIAM/ASA Journal on Uncertainty Quantification*, 5(1):813–869.

[41] Chi Tang, Fusheng You, Guang Cheng, Dakuan Gao, Feng Fu, Guosheng Yang, and Xiuzhen Dong (2008). Correlation Between Structure and Resistivity Variations of the Live Human Skull. *IEEE Transactions on Biomedical Engineering*, 55(9):2286–2292.

[42] Cho, J.-H., Vorwerk, J., Wolters, C. H., and Knösche, T. R. (2015). Influence of the head model on EEG and MEG source connectivity analyses. *NeuroImage*, 110:60–77.

[43] Clerc, M., Badier, J.-M., Adde, G., Kybic, J., and Papadopoulo, T. (2005). Boundary Element formulation for Electrical Impedance Tomography. *ESAIM: Proceedings*, 14:63–71.

[44] Codecasa, L., Di Rienzo, L., Weise, K., Gross, S., and Haueisen, J. (2016). Fast MOR-Based Approach to Uncertainty Quantification in Transcranial Magnetic Stimulation. *IEEE Transactions on Magnetics*, 52(3):1–4.

[45] Corona, L., Tamilia, E., Perry, M. S., Madsen, J. R., Bolton, J., Stone, S. S. D., Stufflebeam, S. M., Pearl, P. L., and Papadelis, C. (2023). Non-invasive mapping of epileptogenic networks predicts surgical outcome. *Brain*, 146(5):1916–1931.

[46] Costa, F., Batatia, H., Oberlin, T., and Tourneret, J.-Y. (2017). Skull Conductivity Estimation for EEG Source Localization. *IEEE Signal Processing Letters*, 24(4):422–426.

[47] Dabek, J., Kalogianni, K., Rotgans, E., Van Der Helm, F. C., Kwakkel, G., Van Wegen, E. E., Daffertshofer, A., and De Munck, J. C. (2016). Determination of head conductivity frequency response in vivo with optimized EIT-EEG. *NeuroImage*, 127:484–495.

[48] Dalal, S. S., Rampp, S., Willomitzer, F., and Ettl, S. (2014). Consequences of EEG electrode position error on ultimate beamformer source reconstruction performance. *Frontiers in Neuroscience*, 8.

[49] Dannhauer, M., Lanfer, B., Wolters, C. H., and Knösche, T. R. (2011). Modeling of the human skull in EEG source analysis. *Human Brain Mapping*, 32(9):1383–1399.

[50] De Munck, J. and Peters, M. (1993). A fast method to compute the potential in the multisphere model (EEG application). *IEEE Transactions on Biomedical Engineering*, 40(11):1166–1174.

[51] De Munck, J., Van Dijk, B., and Spekreijse, H. (1988). Mathematical dipoles are adequate to describe realistic generators of human brain activity. *IEEE Transactions on Biomedical Engineering*, 35(11):960–966.

[52] De Munck, J. C. (1988). The potential distribution in a layered anisotropic spheroidal volume conductor. *Journal of Applied Physics*, 64(2):464–470.

[53] de Munck, J. C., Daffertshofer, A., Montes-Restrepo, V., Faes, T. J., Clerc, M., and Hulshof, J. (2019). Optimized application of double and single layer BEM for in vivo conductivity estimation. arXiv:1903.09971 [physics].

[54] Degabriele, R. and Lagopoulos, J. (2009). A review of EEG and ERP studies in bipolar disorder. *Acta Neuropsychiatrica*, 21(2):58–66.

[55] Dennis, J. E. and Schnabel, R. B. (1996). *Numerical Methods for Unconstrained Optimization and Nonlinear Equations*. Society for Industrial and Applied Mathematics.

[56] Dezhong Yao (2000). Electric potential produced by a dipole in a homogeneous conducting sphere. *IEEE Transactions on Biomedical Engineering*, 47(7):964–966.

[57] Drechsler, F., Wolters, C., Dierkes, T., Si, H., and Grasedyck, L. (2009). A full subtraction approach for finite element method based source analysis using constrained Delaunay tetrahedralisation. *NeuroImage*, 46(4):1055–1065.

[58] Ellis, H. and Mahadevan, V. (2014). The surgical anatomy of the scalp. *Surgery (Oxford)*, 32:e1–e5.

[59] Elman, H., Silvester, D., and Wathen, A. (2014). *Finite Elements and Fast Iterative Solvers: with Applications in Incompressible Fluid Dynamics*. Oxford University PressOxford, 2 edition.

[60] Fernández-Corazza, M., Beltrachini, L., Von Ellenrieder, N., and Muravchik, C. H. (2013). Analysis of parametric estimation of head tissue conductivities using Electrical Impedance Tomography. *Biomedical Signal Processing and Control*, 8(6):830–837.

[61] Fernández-Corazza, M., Turovets, S., Govyadinov, P., Muravchik, C. H., and Tucker, D. (2016a). Effects of Head Model Inaccuracies on Regional Scalp and Skull Conductivity Estimation Using Real EIT Measurements. In Simini, F. and Bertemes-Filho, P., editors, *II Latin American Conference on Bioimpedance*, volume 54, pages 5–8. Series Title: IFMBE Proceedings.

[62] Fernández-Corazza, M., Turovets, S., Luu, P., Anderson, E., and Tucker, D. (2016b). Transcranial Electrical Neuromodulation Based on the Reciprocity Principle. *Frontiers in Psychiatry*, 7.

[63] Fernández-Corazza, M., Turovets, S., Luu, P., Price, N., and Horacio Muravchik, C. (2018). Skull Modeling Effects in Conductivity Estimates Using Parametric Electrical Impedance Tomography. *IEEE Transactions on Biomedical Engineering*, 65(8):1785–1797.

[64] Fernández-Corazza, M., Turovets, S., and Muravchik, C. H. (2020a). A novel bounded EIT protocol to generate inhomogeneous skull conductivity maps non-invasively. In *2020 42nd Annual International Conference of the IEEE Engineering in Medicine & Biology Society (EMBC)*, pages 1440–1443, Montreal, QC, Canada. IEEE.

[65] Fernández-Corazza, M., Turovets, S., and Muravchik, C. H. (2020b). Unification of optimal targeting methods in transcranial electrical stimulation. *NeuroImage*, 209:116403.

[66] Fernández-Corazza, M., von Ellenrieder, N., and Muravchik, C. H. (2011). Estimation of electrical conductivity of a layered spherical head model using electrical impedance tomography. *Journal of Physics: Conference Series*, 332:012022.

[67] Ferree, T., Eriksen, K., and Tucker, D. (2000). Regional head tissue conductivity estimation for improved EEG analysis. *IEEE Transactions on Biomedical Engineering*, 47(12):1584–1592.

[68] Fiederer, L., Vorwerk, J., Lucka, F., Dannhauer, M., Yang, S., Dümpelmann, M., Schulze-Bonhage, A., Aertsen, A., Speck, O., Wolters, C., and Ball, T. (2016). The role of blood vessels in high-resolution volume conductor head modeling of EEG. *NeuroImage*, 128:193–208.

[69] Fraschini, M., Demuru, M., Crobe, A., Marrosu, F., Stam, C. J., and Hillebrand, A. (2016). The effect of epoch length on estimated EEG functional connectivity and brain network organisation. *Journal of Neural Engineering*, 13(3):036015.

[70] Fuchs, M., Wagner, M., Wischmann, H.-A., Köhler, T., Theißen, A., Drenckhahn, R., and Buchner, H. (1998). Improving source reconstructions by combining bioelectric and biomagnetic data. *Electroencephalography and Clinical Neurophysiology*, 107(2):93–111.

[71] Fulham, W. R., Michie, P. T., Ward, P. B., Rasser, P. E., Todd, J., Johnston, P. J., Thompson, P. M., and Schall, U. (2014). Mismatch Negativity in Recent-Onset and Chronic Schizophrenia: A Current Source Density Analysis. *PLoS ONE*, 9(6):e100221.

[72] Garcia-Larrea, L., Frot, M., and Valeriani, M. (2003). Brain generators of laser-evoked potentials: from dipoles to functional significance. *Neurophysiologie Clinique/Clinical Neurophysiology*, 33(6):279–292.

[73] Genna, C., Artoni, F., Fanciullacci, C., Chisari, C., Oddo, C. M., and Micera, S. (2016). Long-latency components of somatosensory evoked potentials during passive tactile perception of gratings. In *2016 38th Annual International Conference of the IEEE Engineering in Medicine and Biology Society (EMBC)*, pages 1648–1651, Orlando, FL, USA. IEEE.

[74] Geyer, S., Weiss, M., Reimann, K., Lohmann, G., and Turner, R. (2011). Microstructural Parcellation of the Human Cerebral Cortex – From Brodmann's Post-Mortem Map to in vivo Mapping with High-Field Magnetic Resonance Imaging. *Frontiers in Human Neuroscience*, 5.

[75] Giles, M. B. and Süli, E. (2002). Adjoint methods for PDEs: *a posteriori* error analysis and postprocessing by duality. *Acta Numerica*, 11:145–236.

[76] Godey, B., Schwartz, D., De Graaf, J., Chauvel, P., and Liégeois-Chauvel, C. (2001). Neuromagnetic source localization of auditory evoked fields and intracerebral evoked potentials: a comparison of data in the same patients. *Clinical Neurophysiology*, 112(10):1850–1859.

[77] Golub, G. H. and Van Loan, C. F. (2013). *Matrix computations*. Johns Hopkins studies in the mathematical sciences. The Johns Hopkins University Press, Baltimore, fourth edition edition.

[78] Gomez, C. K., Schiffman, S. R., and Bhatt, A. A. (2018). Radiological review of skull lesions. *Insights into Imaging*, 9(5):857–882.

[79] Goncalves, S., De Munck, J., Verbunt, J., Heethaar, R., and Da Silva, F. (2003). In vivo measurement of the brain and skull resistivities using an EIT-based method and the combined analysis of SEF/SEP data. *IEEE Transactions on Biomedical Engineering*, 50(9):1124–1127.

[80] Gutierrez, D., Nehorai, A., and Muravchik, C. (2004). Estimating Brain Conductivities and Dipole Source Signals With EEG Arrays. *IEEE Transactions on Biomedical Engineering*, 51(12):2113–2122.

[81] Güllmar, D., Haueisen, J., and Reichenbach, J. R. (2010). Influence of anisotropic electrical conductivity in white matter tissue on the EEG/MEG forward and inverse solution. A high-resolution whole head simulation study. *NeuroImage*, 51(1):145–163.

[82] Hader, W. J., Tellez-Zenteno, J., Metcalfe, A., Hernandez-Ronquillo, L., Wiebe, S., Kwon, C., and Jette, N. (2013). Complications of epilepsy surgery—A systematic review of focal surgical resections and invasive EEG monitoring. *Epilepsia*, 54(5):840–847.

[83] Hallez, H., Vanrumste, B., Hese, P. V., Delputte, S., and Lemahieu, I. (2008). Dipole estimation errors due to differences in modeling anisotropic conductivities in realistic head models for EEG source analysis. *Physics in Medicine and Biology*, 53(7):1877–1894.

[84] Hanke, M., Harrach, B., and Hyvönen, N. (2011). JUSTIFICATION OF POINT ELECTRODE MODELS IN ELECTRICAL IMPEDANCE TOMOGRAPHY. *Mathematical Models and Methods in Applied Sciences*, 21(06):1395–1413.

[85] Hari, R., Karhu, J., Hämäläinen, M., Knuutila, J., Salonen, O., Sams, M., and Vilkman, V. (1993). Functional Organization of the Human First and Second Somatosensory Cortices: a Neuromagnetic Study. *European Journal of Neuroscience*, 5(6):724–734.

[86] Hari, R. and Puce, A. (2017). *MEG-EEG Primer*. Oxford University Press, 1 edition.

[87] Hassan, M., Dufor, O., Merlet, I., Berrou, C., and Wendling, F. (2014). EEG Source Connectivity Analysis: From Dense Array Recordings to Brain Networks. *PLoS ONE*, 9(8):e105041.

[88] Haueisen, J., Tuch, D., Ramon, C., Schimpf, P., Wedeen, V., George, J., and Belliveau, J. (2002). The Influence of Brain Tissue Anisotropy on Human EEG and MEG. *NeuroImage*, 15(1):159–166.

[89] Hauthal, N., Thorne, J. D., Debener, S., and Sandmann, P. (2014). Source Localisation of Visual Evoked Potentials in Congenitally Deaf Individuals. *Brain Topography*, 27(3):412–424.

[90] He, Q., Rezaei, A., and Pursiainen, S. (2020). Zeffiro User Interface for Electromagnetic Brain Imaging: a GPU Accelerated FEM Tool for Forward and Inverse Computations in Matlab. *Neuroinformatics*, 18(2):237–250.

[91] Helms, G. (2016). Segmentation of human brain using structural MRI. *Magnetic Resonance Materials in Physics, Biology and Medicine*, 29(2):111–124.

[92] Holder, D., editor (2004). *Electrical Impedance Tomography*. CRC Press, 0 edition.

[93] Huang, M.-X., Song, T., Hagler, D. J., Podgorny, I., Jousmaki, V., Cui, L., Gaa, K., Harrington, D. L., Dale, A. M., Lee, R. R., Elman, J., and Halgren, E. (2007). A novel integrated MEG and EEG analysis method for dipolar sources. *NeuroImage*, 37(3):731–748.

[94] Hämäläinen, M., Hari, R., Ilmoniemi, R. J., Knuutila, J., and Lounasmaa, O. V. (1993). Magnetoencephalography—theory, instrumentation, and applications to noninvasive studies of the working human brain. *Reviews of Modern Physics*, 65(2):413–497.

[95] Jayakar, P., Gotman, J., Harvey, A. S., Palmini, A., Tassi, L., Schomer, D., Dubeau, F., Bartolomei, F., Yu, A., Kršek, P., Velis, D., and Kahane, P. (2016). Diagnostic utility of invasive EEG for epilepsy surgery: Indications, modalities, and techniques. *Epilepsia*, 57(11):1735–1747.

[96] Jog, M. A., Anderson, C., Kubicki, A., Boucher, M., Leaver, A., Hellemann, G., Iacoboni, M., Woods, R., and Narr, K. (2023). Transcranial direct current stimulation (tDCS) in depression induces structural plasticity. *Scientific Reports*, 13(1):2841.

[97] Johnson, C. (2009). *Numerical solution of partial differential equations by the finite element method*. Dover.

[98] Jones, D. K., editor (2011). *Diffusion MRI: theory, methods, and applications*. Oxford Univ. Press, New York Oxford.

[99] Kaipio, J. P., Kolehmainen, V., Somersalo, E., and Vauhkonen, M. (2000). Statistical inversion and Monte Carlo sampling methods in electrical impedance tomography. *Inverse Problems*, 16(5):1487–1522.

[100] Knappe, S., Sander, T., and Trahms, L. (2014). Optically-Pumped Magnetometers for MEG. In Supek, S. and Aine, C. J., editors, *Magnetoencephalography*, pages 993–999. Springer Berlin Heidelberg, Berlin, Heidelberg.

[101] Koulouri, A. and Rimpiläinen, V. (2021). Simultaneous Skull Conductivity and Focal Source Imaging from EEG Recordings with the Help of Bayesian Uncertainty Modelling. In Jarm, T., Cvetkoska, A., Mahnič-Kalamiza, S., and Miklavcic, D., editors, *8th European Medical and Biological Engineering Conference*, volume 80, pages 1019–1027. Springer International Publishing, Cham. Series Title: IFMBE Proceedings.

[102] Kuo-Sheng Cheng, Isaacson, D., Newell, J., and Gisser, D. (1989). Electrode models for electric current computed tomography. *IEEE Transactions on Biomedical Engineering*, 36(9):918–924.

[103] Lai, Y., Van Drongelen, W., Ding, L., Hecox, K., Towle, V., Frim, D., and He, B. (2005). Estimation of in vivo human brain-to-skull conductivity ratio from simultaneous extra- and intra-cranial electrical potential recordings. *Clinical Neurophysiology*, 116(2):456–465.

[104] Lanfer, B., Scherg, M., Dannhauer, M., Knösche, T., Burger, M., and Wolters, C. (2012). Influences of skull segmentation inaccuracies on EEG source analysis. *NeuroImage*, 62(1):418–431.

[105] Lenartowicz, A. and Loo, S. K. (2014). Use of EEG to Diagnose ADHD. *Current Psychiatry Reports*, 16(11):498.

[106] Lew, S., Sliva, D. D., Choe, M.-s., Grant, P. E., Okada, Y., Wolters, C. H., and Hämäläinen, M. S. (2013). Effects of sutures and fontanels on MEG and EEG source analysis in a realistic infant head model. *NeuroImage*, 76:282–293.

[107] Lew, S., Wolters, C., Dierkes, T., Röer, C., and MacLeod, R. (2009a). Accuracy and run-time comparison for different potential approaches and iterative solvers in finite element method based EEG source analysis. *Applied Numerical Mathematics*, 59(8):1970–1988.

[108] Lew, S., Wolters, C. H., Anwander, A., Makeig, S., and MacLeod, R. S. (2009b). Improved EEG source analysis using low-resolution conductivity estimation in a four-compartment finite element head model. *Human Brain Mapping*, 30(9):2862–2878.

[109] Liu, Q., Balsters, J. H., Baechinger, M., Van Der Groen, O., Wenderoth, N., and Mantini, D. (2015). Estimating a neutral reference for electroencephalographic recordings: the importance of using a high-density montage and a realistic head model. *Journal of Neural Engineering*, 12(5):056012.

[110] Lou, Y., Shi, Y., Yang, K., Zhou, L., Yang, T., Zhang, P., Qin, B., and Qian, Z. (2024). Modified tuna swarm optimization algorithm for brain stroke imaging with electrical impedance tomography. *Engineering Analysis with Boundary Elements*, 165:105786.

[111] Maksymenko, K., Clerc, M., and Papadopoulo, T. (2020). Fast Approximation of EEG Forward Problem and Application to Tissue Conductivity Estimation. *IEEE Transactions on Medical Imaging*, 39(4):888–897.

[112] Manzoni, A. and Negri, F. (2015). Heuristic strategies for the approximation of stability factors in quadratically nonlinear parametrized PDEs. *Advances in Computational Mathematics*, 41(5):1255–1288.

[113] Martin, J. B. (2002). The Integration of Neurology, Psychiatry, and Neuroscience in the 21st Century. *American Journal of Psychiatry*, 159(5):695–704.

[114] McCann, H. and Beltrachini, L. (2021). Does participant's age impact on tDCS induced fields? Insights from computational simulations. *Biomedical Physics & Engineering Express*, 7(4):045018.

[115] McCann, H. and Beltrachini, L. (2022). Impact of skull sutures, spongiform bone distribution, and aging skull conductivities on the EEG forward and inverse problems. *Journal of Neural Engineering*, 19(1):016014.

[116] McCann, H., Pisano, G., and Beltrachini, L. (2019). Variation in Reported Human Head Tissue Electrical Conductivity Values. *Brain Topography*, 32(5):825–858.

[117] Michel, C. M. and Brunet, D. (2019). EEG Source Imaging: A Practical Review of the Analysis Steps. *Frontiers in Neurology*, 10:325.

[118] Miinalainen, T., Rezaei, A., Us, D., Nüßing, A., Engwer, C., Wolters, C. H., and Pursiainen, S. (2019). A realistic, accurate and fast source modeling approach for the EEG forward problem. *NeuroImage*, 184:56–67.

[119] Montes-Restrepo, V., Carrette, E., Strobbe, G., Gadeyne, S., Vandenberghe, S., Boon, P., Vonck, K., and Mierlo, P. V. (2016). The Role of Skull Modeling in EEG Source Imaging for Patients with Refractory Temporal Lobe Epilepsy. *Brain Topography*, 29(4):572–589.

[120] Montes-Restrepo, V., Van Mierlo, P., Strobbe, G., Staelens, S., Vandenberghe, S., and Hallez, H. (2014). Influence of Skull Modeling Approaches on EEG Source Localization. *Brain Topography*, 27(1):95–111.

[121] Moody, G. B. (2013). LightWAVE: Waveform and annotation viewing and editing in aWeb browser. In *Computing in Cardiology 2013*, pages 17–20.

[122] Neugebauer, F., Antonakakis, M., Unnwongse, K., Parpaley, Y., Wellmer, J., Rampp, S., and Wolters, C. H. (2022). Validating EEG, MEG and Combined MEG and EEG Beamforming for an Estimation of the Epileptogenic Zone in Focal Cortical Dysplasia. *Brain Sciences*, 12(1):114.

[123] Neugebauer, F., Möddel, G., Rampp, S., Burger, M., and Wolters, C. H. (2017). The Effect of Head Model Simplification on Beamformer Source Localization. *Frontiers in Neuroscience*, 11:625.

[124] O'Leary, D. P. (1980). The block conjugate gradient algorithm and related methods. *Linear Algebra and its Applications*, 29:293–322.

[125] Oostendorp, T., Delbeke, J., and Stegeman, D. (2000). The conductivity of the human skull: results of in vivo and in vitro measurements. *IEEE Transactions on Biomedical Engineering*, 47(11):1487–1492.

[126] Oostenveld, R. and Praamstra, P. (2001). The five percent electrode system for high-resolution EEG and ERP measurements. *Clinical Neurophysiology*, 112(4):713–719.

[127] Ouypornkochagorn, T. and Ouypornkochagorn, S. (2019). In Vivo Estimation of Head Tissue Conductivities Using Bound Constrained Optimization. *Annals of Biomedical Engineering*, 47(7):1575–1583.

[128] Pascual-Marqui, R., Michel, C., and Lehmann, D. (1994). Low resolution electromagnetic tomography: a new method for localizing electrical activity in the brain. *International Journal of Psychophysiology*, 18(1):49–65.

[129] Pascual-Marqui, R. D. (2002). Standardized low-resolution brain electromagnetic tomography (sLORETA): technical details. *Methods and Findings in Experimental and Clinical Pharmacology*, 24 Suppl D:5–12.

[130] Pascual-Marqui, R. D. (2007). Discrete, 3D distributed, linear imaging methods of electric neuronal activity. Part 1: exact, zero error localization. Version Number: 2.

[131] Pohlmeier, R., Buchner, H., Knoll, G., Rienäcker, A., Beckmann, R., and Pesch, J. (1997). The influence of skull-conductivity misspecification on inverse source localization in realistically shaped finite element head models. *Brain Topography*, 9(3):157–162.

[132] Poolman, P., Turovets, S. I., Frank, R. M., and Russell, G. S. (2008). Instrumentation and Signal Processing for Low-frequency Bounded-EIT Studies of the Human Head. In *2008 IEEE Instrumentation and Measurement Technology Conference*, pages 602–606, Victoria, BC, Canada. IEEE.

[133] Pursiainen, S. (2012). Raviart–Thomas-type sources adapted to applied EEG and MEG: implementation and results. *Inverse Problems*, 28(6):065013.

[134] Pursiainen, S., Agsten, B., Wagner, S., and Wolters, C. H. (2018). Advanced Boundary Electrode Modeling for tES and Parallel tES/EEG. *IEEE Transactions on Neural Systems and Rehabilitation Engineering*, 26(1):37–44.

[135] Pursiainen, S., Lucka, F., and Wolters, C. H. (2012). Complete electrode model in EEG: relationship and differences to the point electrode model. *Physics in Medicine and Biology*, 57(4):999–1017.

[136] Pursiainen, S., Sorrentino, A., Campi, C., and Piana, M. (2011). Forward simulation and inverse dipole localization with the lowest order Raviart—Thomas elements for electroencephalography. *Inverse Problems*, 27(4):045003.

[137] Pursiainen, S., Vorwerk, J., and Wolters, C. H. (2016). Electroencephalography (EEG) forward modeling via H (div) finite element sources with focal interpolation. *Physics in Medicine and Biology*, 61(24):8502–8520.

[138] Qianqian Fang and Boas, D. A. (2009). Tetrahedral mesh generation from volumetric binary and grayscale images. In *2009 IEEE International Symposium on Biomedical Imaging: From Nano to Macro*, pages 1142–1145, Boston, MA, USA. IEEE.

[139] Quarteroni, A., Manzoni, A., and Negri, F. (2016). *Reduced Basis Methods for Partial Differential Equations*, volume 92 of *UNITEXT*. Springer International Publishing, Cham.

[140] Quarteroni, A., Sacco, R., and Saleri, F. (2007). *Numerical Mathematics*, volume 37 of *Texts in Applied Mathematics*. Springer New York, New York, NY.

[141] Quillen, P. and Ye, Q. (2010). A block inverse-free preconditioned Krylov subspace method for symmetric generalized eigenvalue problems. *Journal of Computational and Applied Mathematics*, 233(5):1298–1313.

[142] Ramon, C., Garguilo, P., Fridgeirsson, E. A., and Haueisen, J. (2014). Changes in scalp potentials and spatial smoothing effects of inclusion of dura layer in human head models for EEG simulations. *Frontiers in Neuroengineering*, 7.

[143] Ramon, C., Schimpf, P., Haueisen, J., Holmes, M., and Ishimaru, A. (2003). Role of Soft Bone, CSF and Gray Matter in EEG Simulations. *Brain Topography*, 16(4):245–248.

[144] Ramon, C., Schimpf, P. H., and Haueisen, J. (2006). Influence of head models on EEG simulations and inverse source localizations. *BioMedical Engineering OnLine*, 5(1):10.

[145] Rimpiläinen, V., Koulouri, A., Lucka, F., Kaipio, J. P., and Wolters, C. H. (2019). Improved EEG source localization with Bayesian uncertainty modelling of unknown skull conductivity. *NeuroImage*, 188:252–260.

[146] Ropper, A. H., Adams, R. D., Victor, M., Brown, R. H., and Victor, M. (2005). *Adams and Victor's principles of neurology*. McGraw-Hill, New York, 8. ed edition.

[147] Rossi Sebastiano, D., Tassi, L., Duran, D., Visani, E., Gozzo, F., Cardinale, F., Nobili, L., Del Sole, A., Rubino, A., Dotta, S., Schiaffi, E., Garbelli, R., Franceschetti, S., Spreafico, R., and Panzica, F. (2020). Identifying the epileptogenic zone by four non-invasive imaging techniques versus stereo-EEG in MRI-negative pre-surgery epilepsy patients. *Clinical Neurophysiology*, 131(8):1815–1823.

[148] Sadleir, R. J., Vannorsdall, T. D., Schretlen, D. J., and Gordon, B. (2012). Target Optimization in Transcranial Direct Current Stimulation. *Frontiers in Psychiatry*, 3.

[149] Salman, A., Turovets, S., Malony, A., Eriksen, J., and Tucker, D. (2005). Computational Modeling of Human Head Conductivity. In Hutchison, D., Kanade, T., Kittler, J., Kleinberg, J. M., Mattern, F., Mitchell, J. C., Naor, M., Nierstrasz, O., Pandu Rangan, C., Steffen, B., Sudan, M., Terzopoulos, D., Tygar, D., Vardi, M. Y., Weikum, G., Sunderam, V. S., Van Albada, G. D., Sloot, P. M. A., and Dongarra, J. J., editors, *Computational Science – ICCS 2005*, volume 3514, pages 631–638. Springer Berlin Heidelberg, Berlin, Heidelberg. Series Title: Lecture Notes in Computer Science.

[150] Sanei, S. and Chambers, J. (2007). *EEG Signal Processing*. Wiley, 1 edition.

[151] Sarvas, J. (1987). Basic mathematical and electromagnetic concepts of the biomagnetic inverse problem. *Physics in Medicine and Biology*, 32(1):11–22.

[152] Saturnino, G. B., Puonti, O., Nielsen, J. D., Antonenko, D., Madsen, K. H., and Thielscher, A. (2019a). SimNIBS 2.1: A Comprehensive Pipeline for Individualized Electric Field Modelling for Transcranial Brain Stimulation. In Makarov, S., Horner, M., and Noetscher, G., editors, *Brain and Human Body Modeling*, pages 3–25. Springer International Publishing, Cham.

[153] Saturnino, G. B., Thielscher, A., Madsen, K. H., Knösche, T. R., and Weise, K. (2019b). A principled approach to conductivity uncertainty analysis in electric field calculations. *NeuroImage*, 188:821–834.

[154] Schimpf, P., Ramon, C., and Haueisen, J. (2002). Dipole models for the EEG and MEG. *IEEE Transactions on Biomedical Engineering*, 49(5):409–418.

[155] Schmidt, C., Wagner, S., Burger, M., Rienen, U. V., and Wolters, C. H. (2015). Impact of uncertain head tissue conductivity in the optimization of transcranial direct current stimulation for an auditory target. *Journal of Neural Engineering*, 12(4):046028.

[156] Schoffelen, J. and Gross, J. (2009). Source connectivity analysis with MEG and EEG. *Human Brain Mapping*, 30(6):1857–1865.

[157] Schrader, S., Antonakakis, M., Rampp, S., Engwer, C., and Wolters, C. H. (2020). A novel method for calibrating head models to account for variability in conductivity and its evaluation in a sphere model. *Physics in Medicine & Biology*, 65(24):245043.

[158] Schrader, S., Westhoff, A., Piastra, M. C., Miinalainen, T., Pursiainen, S., Vorwerk, J., Brinck, H., Wolters, C. H., and Engwer, C. (2021). DUNEuro—A software toolbox for forward modeling in bioelectromagnetism. *PLOS ONE*, 16(6):e0252431.

[159] Seo, J. K., Kim, K. C., Jargal, A., Lee, K., and Harrach, B. (2019). A Learning-Based Method for Solving Ill-Posed Nonlinear Inverse Problems: A Simulation Study of Lung EIT. *SIAM Journal on Imaging Sciences*, 12(3):1275–1295.

[160] Shoeb, A. (2010). CHB-MIT Scalp EEG Database.

[161] Silvester, P. P. and Ferrari, R. L. (1996). *Finite Elements for Electrical Engineers*. Cambridge University Press, 3 edition.

[162] Somersalo, E., Cheney, M., and Isaacson, D. (1992). Existence and Uniqueness for Electrode Models for Electric Current Computed Tomography. *SIAM Journal on Applied Mathematics*, 52(4):1023–1040.

[163] Stenroos, M. and Hauk, O. (2013). Minimum-norm cortical source estimation in layered head models is robust against skull conductivity error. *NeuroImage*, 81:265–272.

[164] Tae-Seong Kim, Yongxia Zhou, Sungheon Kim, and Singh, M. (2002). EEG distributed source imaging with a realistic finite-element head model. *IEEE Transactions on Nuclear Science*, 49(3):745–752.

[165] Thevenet, M., Bertrand, O., Perrin, F., Dumont, T., and Pernier, J. (1991). The finite element method for a realistic head model of electrical brain activities: preliminary results. *Clinical Physics and Physiological Measurement*, 12(A):89–94.

[166] Tran, A. P., Yan, S., and Fang, Q. (2020). Improving model-based functional near-infrared spectroscopy analysis using mesh-based anatomical and light-transport models. *Neurophotonics*, 7(01):1.

[167] Treede, R.-D., Lorenz, J., and Baumgärtner, U. (2003). Clinical usefulness of laser-evoked potentials. *Neurophysiologie Clinique/Clinical Neurophysiology*, 33(6):303–314.

[168] Trenado, C., Elben, S., Friggemann, L., Gruhn, S., Groiss, S. J., Vesper, J., Schnitzler, A., and Wojtecki, L. (2017). Long-Latency Somatosensory Evoked Potentials of the Subthalamic Nucleus in Patients with Parkinson's Disease. *PLOS ONE*, 12(1):e0168151.

[169] Turovets, S. I., Poolman, P., Salman, A., Malony, A. D., and Tucker, D. M. (2008). Conductivity Analysis for High-Resolution EEG. In *2008 International Conference on BioMedical Engineering and Informatics*, pages 386–393, Sanya, China. IEEE.

[170] Unnwongse, K., Rampp, S., Wehner, T., Kowoll, A., Parpaley, Y., Von Lehe, M., Lanfer, B., Rusiniak, M., Wolters, C., and Wellmer, J. (2022). Validating EEG source imaging using intracranial electrical stimulation. *Brain Communications*, 5(1):fcad023.

[171] Valeriani, M., Insola, A., Restuccia, D., Le Pera, D., Mazzone, P., Altibrandi, M. G., and Tonali, P. (2001). Source generators of the early somatosensory evoked potentials to tibial nerve stimulation: an intracerebral and scalp recording study. *Clinical Neurophysiology*, 112(11):1999–2006.

[172] Vallaghe, S. and Clerc, M. (2009). A Global Sensitivity Analysis of Three- and Four-Layer EEG Conductivity Models. *IEEE Transactions on Biomedical Engineering*, 56(4):988–995.

[173] Vallaghe, S., Clerc, M., and Badier, J.-m. (2007). IN VIVO CONDUCTIVITY ESTIMATION USING SOMATOSENSORY EVOKED POTENTIALS AND CORTICAL CONSTRAINT ON THE SOURCE. In *2007 4th IEEE International Symposium on Biomedical Imaging: From Nano to Macro*, pages 1036–1039, Arlington, VA, USA. IEEE.

[174] Van Mierlo, P., Vorderwülbecke, B. J., Staljanssens, W., Seeck, M., and Vulliémoz, S. (2020). Ictal EEG source localization in focal epilepsy: Review and future perspectives. *Clinical Neurophysiology*, 131(11):2600–2616.

[175] Vanrumste, B., Van Hoey, G., Van De Walle, R., D'Havé, M., Lemahieu, I., and Boon, P. (2000). Dipole location errors in electroencephalogram source analysis due to volume conductor model errors. *Medical and Biological Engineering and Computing*, 38(5):528–534.

[176] Vatta, F., Meneghini, F., Esposito, F., Mininel, S., and Di Salle, F. (2010). Realistic and Spherical Head Modeling for EEG Forward Problem Solution: A Comparative Cortex-Based Analysis. *Computational Intelligence and Neuroscience*, 2010:1–11.

[177] Vauhkonen, M., Kaipio, J. P., Somersalo, E., and Karjalainen, P. A. (1997). Electrical impedance tomography with basis constraints. *Inverse Problems*, 13(2):523–530.

[178] Vauhkonen, M., Vadasz, D., Karjalainen, P., Somersalo, E., and Kaipio, J. (1998). Tikhonov regularization and prior information in electrical impedance tomography. *IEEE Transactions on Medical Imaging*, 17(2):285–293.

[179] Vauhkonen, P., Vauhkonen, M., Savolainen, T., and Kaipio, J. (1999). Three-dimensional electrical impedance tomography based on the complete electrode model. *IEEE Transactions on Biomedical Engineering*, 46(9):1150–1160.

[180] Vauhkonen, P. J., Vauhkonen, M., and Kaipio, J. P. (2001). Fixed-lag smoothing and state estimation in dynamic electrical impedance tomography. *International Journal for Numerical Methods in Engineering*, 50(9):2195–2209.

[181] Vilhunen, T., Kaipio, J. P., Vauhkonen, P. J., Savolainen, T., and Vauhkonen, M. (2002). Simultaneous reconstruction of electrode contact impedances and internal electrical properties: I. Theory. *Measurement Science and Technology*, 13(12):1848–1854.

[182] von Bartheld, C. S., Bahney, J., and Herculano-Houzel, S. (2016). The search for true numbers of neurons and glial cells in the human brain: A review of 150 years of cell counting. *Journal of Comparative Neurology*, 524(18):3865–3895. _eprint: https://onlinelibrary.wiley.com/doi/pdf/10.1002/cne.24040.

[183] Von Ellenrieder, N., Muravchik, C., Wagner, M., and Nehorai, A. (2009). Effect of Head Shape Variations Among Individuals on the EEG/MEG Forward and Inverse Problems. *IEEE Transactions on Biomedical Engineering*, 56(3):587–597.

[184] Vorwerk, J., Aydin, Ü., Wolters, C. H., and Butson, C. R. (2019a). Influence of Head Tissue Conductivity Uncertainties on EEG Dipole Reconstruction. *Frontiers in Neuroscience*, 13:531.

[185] Vorwerk, J., Cho, J.-H., Rampp, S., Hamer, H., Knösche, T. R., and Wolters, C. H. (2014). A guideline for head volume conductor modeling in EEG and MEG. *NeuroImage*, 100:590–607.

[186] Vorwerk, J., Hanrath, A., Wolters, C. H., and Grasedyck, L. (2019b). The multipole approach for EEG forward modeling using the finite element method. *NeuroImage*, 201:116039.

[187] Vorwerk, J., Wolters, C. H., and Baumgarten, D. (2024). Global sensitivity of EEG source analysis to tissue conductivity uncertainties. *Frontiers in Human Neuroscience*, 18:1335212.

[188] Wagner, S., Rampersad, S. M., Aydin, Ü., Vorwerk, J., Oostendorp, T. F., Neuling, T., Herrmann, C. S., Stegeman, D. F., and Wolters, C. H. (2014). Investigation of tDCS volume conduction effects in a highly realistic head model. *Journal of Neural Engineering*, 11(1):016002.

[189] Walker, M. R., Fernández-Corazza, M., Turovets, S., and Beltrachini, L. (2024). Electrical Impedance Tomography meets Reduced Order Modelling: a framework for faster and more reliable electrical conductivity estimations. Version Number: 1.

[190] Wang, Y. and Gotman, J. (2001). The influence of electrode location errors on EEG dipole source localization with a realistic head model. *Clinical Neurophysiology*, 112(9):1777–1780.

[191] Weinstein, D., Zhukov, L., and Johnson, C. (2000). Lead-field Bases for Electroencephalography Source Imaging. *Annals of Biomedical Engineering*, 28(9):1059–1065.

[192] Whittingstall, K., Stroink, G., Gates, L., Connolly, J., and Finley, A. (2003). Effects of dipole position, orientation and noise on the accuracy of EEG source localization. *BioMedical Engineering OnLine*, 2(1):14.

[193] Wolters, C., Anwander, A., Tricoche, X., Weinstein, D., Koch, M., and MacLeod, R. (2006). Influence of tissue conductivity anisotropy on EEG/MEG field and return current computation in a realistic head model: A simulation and visualization study using high-resolution finite element modeling. *NeuroImage*, 30(3):813–826.

[194] Wolters, C., Köstler, H., Möller, C., Härdtlein, J., and Anwander, A. (2007). Numerical approaches for dipole modeling in finite element method based source analysis. *International Congress Series*, 1300:189–192.

[195] Wolters, C. H., Antonakakis, M., Khan, A., Piastra, M. C., and Vorwerk, J. (2021). Characterization of the Somatosensory System. In Groppa, S. and G. Meuth, S., editors, *Translational Methods for Multiple Sclerosis Research*, volume 166, pages 153–169. Springer US, New York, NY. Series Title: Neuromethods.

[196] Wolters, C. H., Grasedyck, L., and Hackbusch, W. (2004). Efficient computation of lead field bases and influence matrix for the FEM-based EEG and MEG inverse problem. *Inverse Problems*, 20(4):1099–1116.

[197] Wolters, C. H., Köstler, H., Möller, C., Härdtlein, J., Grasedyck, L., and Hackbusch, W. (2008). Numerical Mathematics of the Subtraction Method for the Modeling of a Current Dipole in EEG Source Reconstruction Using Finite Element Head Models. *SIAM Journal on Scientific Computing*, 30(1):24–45.

[198] Wolters, C. H., Lew, S., MacLeod, R. S., and Hämäläinen, M. (2010). Combined EEG/MEG source analysis using calibrated finite element head models. *Biomedizinische Technik/Biomedical Engineering. Rostock, Germany: Walter de Gruyter*, 55(Suppl 1):64–68. Publisher: Citeseer.

[199] Yang, L., Wilke, C., Brinkmann, B., Worrell, G. A., and He, B. (2011). Dynamic imaging of ictal oscillations using non-invasive high-resolution EEG. *NeuroImage*, 56(4):1908–1917.

[200] Yao, D. (2001). A method to standardize a reference of scalp EEG recordings to a point at infinity. *Physiological Measurement*, 22(4):693–711.

[201] Zhao, M., Marino, M., Samogin, J., Swinnen, S. P., and Mantini, D. (2019). Hand, foot and lip representations in primary sensorimotor cortex: a high-density electroencephalography study. *Scientific Reports*, 9(1):19464.

[202] Zijlmans, M., Zweiphenning, W., and Van Klink, N. (2019). Changing concepts in presurgical assessment for epilepsy surgery. *Nature Reviews Neurology*, 15(10):594–606.

Appendix A

Details on the Stiffness Matrix

A.1 Volume and Area Coordinates

Solving the integrals in eqs. (3.34) in Cartesian coordinates can become protracted and cumbersome. To alleviate this issue, barycentric coordinates can be employed to simplify these integrals. These coordinates are often referred to as simplex coordinates or volume or area coordinates in the special cases of 3 dimensional tetrahedrons and 2 dimensional triangles respectively.

Firstly, let an arbitrary tetrahedron T_k in the mesh have a volume V and nodes $\boldsymbol{p_i}$ where $i = 1,2,3,4$. Then, for any point $\boldsymbol{r} \in \mathrm{T}_k$ there exists 4 tetrahedrons made from the points $\boldsymbol{r}$ and $\boldsymbol{p_j}$, $j = 1,2,3,4$ $(j \neq i)$, with volumes V_i. The volume coordinates are then defined as

$$\xi_i = \frac{V_i}{V} = \frac{a_i + b_i x_1 + c_i x_2 + d_i x_3}{6V}, \quad i = 1,2,3,4, \tag{A.1}$$

or in matrix form,

$$\boldsymbol{\xi} = \frac{1}{6V}(\boldsymbol{a} + \boldsymbol{\Lambda}^T \boldsymbol{r}), \tag{A.2}$$

where $\boldsymbol{\xi} = [\xi_1, \xi_2, \xi_3, \xi_4]^T$, $\boldsymbol{r} = [x_1, x_2, x_3]^T$, $\boldsymbol{\Lambda} = [\boldsymbol{b}, \boldsymbol{c}, \boldsymbol{d}]^T$ and $\boldsymbol{a}$, $\boldsymbol{b}$, $\boldsymbol{c}$ and $\boldsymbol{d}$ are the 4×1 vectors with elements a_i, b_i, c_i and d_i respectively. Transforming the coordinate system to volume coordinates normalises the tetrahedrons, therefore the basis functions in the volume coordinate system simply reduce to $\boldsymbol{\psi}(\boldsymbol{\xi}) = \boldsymbol{\xi}$. This allows the integrals to take the form

$$\int_{\mathrm{T}_k} \xi_1^i \xi_2^j \xi_3^k \xi_4^j \, d\boldsymbol{\xi} = 6V \frac{i!j!k!j!}{(i+j+k+j+3)!}. \tag{A.3}$$

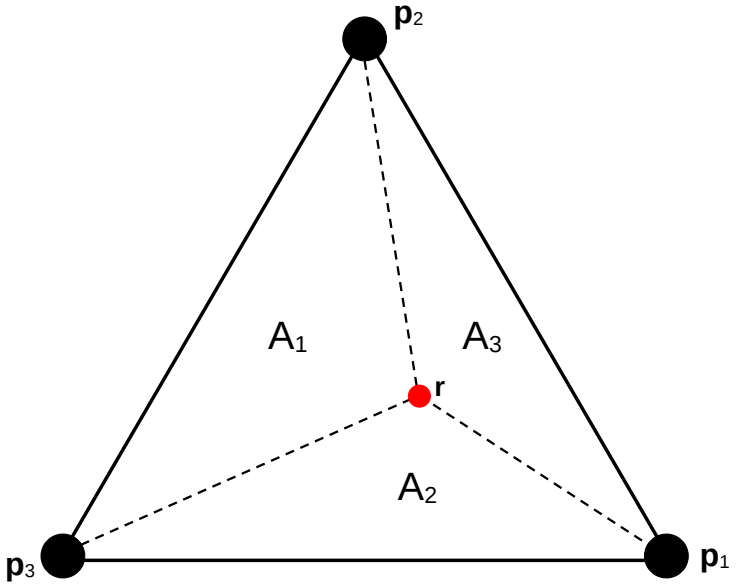

Fig. A.1 A triangle (simplex), part of a finite element mesh, with area A and vertices $\boldsymbol{p}_i$ $(i = 1,2,3)$ being transformed from Cartesian Coordinates to Area Coordinates. The red dot labelled $\boldsymbol{r}$ can be any point within the triangle and creates the 3 triangles with areas $\boldsymbol{A}_i$ where $i = 1,2,3$.

Similarly, for the 2 dimensional case, the area coordinates and the corresponding integrals take the form

$$\xi_i = \frac{A_i}{A} = \frac{a_i + b_i x_1 + c_i x_2}{2A}, \quad i = 1,2,3, \tag{A.4a}$$

$$\int_{\mathrm{T}_k} \xi_1^i \xi_2^j \xi_3^k \, d\boldsymbol{\xi} = 2A \frac{i!\,j!\,k!}{(i+j+k+2)!}, \tag{A.4b}$$

where T_k is an arbitrary triangle with area A split into 3 additional triangles with areas A_i, $i = 1,2,3$, by any point $\boldsymbol{r} \in \mathrm{T}_k$ and points $\boldsymbol{p}_j$, $j = 1,2,3$, $(j \neq i)$. An example of this is given in Fig. A.1. After significant algebraic manipulation, the element matrices used for constructing the global stiffness matrix, can be computed simply as

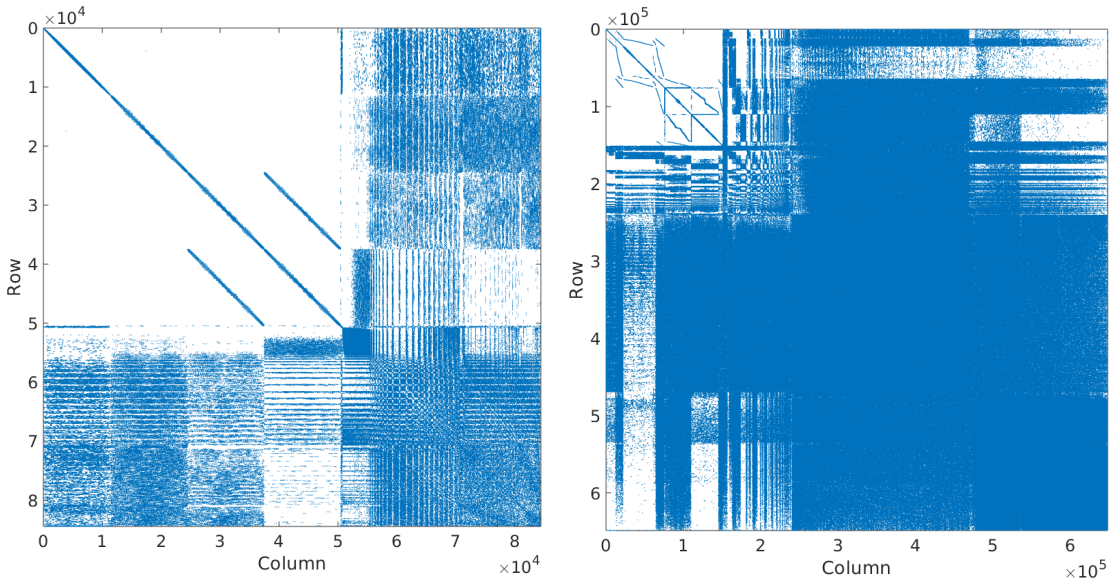

Fig. A.2 Non-zero inputs of the stiffness matrices plotted by position for **left)** spherical head model with 84K nodes and 120 electrodes and **right)** realistic head model with 650K nodes and 133 electrodes.

$$\boldsymbol{K}_k^{e1} = \frac{1}{36V_e}\boldsymbol{\Lambda}^T\boldsymbol{\sigma}\boldsymbol{\Lambda}, \tag{A.5a}$$

$$\boldsymbol{K}_k^{e2} = \sum_{l=1}^{L}\frac{1}{z_l}\frac{A_e}{12}(\mathbf{1}_{3,3}+\boldsymbol{I}_3), \tag{A.5b}$$

$$\boldsymbol{B}_k^{e} = \sum_{l=1}^{L}\frac{1}{z_l}\frac{A_e}{3}\mathbf{1}_{1,3}, \tag{A.5c}$$

where $\boldsymbol{I}_3$ is a 3×3 identity matrix, $\mathbf{1}_{3,3}$ is a 3×3 matrix of ones and $\mathbf{1}_{1,3}$ is a 1×3 vector of ones. $\boldsymbol{K}_k^{e1}$ and $\boldsymbol{K}_k^{e2}$ are constructed separately and summed to make $\boldsymbol{K}(\boldsymbol{\sigma})$ following eq. (3.34)a.

Employing volume and area coordinates have previously been used for the PEM in EEG [24] and for FE implementations of the Bloch-Torrey equations [28]. Alternatively, linear Lagrangian basis functions have also been utilised by Pursiainen et al. (2012) [135]. For more details on the derivation of the above element stiffness matrices the reader is directed to Beltrachini et al. (2015), Beltrachini (2019) and Silvester and Ferrari (1996) [28, 24, 161].

A.2 Sparse Stiffness Matrices

After solving the element stiffness matrices and summing the contributions for each node, the resulting stiffness matrix is highly sparse. This property makes it efficient to store when using sparse matrix tools (e.g., `sparse()` in MATLAB). Revisiting the spherical head model example with 120 electrodes and 84K nodes, the number of non-zero inputs is ~1.2M, only 0.0177% of the total number of matrix inputs. In a realistic head model, with 650K nodes and 133 electrodes, the stiffness matrix has ~10M non-zero inputs which occupies only 0.0024% of the matrix. Fig. A.2 is a visual representation of the sparseness of the stiffness matrices.